**Title**
Organic-Inorganic Thermoelectrics from Single Monomers to Polymer Devices



**Author**
Chang, William Bee

**Publication Date**
2015

Peer reviewed|Thesis/dissertation

# Organic-Inorganic Thermoelectrics from Single Monomers to Polymer Devices

By

William Bee Chang

A dissertation submitted in partial satisfaction of the

requirements for the degree of

Doctor of Philosophy

in

Engineering - Materials Science and Engineering

in the

Graduate Division

of the

University of California, Berkeley

Committee in Charge:

Professor Rachel Segalman, Co-chair

Professor Junqiao Wu, Co-chair

Professor Mark Asta

Professor Jeffrey B. Neaton

Fall 2015

Abstract

Organic-Inorganic Thermoelectrics from Single Monomers to Polymer Devices

By

William Bee Chang

Doctor of Philosophy in Materials Science and Engineering

University of California, Berkeley

Professor Rachel Segalman, Co-chair

Professor Junqiao Wu, Co-chair

Waste heat recovery from the human body provides opportunities to power electronics with a source that is cheap and readily available. Thermoelectrics utilize the Seebeck effect to recover useable electrical energy from this waste heat, but are limited due to material parameters being inversely coupled in the bulk. We investigate the role of novel physics at interfaces in order to develop new fundamental understanding of thermoelectrics. The goal is to discover systems where the Seebeck coefficient and the electrical conductivity are not inversely correlated. We investigate thermoelectric transport in organic-organic systems such as scanning tunneling microscope molecular break junctions on the nanoscale, gold nanocrystal arrays on the mesoscale and polymeric ion and mixed conductors at the macroscale.

The STM molecular junctions studied in this work can provide design rules to positively couple the Seebeck coefficient and the electrical conductance. Since STM molecular junctions are one-dimensional systems, by minimizing the gap between the molecular orbital energy level and the electrode Fermi energy, the power factor $S^2\sigma$ can be optimized. I built a toolbox of chemical structures by first understanding the role of the interface coupling to alkylthiol binding groups of thiophene-based molecules. With this understanding, I designed small molecules based on the monomer unit of donor-acceptor polymers and other conductive polymers. Molecules with very high HOMO levels or low LUMO levels were studied, and the corresponding energy levels were examined using spectroscopic techniques.

I then present our work on scaling these molecular junctions to the macroscale using ligand-exchanged gold nanocrystal arrays. Beginning with a model system of alkanethiols and alkanedithiols, I show that the electrical conductivity scales with ligand length exactly as observed in single molecule junctions, and the Seebeck coefficient follows a similar trend. By showing that gold nanocrystal arrays are a good model platform to scale molecular junctions to the macroscale, I aim to bring the same Landauer transport physics observed in single molecule junctions to macroscale devices. I further investigate the role of different binding groups, where I

find that the character of the ligand binding group directly affects whether the sign of the Seebeck coefficient of the overall array.

Finally, I elaborate on our work with conductive polymers as thermoelectric materials, and specifically investigate the thermoelectric effect in polymers that are solely ion conductors or are capable of both ions and electrons transport. I demonstrate that thermoelectrics based ionic or mixed conduction can be well-described using the developed fundamental equations, and by using these rules we develop positive or negative Seebeck coefficient materials. I present our work on the newly developed thermoelectric AFM technique and how we use the thermoelectric response of different domains to understand the morphology of PEDOT:PSS. By fully understanding the thermoelectric properties of organic-inorganic hybrids from the monomer level, we can extend this same understanding to develop polymer thermoelectrics.

# Table of Contents

Contents

# Chapter 1: Introduction to Thermoelectric Transport at the Nanoscale

## 1.1 Fundamentals of Bulk Thermoelectric Transport

Electrical energy has led to enormous standard of living increases worldwide and is vital to modern society. Energy is primarily generated through heat engines, which although quite efficient, still reject significant amounts of waste heat. For every 1 kilowatt of usable energy generated in the United States, over 2.3 kilowatts of waste heat is rejected.[1] Thermoelectrics are a promising use of materials technology to scavenge this waste heat, utilizing the Seebeck effect, shown in Figure 1.1. Specifically for flexible organic materials, waste heat recovery from the body for useable power is ideal, as organic materials cannot withstand the high operating temperatures of many heat engines. In the Seebeck effect, holes and electrons undergo thermal drift down the thermal gradient $\Delta T$, resulting in a thermoelectric voltage $\Delta V$.[2]

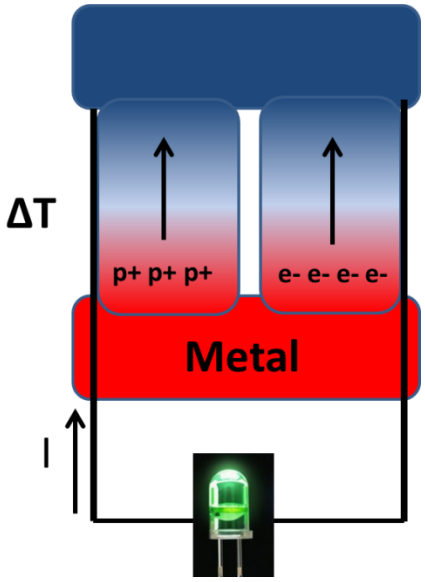


**Figure 1.1:** Under a thermal gradient, both p-type and n-type materials experience charge carrier drift, establishing a voltage gradient. This thermoelectric is wired electrically in series, and thermally in parallel. A thermoelectric module requires both n-type and p-type materials to function.

The module efficiency $\eta$ is related to the thermoelectric figure of merit, zT, and is defined as below in Equation 1.2 for $\eta$. In equation 1.1, zT is the thermoelectric figure of merit, and

consists of the Seebeck coefficient (S), the electrical conductivity (σ) and the thermal conductivity (κ) from both electrons and phonons. In equation 1.2, η is the thermoelectric module efficiency, and consists of zT, the temperature at the hot end, and the temperature gradient. As a heat engine, the thermoelectric efficiency approaches the Carnot efficiency at infinite zT. Thermoelectrics are undergoing renewed interest due to improvements in these materials with reduced density of states, which do not have the same coupling in thermoelectric parameters. On further inspection, the thermoelectric figure of merit is limited by a coupling of S, σ and κ. The electrical conductivity and the thermal conductivity are related by the Weidemann-Franz relation in bulk systems.

$$zT = \frac{S^2 \sigma T}{\kappa_{electron} + \kappa_{phonon}} \tag{1.1}$$

$$\eta = \frac{\Delta T}{T_h} \frac{\sqrt{1+zT}-1}{\sqrt{1+zT}+1} \tag{1.2}$$

## 1.2 Transport in Single Molecule Junctions

One prominent example in the literature to reverse the coupling between the Seebeck coefficient and electrical conductivity for potentially higher thermoelectric power factors is to use reduced dimensional materials, where a positively correlated S and G, the electrical conductance, are expected in a 0-D/1-D density of states.[3] Changing the energy position of a peak in the density of states can lead to enhanced power factors, and has been demonstrated in single molecular junction thermoelectrics, where the molecular HOMO and LUMO levels correspond to the resonance peaks in the density of states.

In a bulk semiconductor or metal with a parabolic density of states, we see that S decreases when σ increases due to doping.[4,5] This limits the power factor $S^2\sigma$ since S and σ are inversely correlated. This coupling of parameters limit ZT to approximately 1 for the best bulk materials, typically heavily doped semiconductors such as $Bi_2Te_3$.[6] Thus, nanostructured materials with 1-dimensional density of states are highly desirable, since at energy levels near the van Hove singularity, S and σ both increase.[3] This energy level alignment leads to a maximum power factor when the electrode Fermi energy is near-resonant with the peak in the density of states. While theoretically simple, this has proven to be very challenging experimentally in inorganics, as designing, synthesizing and characterizing 1-dimensional systems with the Fermi energy near these resonances are difficult. Thus, thermoelectrics have seen a resurgence of interest in the last twenty years, with ZT over 2 for the best nano-structured materials.[6,7]

Single molecule junctions are a system where a single molecule is trapped between two metal electrodes, and the electrical properties of the molecule are characterized. These molecular

junctions satisfy the requirements of a1-dimensional system, where charge transport is confined to the molecular axis, and the location of peaks in the density of states are determined by molecular design.[8] However, there is a lack of understanding at the hybrid metal-molecule interface. Therefore, it is imperative to investigate fundamental design rules to guide the molecular structure of these junctions, thereby enhancing the thermoelectric performance of these hybrid interfaces. Specifically, I aim to understand how the transmission function, which mathematically describes the probability of electron passage, and the thermoelectric properties change with molecular structure and electrode binding group, using a combination of chemistry, experimental measurements and theoretical modeling.

Electron transmission in single molecule junctions can be modeled using Landauer-Bűttiker theory, which describes electron transport in a system where a ballistic conductor connects two semi-infinite electrodes.[9] Three important results can be derived from Landauer-Bűttiker theory. First, there is no scattering of electrons within the electrodes or the ballistic conductor, so any limit to the conductance of the system is due to the interface of conductor and electrode. Secondly, the conductance of this system is quantized, with integer multiples of $2e^2/h$, termed the quantum of conductance $G_0$. Lastly, the transmission through a molecular wire can be modeled with a summation of Lorenztians, as shown in Figure 1.2, with the equation displayed in Equation 1.3. The electrical conductance G will be the value of the electron transmission function evaluated at the Fermi energy of the electrode. The transmission function is maximized when the energy level E of the electron is on-resonant with the molecular energy level $E_m$. The coupling of the molecule to the electrode is represented by Γ.

$$\tau(E) = \sum_m^M \frac{4\Gamma_1\Gamma_2}{(\Gamma_1+\Gamma_2)^2+4(E-E_m)^2}, \quad S = \frac{dln\tau}{dE}|E = E_F \tag{1.3}$$

By using Landauer-Bűttiker, the Seebeck coefficient of the system can also be derived. The Seebeck coefficient is related to the negative derivative of the logarithm of the transmission function evaluated at the Fermi energy.[10] There are two variables essential to modeling a single molecule junction: the offset ΔE between the Fermi energy $E_F$ and the energy of the frontier molecular orbitals $E_{HOMO/LUMO}$, and the molecule-electrode coupling parameter Γ.[11]

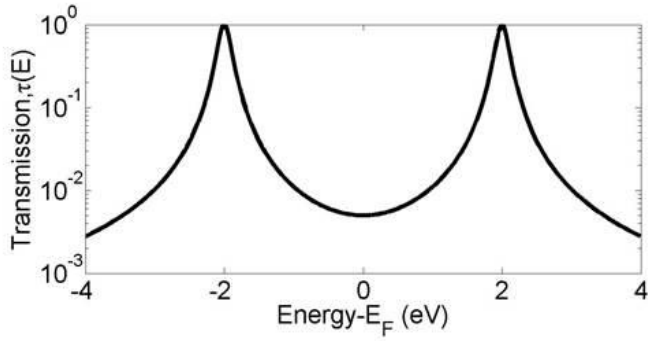


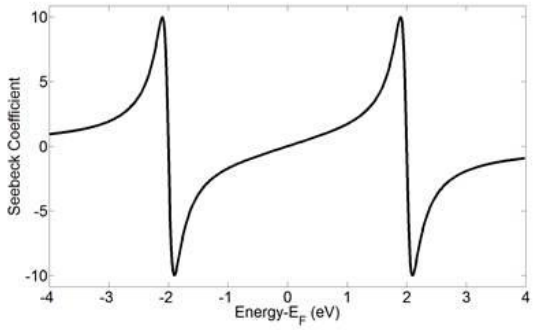

**Figure 1.2:** (Left) Model Lorentzian transmission function with the Seebeck coefficient (right). The Seebeck coefficient is the derivative of the logarithm of the transmission function. By minimizing the energy difference between the Fermi energy and the molecular orbital energies, which correspond to peaks in the transmission functions, S and G can be enhanced simultaneously.

From a theoretical standpoint, we can first investigate the effects of modulating Γ and the position of the Fermi level from the frontier molecular orbitals, ΔE. What I see is quite intuitive, and the results for the power factor are plotted in Figure 1.3. I first observe that in a regime of higher ΔE, where the Fermi energy is distant from a molecular orbital resonance, higher coupling is preferred. In this high ΔE region, the slope of the transmission function is quite low, and so increases in the power factor are seen by broadening the transmission function. However, as ΔE decreases, and the Fermi energy moves to within one electron volt of the frontier molecular orbital energy, our calculation shows that the power factor is optimized with Γ decreasing to order one. This highlights the need for two control knobs in the molecular design to change Γ or ΔE, ideally with a method that can move solely only one parameter.

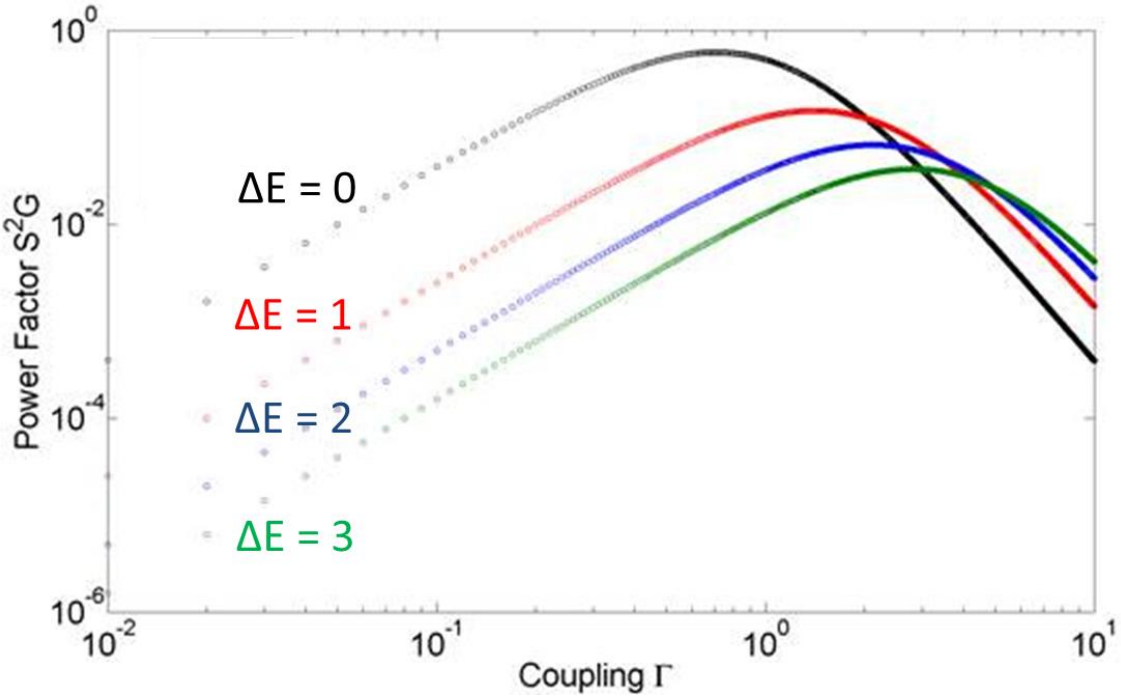


**Figure 1.3:** Power factor of a single molecule junction as a function of coupling and offset of the molecular orbital resonance from the electrode Fermi energy on a log-log scale. Coupling has units of eV, and power factor has units of $W/K^2$ Green: ΔE = 3 eV, Blue: ΔE = 2 eV, Red: ΔE = 1 eV, Black: ΔE = 0 eV

Previous work has shown that the addition of electron donating and withdrawing groups will shift $E_{HOMO/LUMO}$ while leaving the Fermi energy of the electrode unchanged, thus changing

ΔE. The electro active groups used could only change $E_{HOMO/LUMO}$ slightly, and thus the Seebeck coefficient increased only by 10%.[12] Researchers also showed that certain binding groups enhance the electronic coupling Γ of molecule to electrode, enabling molecules with conductances near that of gold.[13]

Building from this previous work from a synthetic point of view, molecular structures were designed drawing from the semiconducting small molecule and gold-ligand literature, allowing us to design systems with control over Γ and ΔE.[14–37] In Figure 1.4 possible molecular structures are drawn with $E_{HOMO/LUMO}$ near the gold Fermi energy, gold ligand binding groups, and electro-active substituents. In the first row of Figure 1.4 are molecular designs with short linear or cyclic molecules. In order to shift $E_{HOMO/LUMO}$ significantly, heterocycles with nitrogen and sulfur heteroatoms are used.[38] Thiophene was identified as a promising candidate with well-known chemistry and a higher $E_{HOMO}$ than typical phenyl molecules. In the second row are certain binding groups to gold. It should be noted that binding groups such as thiols (-SH), amines ($-NH_2$) and trimethyl tins ($-SnMe_3$) exhibit a large range in coupling from molecule to electrode, and is an ideal series to study.[39,40,13] Finally, in the third row are four of the most electron withdrawing or electron donating groups, to further shift $E_{HOMO/LUMO}$ beyond what simple heterocycles can. The methoxy (-OMe) group is a potential molecular fragment which will be used to decorate the molecule backbone. Many elements of this molecular design library will be investigated throughout Chapter 1.

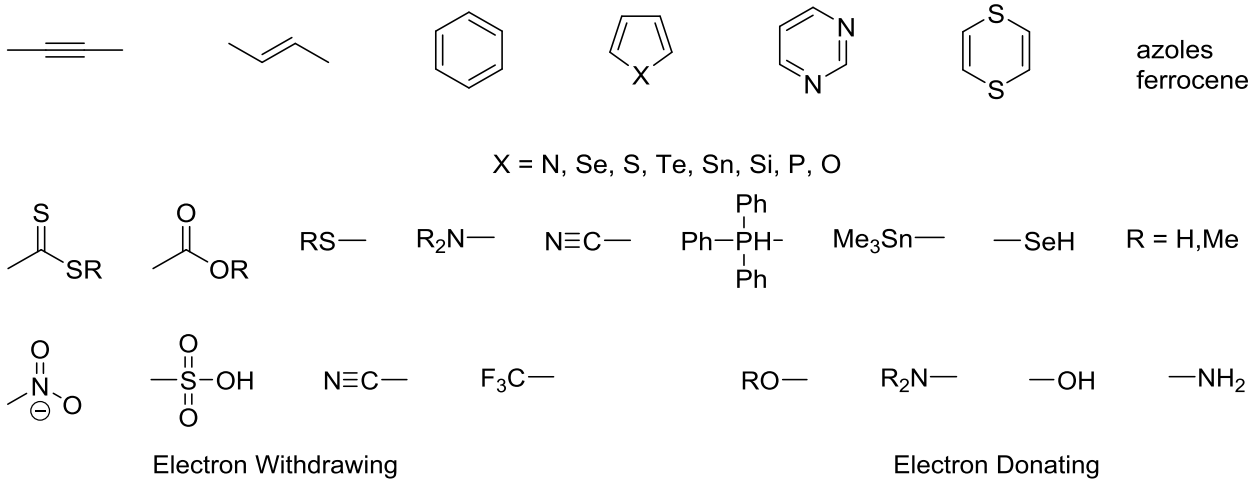


**Figure 1.4:** (Top row) Molecular structures of potential candidates (Middle row) All binding groups to gold (Bottom row) Four of the strongest electron withdrawing or donating groups to provide additional shifts to the HOMO/LUMO energies. By using this structure library, we can design molecular junctions with optimized thermoelectric power factors.

The synthesized molecules are studied using a home-built thermoelectric scanning tunneling microscope break junction.[41] The principles behind the instrument are simple: a sharp gold tip is brought repeatedly into contact with a smooth, evaporated gold film with a self-assembled monolayer of molecules on top. A voltage of five millivolt is continuously applied between the tip and substrate, and the resulting current is acquired and later binned into a histogram. Peaks in the histogram inform us of the molecular conduction, and the breadth of the histogram is an indication of the variety of binding geometries. An example of a conductance histogram is shown below for molecule terthiophene-dithioacetate, a molecular which is key to Chapter 1. The peak at $1G_0$ is the conductance of gold, while the peak at $10^{-3}G_0$ is the conductance of the molecule. A similar process is used to measure the thermoelectric voltage and Seebeck coefficient of single molecules.[12] The substrate is heated, and the tip is kept in contact with a thermal sink at room temperature. Instead of applying a voltage between the tip and the substrate at all times, the voltage bias is set to zero and instead the thermoelectric voltage at open circuit is measured. This voltage is binned into a histogram, and the resulting voltage histograms are recorded as a function of temperature difference, with the Seebeck coefficient being the change in the peak of the voltage histogram with temperature.

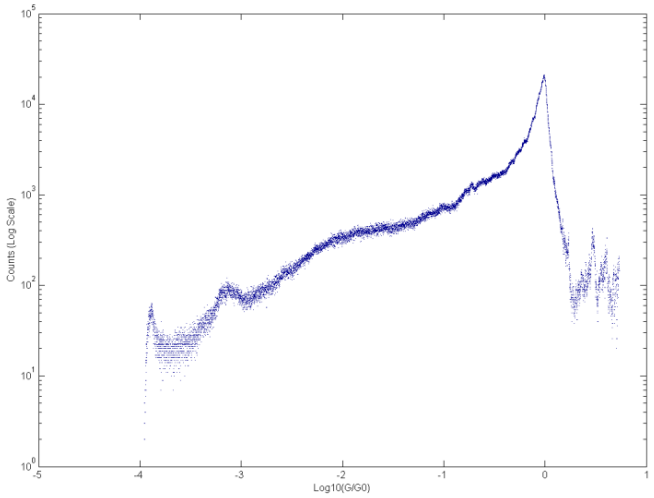


**Figure 1.5:** Representative conductance histogram for molecule OT3 with a voltage bias of 5 mV. Notice the sharp peak at 0, corresponding to the $1G_0$ peak of gold, and the other peak at near -3, corresponding to the molecular conductance of OT3.

## 1.3 Transport in Gold Nanocrystal Arrays

While it is fundamentally intriguing that the conductance and Seebeck coefficient can be decoupled in single molecule junctions, any application of this phenomenon must be able to scale molecular junctions to the macroscale. To do this, I aim to create a model system that is as

similar in composition and energy levels as molecular junctions. I have demonstrated the applicability of gold nanocrystal arrays as a potential platform to scale single molecule thermoelectrics to the macroscale, showing positively coupled S and σ in drop-cast ligand exchanged films mirroring the trends observed in STM-BJ thermoelectrics for thiol binding groups. I have also showed the effects of various conjugated ligands and binding groups of the overall thermoelectric performance of the gold nanocrystal array, and relate this to the transport observed in single molecule junctions.

Nanocrystals are essential to scaling single molecule behavior, since the surface area to volume ratio of nanocrystals means that interfacial properties dominate transport.[42–46] Nanocrystals come in all shapes and sizes, ranging from pyramids, cubes and spheres. [47–55]Nanocrystals can either be insulators, semiconductors or metallic, with many of their optical properties dominated by plasmons at the interface.[42,56,57] Since the vast majority of STM molecular junction measurements are performed with gold tips and surfaces, it is important that we perform our studies on gold nanocrystals to insure maximum similarity. By synthesizing near mono-disperse gold nanoparticles using known methods in the literature, with well-characterized energy levels and plasmonic properties, I can control as many properties in our model system to identify the role of ligand chemistry on the thermoelectric properties.[58–60]

Typically, oleylamine ligands are the as-synthesized ligand for a vast majority of nanocrystals. Oleylamine is a popular ligand choice for synthesis because the long alkene chain enables the nanocrystals to be soluble in organic solvents, and prevent particle aggregation and ripening.[61] However, long alkane ligands result in nanocrystals arrays that are unable to participate in charge transport. A similar result is seen in single molecule junctions of alkanethiols; as the ligand length increases, charge transport is seen to switch from a tunneling regime to a hopping regime.[62] In order for the nanocrystals arrays to display appreciable electrical conductivity, the native oleylamine ligands must be removed and replaced with shorter, conductive ligands such as ethanedithiol or ammonium thiocyanate. It is here that we can replicate the same physics seen in single molecule junctions, and by using solid-state ligand exchanges to our advantage, we can construct systems with many molecular junctions in series and in parallel.

In the past, ligand exchanges were performed in solution, with a biphasic organic and aqueous mixture.[63–68] Nanocrystals with long oleylamine ligands, for example, are soluble in the organic phase and insoluble in the aqueous phase. Shorter hydrophilic ligands then replace the long alkyl ligands at the solution interface, resulting in water soluble nanocrystals. Recently however, solid state ligand exchanges on nanocrystal arrays have been of great interest with the advent of chemical agents such ammonium thiocyanate for removal of long alkyl ligands with short ligands in the film.[69] The removal of these long alkyl ligands results in a nanocrystal array which typically conducts electrons and holes, if the carrier concentrations are high enough. Recently, progress on solid-state ligand exchange techniques have resulted in the ability to partially exchange the ligands within a drop-coated or spin-coated thin film.[70] A scanning

electron microscope example of a film exchanged with this method is presented in Figure 1.6, where the native oleylamine ligand has been replaced with shorter ethanedithiol molecules, resulting in an electrically conductive material. Using these techniques, I exchange the native oleylamine ligands of gold nanocrystal arrays with that of molecules well-studied in the STM literature, and correlate the thermal and electrical transport to STM results and theory.

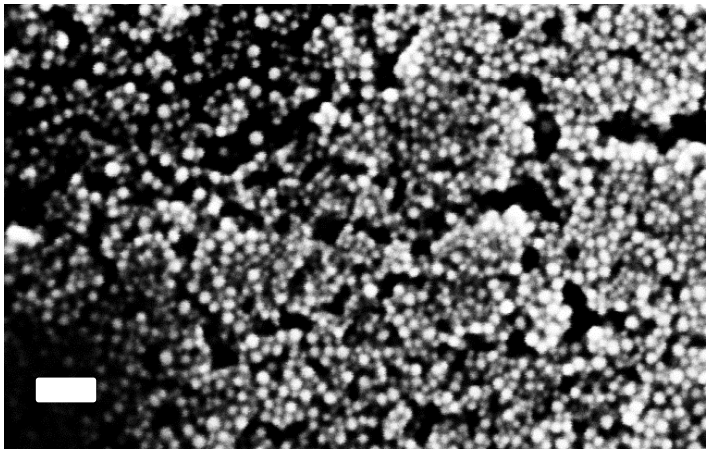

**Figure 1.6**: Au nanocrystal array exchanged with ethandithiol scanning electron micrograph at 200kx magnification. Distinct nanoparticles are still present in the material. This demonstrates that the ligand coat is still protecting the nanoparticle, and so transport is still dominated by the organic-inorganic interface and not by bulk physics. The white scale bar is 20 nm.

Charge transport in these ligand/gold nanocrystal array systems is not well-understood; there is evidence to suggest metallic, semiconducting or hopping transport in these nanocrystal sytems.[71] Regardless of the mechanism of transport, the Seebeck coefficient is dependent on the general Mott relation for thermopower, which does not assume a transport mechanism, and is intimately related to the differential conductivity of the system (Eqn 1.4). Under the Mott formula, the Seebeck coefficient of a carrier in a freely independent scattering system is related to the differential conductivity of the material, as seen in Equation 1.5.[72] The total electrical conductivity of the material is dependent on the density of states as seen in Equation 1.4, while the Seebeck coefficient is related to the derivative of the differential conductivity, as demonstrated in Equation 1.5.[73]

$$\sigma = \int_{-\infty}^{\infty} dE \left(-\frac{dn(E)}{dE}\right)\sigma(E) \tag{1.4}$$

$$S = \frac{\pi^2}{3}\left(\frac{k^2 T}{e}\right)\left(\frac{d\ ln\sigma(E)}{dE}\right)|E_F \tag{1.5}$$

From Equation 1.5, it is important to observe a close similarity between the Mott relation detailing the relationship between differential conductivity and the Seebeck coefficient (Eqn 1.5) and the Seebeck coefficient of a molecular junction (Eqn 1.3).[10] Therefore, I aim to frame the discussion of the thermoelectric transport in gold nanocrystal arrays in a single molecule transport framework, with unconventional electronic density of states caused by ligand-crystal interfaces. Upon binding the electronic structure of the molecule changes, so that new charge transfer states are induced that dominate transport at the interface. These states are termed metal induced gap states (MIGS), as they exist solely due to electron transfer from the metal to the molecules.[74]This difference in transport is illustrated in the following Figure 1.7, where in one ligand/nanocrystal interface there is no metal induced gap state, and in the other there is state facilitating transport, resulting in significantly different Seebeck coefficients and conductivity.

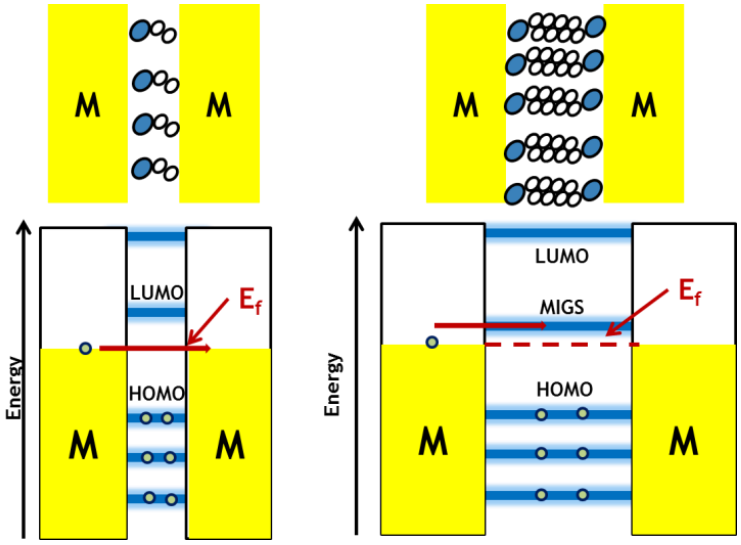


**Figure 1.7**: Schematic for qualitative electron transport in shorter ligands versus longer ligands. Electron transmission from left to right electrode is denoted by a red solid line, the Fermi level is depicted using a dotted red line.(Left) Electron tunneling through the ligand shell between gold nanoparticles, resulting in native p-type transport in gold (Right) Assisted electron tunneling through the molecular metal induced gap state (MIGS) energy level results in p or n-type behavior, depending on the position of $E_f$, as observed in single molecules junctions.

Metal induced gap states are not native to just organic-inorganic interfaces. These states are present whenever there is electron transfer between a semiconductor and a metal, and are known as Schottky barriers.[75–77] This reorganization of the electron density of the states at the interface, or band-bending, is a direct result of different work functions and electron energies in the two disparate materials having equal energy at the interface.[78] The resulting interfacial states are different in energy compared to either the bulk semiconductor or bulk metal. Fermi level pinning is a direct result of the requirement that the semiconductor conduction band must be equal the metal's free electron Fermi energy. The extent of this effect is highly dependent on the chemical

bond between the semiconductor and metal. These same principles from inorganic solid-state physics can be applied to organic semiconductors and metal junctions, where the interfacial state dominates transport since there is no bulk semiconductor. These charge transfer states, or MIGS, are highly dependent on ligand binding geometries, where it has been observed that different theoretical binding conformations can lead to vastly different Seebeck coefficients and conductance values for the molecular junction.[79,80] Within this work, I do not study the effects of binding conformation on the thermoelectric properties of gold nanocrystal arrays; however, custom designed thiol and methylthiol ligands, along with extensive theoretical analysis could probe these effects in the future.

## 1.4 Transport in Conductive Polymers

In the last and final chapter, I investigate the role of organic-inorganic transport at interfaces on the thermoelectric behavior of conductive polymers. Conductive polymers are organic polymers which conduct electricity due to a delocalization of charge. This has lead to a multitude of conjugated polymer structures which mostly display hopping transport of electrons at room temperature.[81] A variety of conjugated polymer structures are presented in the figure below. Notably, poly-3-hexylthiophene (P3HT) is typically used in solar cells, poly-ethylenedioxythiophene (PEDOT) as a transparent conducting thin film. Currently, conjugated polymers are of great interest as thermoelectric materials because the phonon contribution to thermal conductivity is very small at 0.2 W/mK, which is essentially the amorphous limit.[82] Material scientists working with inorganic thermoelectrics often attempt to decrease the thermal conductivity of their material systems with nano-structuring defects to decrease the phonon mean free path.[83]

A conjugated structure is the first and foremost requirement for conductive polymers, as the delocalization of the electron density across the polymer backbone is necessary for sufficiently high carrier mobility for electron conduction. Figure 1.8 depicts four chemical structures, ranging from P3HT which is the quintessential polythiophene uses in bulk heterojunction solar cells, PEDOT which is of great interest for thermoelectric opportunities, and polyacetylene, the first and most well-understood conductive polymer.[84–94] These materials all demonstrate considerable hole mobility, however the intrinsic carrier concentrations are generated by oxidation, and are too low to give appreciable conductivity. In order for these conjugated polymers to have conductivities of near 1000 S/cm, additional charge carriers must be introduced into the system via chemical doping, in direct analogy to doping in silicon.[22,95–98]

Common doping strategies involve additional oxidation of the conjugated backbone with the use of chemicals such as iron(III) chloride, or molecules that are capable of electron transfer such as F4-TCNQ.[98] Regardless of the mechanism of doping, the end result is the formation of polarons or bipolarons, which are cation radicals on the polymer chain.[99] The name polaron is

used to distinguish the fact that these charge carriers are coupled to phonon motion on the polymer backbone. The formation of these charge carriers will typically correspond to a distinct color change that can be monitored via UV-VIS spectroscopy. For example, upon increasing doping level of PEDOT, the polymer turns from a near-transparent film to a dark green film. Control over the doping processes is very important for potential thermoelectric applications, since an optimal carrier concentration is typically approximately $10^{19}$-$10^{20}$ $cm^{-3}$, based on theorectical calculations.

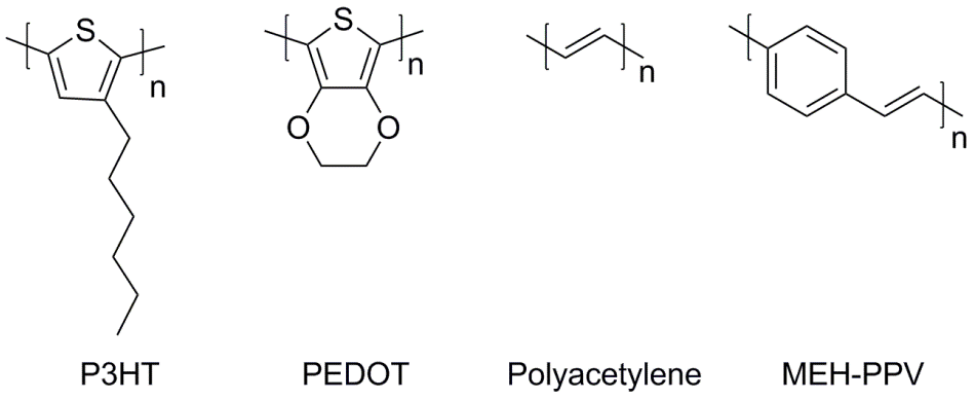


**Figure 1.8**: Chemical Structures of P3HT, PEDOT, polyacetylene and MEH-PPV. P3HT is widely used in organic bulk heterojunction solar cells, PEDOT is a highly conductive polymer used in thermoelectric applications, and polyacetylene was the first conductive polymer discovered. MEH-PPV is a conductive polymer that also exhibits liquid crystal behavior.

Carrier transport in conductive polymers is typically modeled using a temperature dependent hopping transport model where there is no delocalized band structure throughout the material. Instead, there are localized sites within the material that are capable of carrier transport, which models well the crystalline and amorphous domains inherent in the conductive polymer morphology.[98,100–112] The thermoelectric transport can also be modeled as an extension of this model. Equation 1.6 corresponds to the hopping frequency $\omega_{ij}$ between two localized sites *i* and *j* and their associated energy levels separated by a distance $R_{ij}$, and is related to the conductivity observed in the materials. Equation 1.7 is the Seebeck coefficient derived from a hopping model, and is very similar to the Mott thermopower model with an additional temperature dependent term.[72,73,111,113–119] Here, I see that unlike in the previous STM junctions, S and σ are still inversely correlated, resulting in a power factor that must be optimized in terms of electron mobility and carrier concentration.

$$\omega_{ij} = \nu_0 \exp\left(-2\alpha R_{ij} - \frac{E_j - E_i}{kT}\right) \tag{1.6}$$

$$S = -\frac{k^2}{e}(T_0 T)^{\frac{1}{2}} \frac{d \ln N}{dE} |E_f \tag{1.7}$$

Equation 1.6 is the standard hopping transport equation used to model transport in organic semiconductors, where ν is the jump frequency, α is the inverse localization length, R is the distance between the two states, and E is the energy of the states. The rate of transport of electrons from one state to the next is exponentially related to the temperature. Equation 1.7 is how the Seebeck coefficient is related to the density of states in a hopping model, with a temperature dependence of $T^{0.5}$. When these materials become more crystalline and uniform, the localized states will become a delocalized band structure, resulting in the transport modeled by Equation 1.4 and 1.5.

Unlike materials that typically have a delocalized electronic band structure, charge transport in conjugated polymers have a distinct emphasis on morphology. Typically, the more crystalline the polymers are upon making a film, the higher the hole and electron mobility, resulting in more conductive materials. This is especially prominent in materials such as P3HT, where the introduction of a nanofiber morphology that results in high hole mobility.[120] The morphology of PEDOT:PSS is less well-understood due to the uncertain nature of the synthesis; PEDOT is oxidatively polymerized in the presence of PSS, which stabilizes the resultant PEDOT oligomers in water.[121] This dispersion of micron sized particles, when cast form a smooth highly conductive film, and when treated with a high boiling point solvent like DMSO results in a thousand times increase of electrical conductivity. The morphology of PEDOT:PSS is highly debated, and I investigate this issue using a custom-developed scanning Seebeck AFM technique.

Using atomic force microscopy to investigate the surface structure of polymers is common-place, due to the ease of obtaining nano resolution.[122] Thermoelectric imaging has been sparsely used throughout the literature, and is primarily used to detect defects and inhomogeneity throughout the microstructure of the inorganic material. In collaboration with NT-MDT, we co-developed a tapping thermoelectric AFM imaging technique which we use to probe the structure of PEDOT:PSS, and observe two domains, one being the PEDOT rich domain, the other being the PSS rich domain.

PEDOT:PSS, besides being a highly conductive conjugated polymer, is also a polyelectrolyte in the presence of water due to having polystyrenesulfonate. Polyelectrolytes are polymers where each monomer unit contains an ionic group.[51,123,124] The ionic group for Nafion and PSS is a protonated sulfonate group, but by using different metal containing compounds such as sodium hydroxide, the sodium form of Nafion and PSS (Na-Nafion, NaPSS) can be synthesized, and have many applications.[54,77,125] Nafion is a proton conductor with a conductivity greater than 1 mS/cm, and a negligible electrical conductivity.[126] Since Nafion has an electrical conductivity close to Teflon, it typically is used in applications such as fuel cells and ion sensors. In these ion conductor materials, conductivity has been experimentally observed to change over three orders of magnitude between 0% relative humidity and fully humidified environments, due to water uptake.[127]

While the magnitude of the thermoelectric power factor of electrons is well-understood, the thermopower of ions is still not well-established, and I will discuss various theories to understand thermoelectric transport of ions in Chapter 4. Devices that use the movement of ions to set up a voltage gradient are termed thermogalvanics, and have been studied along with thermoelectrics since 1970.[128] Typical thermogalvanics that are studied are inorganic materials which transport ions at temperature over 300°C, and display Seebeck coefficients over 1 mV/K.[88,129–134] These thermogalvanics have the same cycling issues as batteries, since operation of the device requires deposition of ions that can lead to bridging dendrites. As stated before, the Seebeck coefficient of these devices is not well-understood. It is well known that the Seebeck coefficient is related to the transport of entropy, but in these complex ionic systems, it is difficult to ascertain all the sources of entropy.[135] In Chapter 4 I attempt to address all the sources of entropy in polymer ion conductors to pinpoint the major contributions to the large Seebeck coefficient.

Throughout this work, I emphasize transport at all length-scales to demonstrate that charge mobility and defects at every length scale affect the overall performance of thermoelectric materials. It is important to note that the overall theme is to identify physical phenomenon where the Seebeck coefficient and the carrier conductivity can be simultaneously improved. In single molecule systems, transport is no longer dictated by conventional bulk semiconductor physics. Ion transporting systems do not follow semiconductor physics; rather the description of the Seebeck coefficient follows from electrochemistry. These systems are far from commercialization and implementation; however, investigation of these systems reveals exciting new transport physics and demonstrates decoupling of fundamental thermoelectric properties.

# Chapter 2: Elucidating Molecular Design Rules for High Power Factor Molecular Junctions

Adapted from W. Chang, C. Mai, M. Kotiuga, J. Neaton, G. Bazan, R. Segalman. Controlling the Thermoelectric Properties of Thiophene-derived Single Molecule Junctions. *Chemistry of Materials,* **26***,* 7229–7235 **(2014)**. Reproduced by permission of The American Chemical Society

## 2.1 Thermoelectricity in Molecular Junctions

In recent years single molecule junctions have provided scientists with a unique manner to probe charge dynamics at the molecular scale and in turn understand how to tune the thermoelectric properties. A large interest lies in controlling and maximizing the power factor of molecular junctions: $S^2G$, where S is the Seebeck coefficient, also known as the thermopower, and G is the electrical conductance. S and G are inversely correlated in macroscopic materials, challenging researchers to maximize thermoelectric efficiencies by decoupling these two phenomena.

In junctions formed with small molecules strongly-bonded to two electrodes, transport is typically dominated by tunneling, the so-called Landauer transport regime.[136,137] In this coherent tunneling regime, the relative level alignment of the frontier orbital to the lead Fermi energy, $E_F$, and the nature of the bond, including the coupling of this level to the lead, $\Gamma$, dictate the magnitude and sign of G and S. Assuming the transmission function is an approximately Lorentzian function peaked at the frontier orbital resonance energy with broadening $\Gamma$, G increases with $\Gamma$, and as the resonance moves closer to $E_F$.[9] On the other hand, S is proportional to the negative logarithmic derivative of the transmission function with respect to energy, evaluated at $E_F$, and increases as $\Gamma$ decreases and the frontier orbital resonance moves closer to $E_F$.[138,139] Therefore, it is possible to couple S and G in new ways in a molecular junction and for Lorentzian resonances, to maximize the power factor with junctions having a transmission function featuring a narrow frontier orbital resonance close to $E_F$. Experimentally, both S and G have been shown to increase simultaneously with energy level alignment.[9] Positioning the energy of the frontier highest occupied or lowest unoccupied molecular orbitals (HOMO or LUMO) closer to the $E_F$ of gold will result in a simultaneous increase in both S and $\sigma$.[140,141] Other methods shown to control $S^2G$ are changing the highest occupied molecular orbital (HOMO) energy position,[142–145] by varying binding groups,[13,138,142,146–150] molecular design, and choice of metal contacts.[137,151–154]

We propose a series of experiments to construct rules for designing molecular junctions with high thermoelectric performance based on two parameters in the transmission function: the offset of $E_{HOMO/LUMO}$ from $E_{Fermi}$ ($\Delta E$), and the molecular electrode coupling ($\Gamma$). The two studies

presented in this chapter will first focus on controlling the molecular electrode coupling Γ, and then discuss rules to control ΔE. We separate the molecular backbone from the binding groups, and investigate the role of each fragment to the thermoelectric properties. We expect changes to the molecular backbone to change ΔE while different binding groups would strongly alter the electrode coupling Γ, and to a lesser extent, ΔE. From these experiments, we construct fundamental design rules to tailor transmission functions to maximize thermoelectric properties of these hybrid metal-molecule interfaces.

In collaboration with chemists and theoretical physicists, we synthesized, measured and modeled an initial series of thiophene-based molecular junctions that exhibit a higher thermoelectric performance than any previous molecule studied, due to better molecular orbital energy alignment. We show that the addition of a heterocycle decreases ΔE, thereby increasing the power factor. We also illustrate a method to decrease the coupling of molecule to electrode by incorporating insulating alkyl linkers to the molecular design. We can compare the difference between an increase in length with conjugated and non-conjugated linkers, and see a strong difference in the Seebeck coefficient.

Extending these promising results, we then synthesize and measure an additional series of molecules, designed with the goal to align $E_{HOMO}$ to the electrode Fermi energy using molecules based on small molecule organic electronics with low LUMO energies and high HOMO energies. Additionally, we utilize the design rules from our theory to tailor molecules with either positive or negative Seebeek coefficients. Ultraviolet photoelectron spectroscopy and ultraviolet-visible absorption experiments are used to quantify the HOMO/LUMO energy levels of these molecules relative to the gold Fermi energy, confirming the design rules put forth. After these experiments, we hope to have enough fundamental understanding of the hybrid interface not only to tailor transmission functions, but to extend this understanding to hybrid interfaces in bulk materials.

## 2.2 Experimental Thermoelectric Results of Thiophene-based molecules

The energetics of the junction was manipulated through modification of the molecular backbone while leaving the binding group constant. For this series of molecules, the thioacetate binding group was selected as it binds strongly to gold. Due to the strength of the S-Au chemical bond, there is a large charge localization at the metal-molecule interface leading to a gateway state, which is an intermediary state coupling the lead to the molecular backbone. The effect of the gateway state under variation of the molecular backbone was examined. The electron transport through these junctions can be separated into two sequences: the transport into the molecule through the binding group, and transport within the molecule itself. It has been experimentally shown that the binding groups on each molecule dominate the coupling of the molecule to the electrode, resulting in varying peak breadths within the calculated transmission

functions of these junctions.[155–157] The strength of the bond coupling the molecule to the gold electrodes determines the energetics of the metal-molecule interface, which has strong implications for S and G.

The concept that differences in molecular design can cause strong changes in the Seebeck coefficient of the molecular junction was examined. Evidently, the molecular design dictates the modes of electron transport within the channel. Thiophene based molecular junctions, shown in Figure 2.1, were used to investigate this concept through two series, one consisted of thiophene molecules with increasing alkyl linker lengths (TA series: T1, TA2 and TA3) and the other with increased thiophene π-conjugated units (OT Series: T1, OT2 and OT3). Thiophene was chosen to study the effects of a higher HOMO energy, since thiophene has a HOMO energy closer to the Fermi energy of gold than benzenedithiol.[158,159] By increasing the alkyl linker length in TA2 and TA3, the coupling of the molecular backbone and gateway state is expected to be reduced, leading to localization of charge on the thiophene core and a weaker peak in the transmission function gateway state. An increase in the conjugated backbone in OT2 and OT3 was designed to investigate the effects on conjugated molecular length coupling to a gateway state for a HOMO positioned very close to $E_F$. Detailed synthesis of all these molecules can be found in the experimental methods section. The experimental conductance and Seebeck coefficient measurement was performed in a custom built STM-break junction setup, with experimental details provided in the methods section below. Measurements of G for the molecular series T1, TA2, TA3 and T1, OT2, OT3 are presented which show a decreasing trend with length in both cases. S was measured for the same molecular series T1, TA2, TA3 and T1, OT2, OT3. The OT series showed a positive, increasing S with length and the TA series: a positive S which decreases with length. A tight-binding model with a gateway state was employed to capture all of the experimentally observed trends reported.

The conductance of a single molecule junction as a function of length is viewed as a tunneling barrier between two electrodes, with an exponential decay parameter termed β, which differs based on molecular backbone. To confirm that this holds true, the electrical conductance of molecules T1, TA2, TA3, OT2, and OT3, as shown in Figure 2.1, were investigated. Experimental results for the conductance as a function of molecular length are presented and these results are compared to β decay parameters of known conjugated and non-conjugated systems. The molecular length is defined to be from sulfur to sulfur between the two thiol terminations when the molecule in a relaxed geometry that is as symmetric and straight as possible. The conductance of T1, TA2, TA3, OT2 and OT3 are $0.0075G_0$, $0.0035G_0$, $0.002G_0$, $0.0031G_0$ and $0.0007G_0$ respectively. These length dependent values compare well to similar thiophene molecules in the literature.[158] This shows that T1 has a similar conductance compared to more commonly studied molecules such as benzenedithiol ($0.011G_0$) or benzenediamine ($0.0064G_0$). The experimental results indeed show an exponential decay in electrical conductance with molecular length, with T1,TA2 and TA3 having a $\beta_{TA}$ decay parameter of 3.15 $nm^{-1}$ and T1 OT2 and OT3 having a $\beta_{OT}$ decay parameter of 2.96 $nm^{-1}$ . Since it has been shown

that a non-π conjugated system has a β decay parameter of 9.363 $nm^{-1}$,[160] while a π-conjugated system has a β decay parameter of 2.9 $nm^{-1}$,[158] it can be inferred that additional non-π conjugated linkers to a π- conjugated system results in behavior between that of a fully conjugated π-conjugated system and a non-conjugated system, due to partial delocalization of the electron over the molecule.

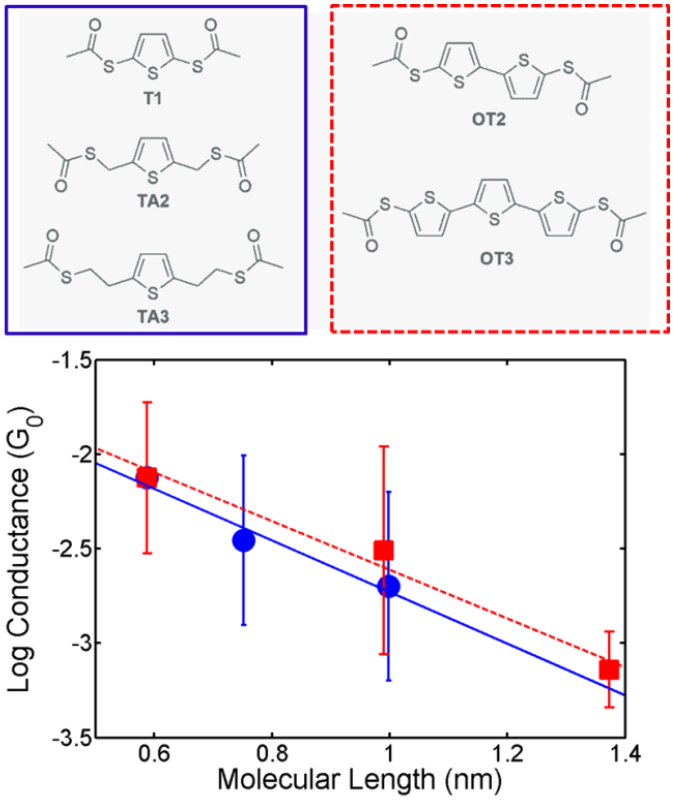


**Figure 2.1:** (Top): Chemical structures of molecule measured. The thioacetate binding group will be referred to as AcS (a) T1: (S,S'-thiophene-2,5-diyl diethanethioate), (b) TA2: (S,S'-thiophene-2,5-diylbis(methylene) diethanethioate), (c) TA3: (S,S'-2,2'-(thiophene-2,5-diyl)bis(ethane-2,1-diyl) diethanethioate (d) OT2: S,S'-([2,2'-bithiophene]-5,5'-diyl)diethanethioate (e) OT3: S,S'-([2,2:5',2"-terthiophene]-5,5"-diyl) diethanethioate (Bottom): Electrical conductance of molecular junctions with T1, TA2, and TA3 (blue circles) and T1 and OT2 (red squares) plotted as a function of molecular length. The data is fit to a standard exponential β-decay model. The $\beta_{TA}$-decay parameter is calculated to be 3.15 $nm^{-1}$, and $\beta_{OT}$-decay parameter is calculated to be 2.18 $nm^{-1}$, and shows that increasing alkyl linkers results in a β that compares in between the β of π-conjugated systems and a non-conjugated systems. The data points are the peak in the conductance histogram, and the error bars represent the full width half maximum of the histogram peaks, and do not represent instrumental error, but rather variances in binding geometry.

Additional information about the effects of π-conjugated versus non-conjugated molecular fragments on electron transmission can be obtained from measurement of the Seebeck coefficient. Molecules in the TA series have an increasing number of alkyl linkers between the molecular ring and the binding group. This is intended to increase the spacing between the aromatic system and the electrodes, in order to isolate the molecule energy levels from the electrodes, which has been already seen to decrease the conductance more rapidly than the addition of conjugated units. The blue line in Figure 2.2 shows the Seebeck coefficient measurements of the TA series with respect to molecular length, and compares these values to benzenedithiol (black). The Seebeck coefficients for T1, TA2 and TA3 are 6.83, 3.01, and 2.2 μV/K respectively. By fitting these numbers to a linear regression, the calculated slope is -10.6 μV/(K nm). In pure alkanethiol systems with no π-conjugation in the literature, the slope in the Seebeck coefficient is -5.6 μV/(K nm).[161] This demonstrates that the trend with introduction of an alkyl linker to a π-conjugated system is not the same trend observed in solely non-conjugated or conjugated systems. As suggested with the length trend in conductance, the Seebeck coefficient decrease is larger than with pure alkane systems, and may be due to electron delocalization across the molecule, resulting in a system between that of a purely alkyl non-π conjugated system and a fully π-conjugated system.[161]

In comparison, the Seebeck coefficients of oligothiophenes were also measured, where the increase in molecular length was due to additional π-conjugated systems, and not alkyl spacer groups. The red trend in Figure 2.2 shows that the Seebeck coefficients of T1, OT2 and OT3, which have an increase in conjugated molecular length, compared to molecules in the blue trend which have increases in non-conjugated molecular length. By increasing the molecular π-conjugation length, an increase in the Seebeck coefficient was observed. The Seebeck coefficients of T1, OT2 and OT3 are 6.83, 7.49, 14.84 μV/K respectively, with a calculated slope of the Seebeck coefficient with respect to molecular length of 10.08 μV/(K nm). Oligophenyls with amine and thiol binding groups, a similar system studied in the literature, also demonstrate an increase in Seebeck coefficient with increasing molecular length. The slope of the Seebeck coefficient with respect to molecular length for oligophenyldithiols is 6.9 μV/(K nm).[161] The larger Seebeck coefficient measured for T1 (6.83 μV/K) compared to benzenedithiol on this system (4.8 μV/K) shows the effect that using heterocycles with better HOMO energy alignment to the gold $E_F$ increases S without lowering G.

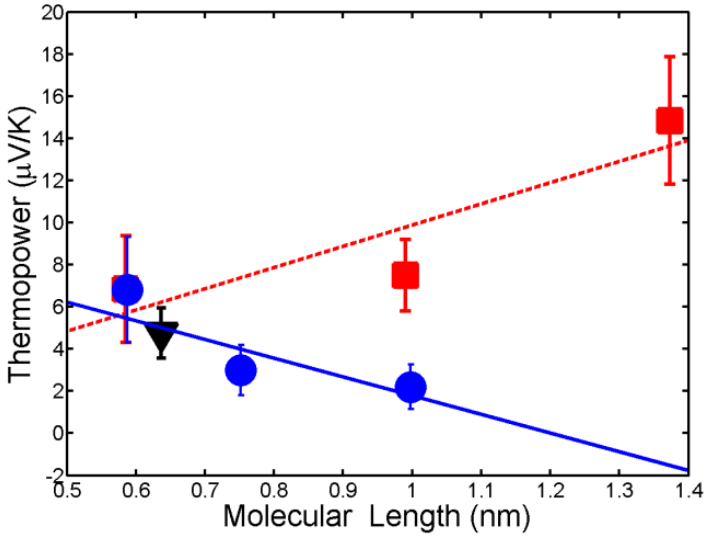


**Figure 2.2:** Seebeck coefficient of T1, TA2, TA3 (blue circle) and T1, OT2, OT3 (red square). T1 is in both TA and OT, and is represented as a red square on a blue circle. Benzenedithiol was also measured in this setup (black triangle). The slope of the alkylthiophene blue line is -10.6 μV/(K nm) and corresponds well to literature trends on the Seebeck coefficient of pure alkanethiol junctions. The slope of the oligothiophene red line is 10.08 μV/(K nm), and is nearly double that of oligophenylthiols, the nearest comparable system.

## 2.3 Theoretical Modeling of Alkyl Linkers

To quantitatively model transport properties of a junction, there are two key ingredients: an accurate representation of how the molecule binds to the leads (junction geometry more generally), and a quantitative description of the level alignment of the molecular orbital resonance energies with respect to the lead Fermi energy.[138] For thiol-terminated molecules, broad conductance histograms are measured compared to other terminal binding groups,[162] resulting from the sensitivity of conductance with respect to binding geometry which is highly variable due to the non-directionality of the S-Au bond,[163] posing challenges to theory in developing representative junction geometries. Additionally, even if suitable model geometries existed, first-principles density functional theory (DFT) approaches are widely known to lead to incorrect level alignment,[164,165] resulting in an artificially low tunnel barrier and an overestimation of the conductance by an order of magnitude or more.[166] While GW-based self-energy corrections can improve the description of level alignment in the junction; corrections come at considerable computational expense, even for well-defined geometries.

We use a physically-motivated tight-binding model with a minimal number of parameters, following previous work on strongly bound molecules;[158,167] our model is sufficient

to explain measured trends in junction G and S, and provides a basis for interpreting future *ab initio* calculations. In our tight binding model, the leads are coupled via a broadening Γ to a gateway state, at energy $E_s$, localized on the thiol; this gateway state is, in turn, coupled to the molecular backbone at energy $E_b$ with off-diagonal coupling strength τ. For molecules with N thiophene rings, we introduce N sites along the backbone with inter-ring hopping parameterized by δ. Using these parameters, the Hamiltonian, H, for OT2 can be expressed as

$$H = \begin{pmatrix} E_s - i\frac{\Gamma}{2} & \tau & 0 & 0 \\ \tau & E_b & \delta & 0 \\ 0 & \delta & E_b & \tau \\ 0 & 0 & \tau & E_s - i\frac{\Gamma}{2} \end{pmatrix}$$

As noted in previous works on related systems,[158] the gateway state arises from the strong S-Au bond formed in the absence of the hydrogen allowing for strong hybridization and large charge localization. For example, gateway states can be seen in the transmission calculations of alkanedithiols of increasing length in the work of Li *et. al.*[168] It can be shown that the positive and decreasing S as a function of length for the alkylthiophene molecular series T1, TA2, TA3 is a direct consequence of this gateway state. Initially the parameters in the model were fit to the measurements of the oligothiophenedithiol-Au junction (T1, OT2, OT3) G and S; the model was then extended to incorporate the addition of $CH_2$ groups in order to the capture the behavior observed from TA2 and TA3.

To model the OT series, the data were fit to the model varying the parameters Γ, $E_s$, $E_b$, δ, and τ, and the experimental trends are replicated. As shown in Figure 2.3, the Seebeck coefficient increases with length and the conductance decreases with exponentially length, with a decay constant ranging from 3 -5 $nm^{-1}$, comparable to reported values for other conjugated backbones. The T1 transmission function, shown in red in Figure 2.3(b), resulting from the best-fit parameters clearly indicates features associated with the gateway state just below $E_F$.

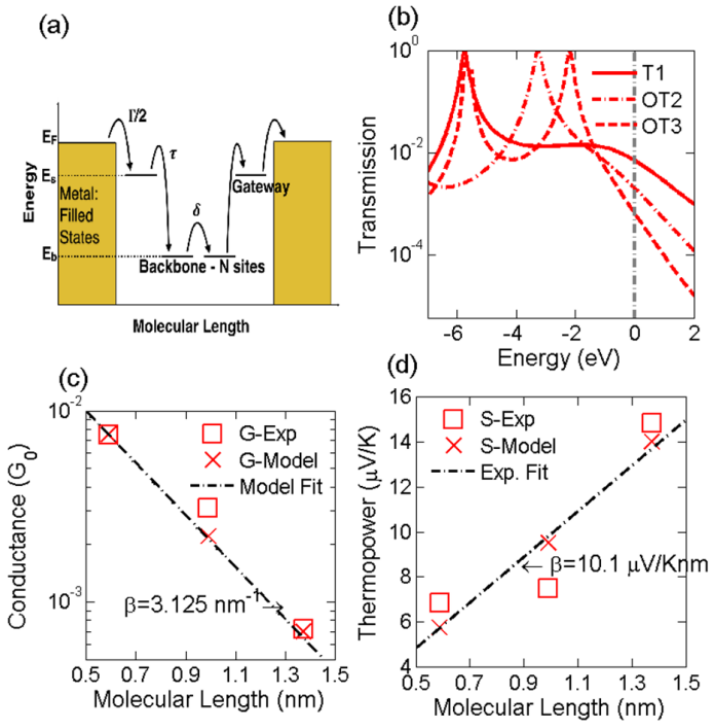


**Figure 2.3:** (a) Schematic of tight-binding model being used with multiple sites along the molecular backbone. (b) The calculated transmission values for the set of parameters: $\Gamma$= 5.32 eV, $E_s$ =-0.98 eV, $E_b$ = -5.54 eV, $\delta$ = -2.40 eV, and $\tau$ = -0.83 eV. (c)The corresponding conductance values as predicted by the model. (d) Calculated Seebeck coefficient values compared to experiment.

For the molecules TA2 and TA3, the T1 Hamiltonian is extended to incorporate more sites representing additional $CH_2$ groups by allowing the position of the gateway state, $E_s$, to move up in energy toward $E_F$ and the value of $\tau$ to decrease. The changes in these two parameters physically represent a decrease in overlap between the charge density on the thiol and the thiophene frontier states. Under this decoupling along the molecule, represented by the decrease in $\tau$, the gateway state can interact more strongly with the gold resulting in a shifted gateway state energy. Using the $\Gamma$ and $E_b$ from the OT series the model is fit via $E_{s,TA2}$, $E_{s,TA3}$, $\tau_{TA2}$, and $\tau_{TA3}$. In the model, it is observed that the decrease in $\tau$ contributes primarily to the decrease in the conductance as a function of length, where the shift in energy of the gateway state is the crucial element to capture the decrease in Seebeck coefficient as a function of molecular length. The conductance and Seebeck coefficient values from the model are compared to experiment in Figure 2.4(b) and Figure 2.4(a) the transmission curves, which again clearly show the resonance due to the gateway state just below $E_F$ whereas the HOMO resonance is a few electron volts below $E_F$. If a different starting point from the OT series is used, the same trends are produced with similar error bars.

Other efforts to capture this behavior for reduced tight-binding models without gateway states fail. With a single level alone the only way to achieve a decreasing G and S with length is to move the frontier orbital away from $E_F$ by a very large unphysical energy shift. If we introduce a second level, a set of parameters for which S is positive and decreasing with length can be found; however, the conductance increases with length – another unphysical result. Only this tight binding model with a gateway state is able to recreate the trends observed in experiment.

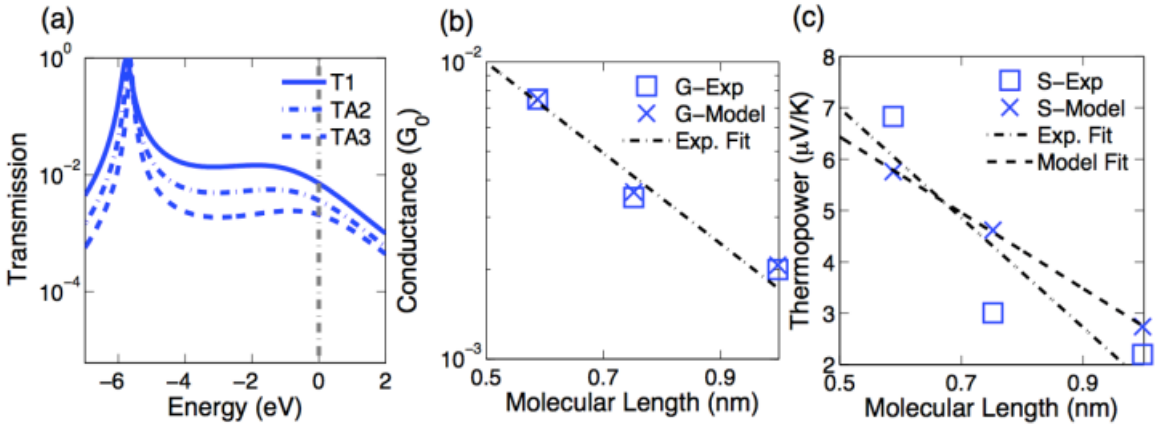


**Figure 2.4:** (a) The transmission curves for T1, TA2, TA3 with the parameters: $\Gamma$ = 5.32 eV, $E_b$ = -5.54 eV, and $E_s$ = -0.98, -0.59. -0.10 eV, $\tau$= -0.83, -0.68, -0.58 eV for T1, TA2, TA3 respectively. (b) Conductance predicted by the model and compared to experiment. (c) The Seebeck coefficient from the model compared to the experimental values.

## 2.4 Concluding Remarks on Effect of Alkyl Linkers on Electrode Coupling

Thiophene junctions have a higher Seebeck coefficient and similar conductance due to closer alignment of the HOMO energy with the gold Fermi energy. By incorporating alkane linkers of increasing length between the binding group and thiophene, the molecular orbitals are localized, resulting in both a decreasing conductance and Seebeck coefficient. In oligothiophene junctions with increased conjugated units, an increase in the Seebeck coefficient was observed. This increase in Seebeck coefficient is attributed to a shift in the HOMO energy closer to the Fermi energy of gold, along with a sharpening of this peak in the transmission function. This highlights the needs for design rules, as an increase in molecular length will result in a decrease of conductance, but may increase or decrease the Seebeck coefficient, depending on the molecular design and the presence of a gateway state.

## 2.5 Finely Tuned Heterocyclic Molecular Junctions

With our newly gained experimental and theoretical understanding on how to control the molecular coupling, we turn to controlling the molecular junction ΔE, the energy difference between HOMO/LUMO and the Fermi energy. We seek to design high power factor single molecule junctions with thiol-based binding groups, as these are well-understood theoretically.[45,169,170] From a design perspective, we desire short aromatic molecules with HOMO levels close to the Fermi level of gold for p-type junctions, and LUMO levels close to the Fermi level of gold for n-type junctions with near-resonant energy levels for maximum thermoelectric power factor. Short aromatic molecules are advantageous since the electrical conductance decays exponentially with molecular length, and conjugated units have been shown to decay less with increasing length than non-conjugated units.[39,163,171–174,62,175] From the vast literature of small molecule organic electronics, we can design thiophene based heterocycles with various chemical substitutions to the ring.[14–37]

Figure 2.5 below shows the five molecules studied, with molecules M1 (bis(methylthio)dihydrothienodioxine) and M2 being more electron rich and with HOMO levels closer to gold than M3 (benzenedithiolacetate), and hence one would expect enhanced p-type thermoelectric transport.[16] Molecules M4 and M5 (bis(methylthio)benzothiadiazole) are more electron poor and with LUMO levels closer to gold than M3, which will lead to a decreased Seebeck coefficient or switch in the sign of the Seebeck coefficient, denoting a change from HOMO-mediated transport to LUMO transport.[19,20] While the molecules have different binding groups, varying from thiol, thioacetate and thiomethyl, we shall see that the effect on the molecular HOMO/LUMO are minimal compared to the aromatic heterocycle. Experimental measurements of benzenedithiol and benzenedimethylthiol show minimal differences in conductance, even accounting for slight differences in binding geometery.[8,174,176–179]The HOMO/LUMO energy levels are then measured using a combination of UPS, UV-VIS and CV, so that accurate trends of the Seebeck coefficient with regards to molecular energetics can be ascertained.

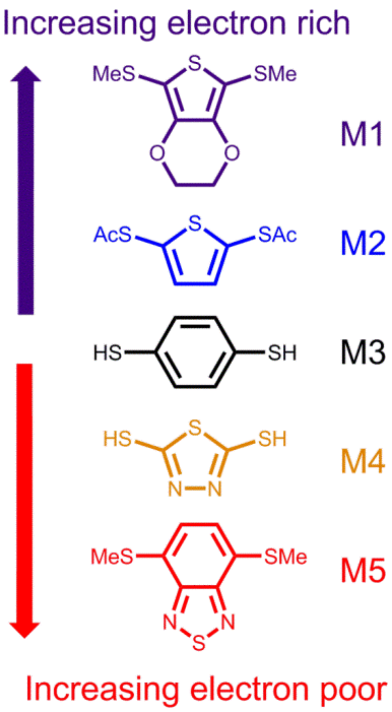


**Figure 2.5**: Synthesized molecules listed from most electron rich to most electron poor. M3 demonstrates p-type transport, with a Seebeck coefficient of 4.8 uV/K. M1 and M2 are designed to be more electron rich than M3, and should be expected to have HOMO energy levels closer to gold than M3. Molecules M4 and M5 are electron poor compared to M3, and so should have LUMO energy levels closer to gold than M3. The more aligned the energy level of the dominant transport orbital to the Fermi energy, the higher the thermoelectric power factor. This color scheme will be used as a legend for all future figures in this chapter.

## 2.6 UPS and UV-VIS as a Method to Assess Energy Alignment

In order to accurately measure the energy difference between the gold Fermi level and the molecule HOMO level for this study, we turn to ultraviolet photoelectron spectroscopy (UPS). By analyzing the UPS spectrum near the Fermi edge, also known as zero binding energy, and observing the onset of the intensity spectrum, one can calculate the energy difference of the molecular HOMO level and that of the gold Fermi level, where the difference will be termed $E_{HOMO}^{F}$.[99,180–189] This term is extremely important since the slightly modified binding thiol binding groups between M1-M5 (thiol, thioacetate, thiomethyl) can lead to changes in the molecule HOMO/LUMO level upon binding and a modification of the gold work function. The UPS results are shown in Figure 2.6, where each color curve corresponds to the offset UPS spectrum of the respective molecule on gold/mica in Figure 2.5.

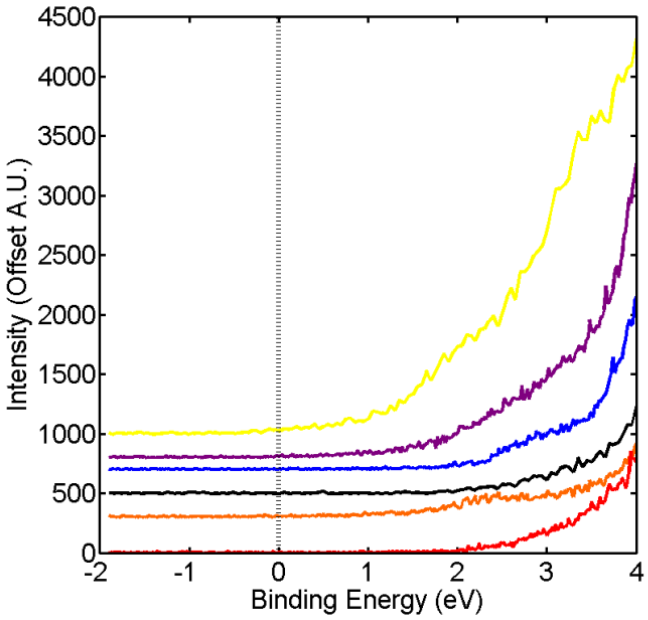


**Figure 2.6**: Ultraviolet photoelectron spectroscopy on molecules M1-M5 drop-coated ontp gold evaporated on mica, offset for the sake of clarity. The color scheme is the legend for molecules depicted in Figure 2.5, with the addition of the yellow spectra being that of the bare gold surface. As expected, at zero binding energy the bare gold spectra demonstrate significant intensity above the baseline, indicating finite density of states. The more electron rich the molecule is, the lower binding energy the absorption onset occurs at, signifying a smaller difference between the HOMO energy level and the Fermi energy of gold ($E_{HOMO}^{F}$).

From the UPS measurement, we are able to measure $E_{HOMO}^{F}$ and observe a noticeable trend from molecules M1-M5. One can observe that starting with M1, the most electron-rich molecule, by decreasing electron density one sees a shift of the onset binding energy to higher energies. This signifies that the more electron poor the molecule is, the lower the HOMO level relative to gold, which results in a monotonically larger $E_{HOMO}^{F}$. The onset for molecule M4 was calculated from the second onset; two separate peaks can be found in the complete UPS spectrum for M4. The values for $E_{HOMO}^{F}$ are shown in Table 2.1.

By using UPS to measure $E_{HOMO}^{F}$, we are able to quantitative assess the energy levels of the molecular HOMO in relation to gold; however, this only explains half of the energy landscape of the molecule, and the energy difference of the gold Fermi energy from the molecular LUMO level ($E_{LUMO}^{F}$) is very important. The ideal tool and experiment for determining $E_{LUMO}^{F}$ would be inverse photoelectron spectroscopy, but the energy resolution for these measurements are poor (~1 eV) and instruments are home-built and few in number.[190–192] For the purpose of this work, we will calculate $E_{LUMO}^{F}$ by measuring the energy of the HOMO-LUMO gap ($E_{HOMO\text{-}LUMO}$) and subtracting $E_{HOMO}^{F}$. An ideal measurement of the HOMO-LUMO gap would be when the molecule is bound to gold, as in the case of the UPS measurement.

However, gold is not an appropriate substrate for cyclic voltammetry or solid-state UV-VIS experiments due to electrode polarization.[193–196] Therefore, measurement of $E_{HOMO-LUMO}$ was performed using through solution cyclic voltammetry and solution UV-VIS absorption. Figure 2.7 depicts the UV-VIS absorption spectra of M1-M5. Cyclic voltammetry was performed, and curves show instability of the molecules upon reduction, but for those molecules within the energy window of the CV experiment, we find good agreement between the $E_{HOMO-LUMO}$ measured. Thin film absorption spectra on glass demonstrate an increased baseline, most likely due to polaron formation in these films. The values for $E_{LUMO}^{F}$ as obtained from solution UV-VIS absorption in THF are recorded in Table 2.1.

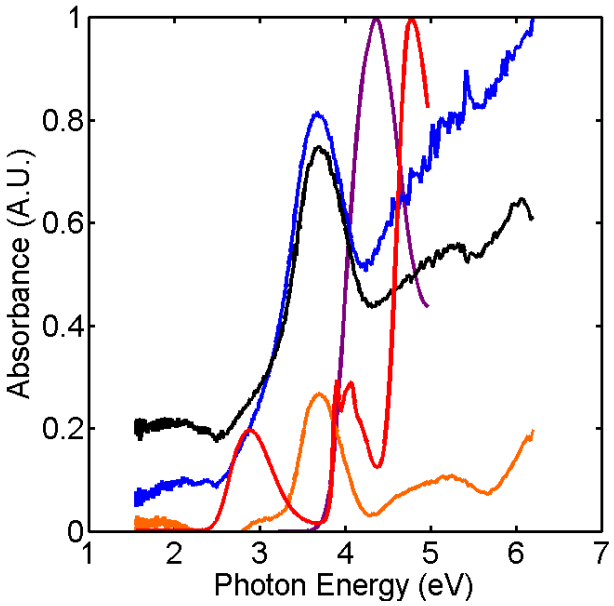


**Figure 2.8**: Solution UV-VIS of M1-M5 in THF. The same color scheme in Figure 2.5 for the molecular series applies here. The absorption onset is obtaining by fitting a slope to the onset and calculating the intersection with baseline. The absorption onset is then used to calculate $E_{HOMO-LUMO}$. M1 demonstrates the largest gap, while M5 shows the smallest energy difference between HOMO/LUMO. Some molecules, such as M5 demonstrate multiple photon absorption peaks; the lower energy absorptions were used to calculate the energy gap of the molecule. The gap calculated from solution UV-VIS agrees well with the thin film UV-VIS absorption and solution cyclic voltammetry gap results.

The UV-VIS absorption spectra are labeled by the same color scheme established in Figure 2.5. $E_{HOMO-LUMO}$ is calculated from the onset of the absorption of each molecule, and is recorded in Table 2.1. M1 exhibits the largest absorption onset energy and thus has the largest $E_{HOMO-LUMO}$ gap, and is evidence of a low lying HOMO energy. M2-M4 exhibit similar absorption onset energies and have similar $E_{HOMO-LUMO}$, being smaller than M1 and larger than M5. M5 exhibits the smallest absorption onset energy and thus has the smallest $E_{HOMO-LUMO}$ gap, which is evidence of a low lying LUMO energy. Molecules made with the core of M1 and M5

take advantage of these HOMO/LUMO offsets to synthesize narrow band-gap donor-acceptor molecules, which inspired many of the molecules in Figure 2.5.

## 2.7 Experimental Thermoelectric Properties of Highly Aligned Molecules

The electrical conductance of M1, M4 and M5 were measured by the procedure described in the experimental methods section, with the linear conductance histogram for M1 shown in Figure 2.9. The electrical conductances of M2 and M3 have been measured in the literature, and their values are provided in Table 2.1. The conductance of M2-M5 are all approximately in the same order of magnitude of $10^{-2}G_0$, which is typical for one ring aromatic molecules. Figure 2.9 is the linear electrical conductance histogram of M1, which demonstrates a high conductance of $0.18G_0$, which we attribute to a small $E_{HOMO}^{F}$ and better energy level alignment. The $1G_0$ peak of gold is much broader than previous measurements, and the higher order peaks of gold ($2G_0$, $3G_0$) are suppressed. We would like to note that upon preparation of these molecules on gold/mica, a strong crystallization of the film is observed before rinsing in solvent for SAM preparation, which may have a strong effect on the STM measurement. This results in a measurement of M1 that is more than an order of magnitude higher than typical aromatic ring molecules, and can be due to surface concentration effects resulting in crystallization, or oxidation of the molecule.[197]

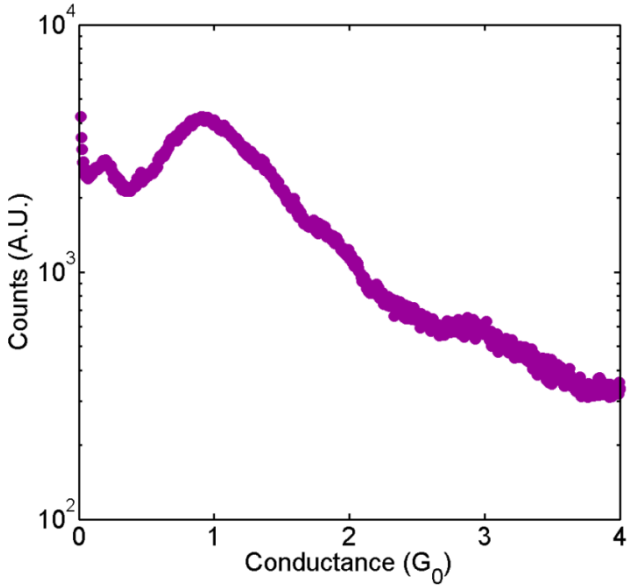


**Figure 2.9**: Electrical conductance histogram of molecule M1 (purple), where $G_{mol} = 0.18G_0$ and $G_{Au} = 0.98G_0$. The breadth of the gold peak is much larger than normal in other experiments. Molecule M1 crystallizes strongly when drop-cast on gold/mica, which may lead to unintended broadening of the $1G_0$ due to tip damage. Other explanations for the high conductance include surface concentration and concentration changing the energy levels of the molecular junction, or

oxidation of the molecule, as the solution is observed to change color over the course of the experiment. M1 is very keen to oxidize since the HOMO level was designed to be so high.

Since the electrical conductance of M1 is higher than M2-M5 due to energy level alignment, we expect to see an increase in the Seebeck coefficient and hence a improved power factor.[140] The values of the Seebeck coefficients are given in Table 2.1. Figure 2.10 depicts the thermoelectric voltage of M1, M4 and M5 and the internal gold reference standard as a function of applied temperature bias in the single molecule break junction. We observe that the Seebeck coefficient of M1 is positive, which we attribute to $E_{HOMO}^{F} < E_{LUMO}^{F}$ resulting in transport through the HOMO level, and that M4, M5 have a negative Seebeck coefficient, due to $E_{HOMO}^{F} > E_{LUMO}^{F}$ resulting in transport through the LUMO level. In the measurement, gold is also measured during the experiment, giving an internal reference of a gold junction (S = 0.93 μV/K). Since the values given for the thermoelectric measurement of M2 and M3 were of $S_{junc}$, a simple subtraction of the gold wire used will result in $S_{mol}$.

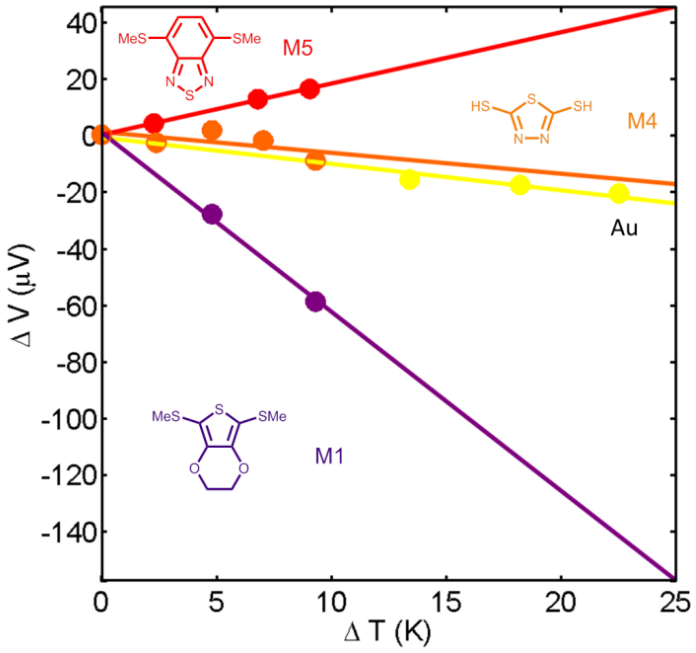


**Figure 2.10**: Seebeck coefficients of junctions formed with gold (yellow) and molecules M1 (purple), M4 (orange), M5 (red). M1 junctions show strong p-type behavior (HOMO transport) due to small $E_{HOMO}^{F}$. Junctions formed with M2 show weak n-type behavior, almost having a Seebeck coefficient of zero, which demonstrates both HOMO/LUMO transport. Molecule M5 is measured to have a negative Seebeck coefficient, indicative of LUMO transport and a LUMO energy close to that of the gold Fermi energy ($E_{HOMO}^{F} > E_{LUMO}^{F}$).

The trend in Seebeck coefficient, conductance and power factor is strongly dependent on $E_{HOMO}^{F}$ and $E_{LUMO}^{F}$; by decreasing $E_{HOMO}^{F}$ through molecule design so that the HOMO level is

more energy aligned, the S, G and the thermoelectric power factor are increased. N-type molecular junctions can be achieved by designing molecules that are extremely electron poor, which will result in $E_{LUMO}^{F} < E_{HOMO}^{F}$ and thus n-type transport. It is important to note that while the conductance of M1 is much higher than all other molecules in the series, the Seebeck coefficient does not appear to be substantially higher than M2. Typically, an energy aligned molecule would observe increases in both S and G. This lends credence to the theory that molecule M1 is extensively oxidized throughout the experiment, which will require future theorectical analysis on the effect of oxidation on molecular junctions. Now with the parameters S, G, $E_{HOMO-LUMO}$, $E_{HOMO}^{F}$, and $E_{LUMO}^{F}$, we have additional experimental parameters to aid the future theoretical evaluation using DFT+Σ or tight binding model.

| | $E_{HOMO}^{F}$ (eV) | $E_{HOMO-LUMO}$ (eV) | $E_{LUMO}^{F}$(eV) | $S_{junc}$ (μV/K) | $S_{mol}$ (μV/K) | G ($G_0$) | $S_{mol}^{2}G$ ($10^{-12}$ $W/K^2$) |
|---|---|---|---|---|---|---|---|
| M1 | 0.54 | 3.8 | 3.26 | 6.33 | 5.40 | 0.18 | 5.59e-4 |
| M2 | 1.52 | 3.10 | 1.58 | 6.83* | 5.03 | 0.0075* | 2.71e-5 |
| M3 | 1.55 | 3.15 | 1.6 | 4.8* | 3.86 | 0.011* | 1.79e-5 |
| M4 | 1.70 | 3.22 | 1.52 | 0.7 | -0.23 | 0.017 | 6.46e-7 |
| M5 | 1.84 | 2.48 | 0.64 | -1.78 | -2.71 | 0.007 | 1.72e-6 |
| Gold | - | - | - | 0.934 | - | 1 | 6.76e-5 |

Table 2.1: Values of $E_{HOMO}^{F}$, $E_{HOMO-LUMO}$, $E_{LUMO}^{F}$, $S_{junc}$, $S_{mol}$, G and $S_{mol}^{2}G$ for molecules M1-M5 from experimental data. *From gold wire subtraction of 1.6 uV/K for $S_{junc}$

Custom designed heterocycles with diverse substitutions and similar thiol-based binding groups were characterized using spectroscopic techniques, and the thermoelectric properties of their corresponding molecular junctions were measured. A combination of UPS and UV-VIS were used to measure the energy gap from the Fermi energy of the metal and the HOMO/LUMO energies of the molecule. The molecules that demonstrated a LUMO energy level closer to gold also showed n-type transport, and vice versa for the molecules designed with HOMO energy level alignment in mind. The molecule derived from EDOT showed the highest conductance during STM-BJ measurements and the highest Seebeck coefficient, but worries of oxidation could alter the molecular energy levels. Finally, experimental agreement with theoretical analysis on the shifts in $E_{HOMO}^{F}$, $E_{HOMO-LUMO}$, $E_{LUMO}^{F}$ during DFT+Σ calculations could lead to more accurate calculations.

## 2.8 Synthetic Methods

All glassware was oven-dried or flame-dried, and the reactions were conducted under Ar atomosphere using Schlenk line technique. THF, DMF and diethyl ether were obtained via the

solvent purification system packed with alumina. Unless specifically mentioned, all chemicals are commercially available and were used as received. Flash chromatography was performed using 60 Å silica gel (37-75 μm). $^{1}$H NMR spectra were recorded at either 500 MHz or 600 MHz, and $^{13}$C NMR spectra were recorded at 100 MHz or 126 MHz in $CDCl_3$. Chemical shifts are reported in ppm referenced to residual solvent peak as follows: 7.24 ppm for $^{1}$H NMR; 77.16 ppm for $^{13}$C NMR.

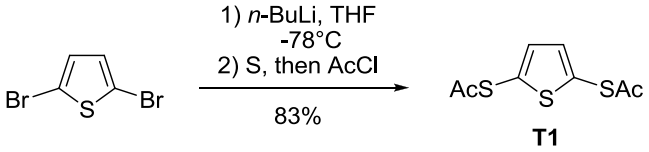


**Scheme 2.1:** S,S'-Thiophene-2,5-diyl diethanethioate (T1):

2,5-Dibromothiophene (1.98 g, 8.18 mmol, 1.0 equiv) was dissolved in dry $Et_2O$ (40 mL), and the solution was cooled to -78 °C. *n*-BuLi (2.5 M in hexanes, 7.20 mL, 18.0 mmol, 2.2 equiv) was added dropwise via syringe, and the reaction was allowed to stir at -78 °C for 30 min. Dry sulfur (786 mg, 24.5 mmol, 3.0 equiv) power was added in one portion, and the reaction was stirred for another hour before AcCl (1.45 mL, 20.4 mmol, 2.5 equiv) was added via syringe. The cold bath was removed, and the reaction was stirred for an additional one hour, before pouring into water (50 mL). The aqueous layer was extracted with $Et_2O$ (30 mL×2), and the combined organic layers were washed with brine (10 mL), dried over $MgSO_4$, filtered, and concentrated to provide a gray oil. Purification by flash chromatography with a gradient of 1:1 hexane:$CH_2Cl_2$ to $CH_2Cl_2$ provided T1 as a colorless oil (1.58 g, 83%). $^{1}$H NMR (500 MHz, $CDCl_3$) δ 7.10 (s, 2H), 2.39 (s, 6H). $^{13}$C NMR (126 MHz, $CDCl_3$) δ 193.00, 135.42, 131.17, 29.73. GC-MS: *m/z* = 232.

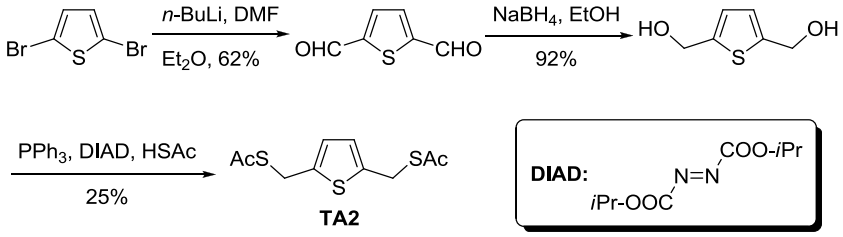


**Scheme 2.2:** *S,S'*-Thiophene-2,5-diylbis(methylene) diethanethioate (TA2)

2,5-Dibromothiophene was converted to 2,5-diformylthiophene via lithium-halogen exchange followed by trapping with DMF,[198] and subsequently to thiophene-2,5-diyldimethanol via reduction with $NaBH_4$ following the known procedures.[199] TA2 was obtained via Mitsunobu reaction shown as follows.

Diisopropyl azodicarboxylate (DIAD, 1.06 mL, 3.38 mmol, 1.0 equiv) was added dropwise via syringe to a dry THF (10 mL) solution of $PPh_3$ (1.41 g, 5.38 mmol, 2.5 equiv) in an ice bath. Thiophene-2,5-diyldimethanol (310 mg, 2.15 mmol, 1.0 equiv) was dissolved in dry THF (12 mL), and added slowly via syringe to the above solution, followed by the addition of AcSH (380 μL, 5.38 mmol, 2.5 equiv). The reaction was allowed to warm up to room temperature slowly and stir overnight (24 hrs), and then heated to 70 °C for 2 hrs. After cooling down to room temperature, the reaction mixture was concentrated, and purified by flash chromatography (1:1 hexane:$CH_2Cl_2$) to provide TA2 as a colorless oil (141 mg, 25%). $^1$H NMR (500 MHz, $CDCl_3$) δ 6.72 (s, 2H), 4.21 (s, 4H), 2.32 (s, 6H). $^{13}$C NMR (126 MHz, $CDCl_3$) δ 194.72, 140.09, 126.47, 30.43, 28.28. GC-MS: *m/z* = 260.

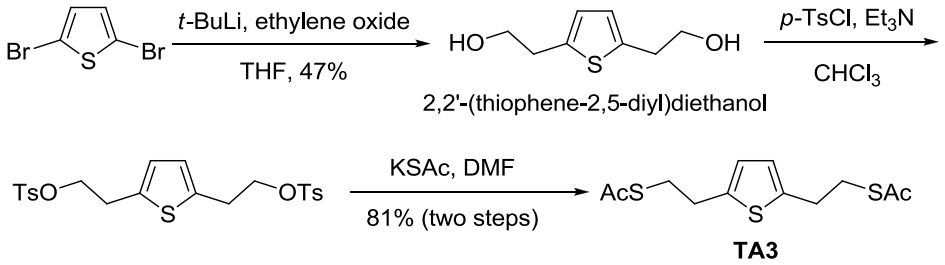


**Scheme 2.3:** *S,S'*-Thiophene-2,5-diylbis(methylene) diethanethioate (TA3)

2,5-Dibromothiophene (1.84 g, 7.61 mmol, 1.0 equiv) was dissolved in dry THF (38 mL), and the solution was cooled to -78 °C in a dry ice/acetone bath. *t*-BuLi (9.84 mL of 1.7 M in pentane, 16.7 mmol, 2.2 equiv) was added dropwise via syringe. The reaction was stirred at -78 °C for 30 min, and at 0 °C for 1 h, before cold ethylene peroxide (1.9 mL, 38.0 mmol, 5.0 equiv) was added via syringe quickly. The reaction was allowed to warm up to room temperature and stir overnight (15 hrs), and quenched with saturated $NH_4Cl$ (aq, 20 mL). The aqueous layer was extracted with $CHCl_3$ (20 mL×3). The combined organic layers were dried ($MgSO_4$), filtered, and concentrated to provide a brown oil. Purification by flash chromatography (1:1 hexane:EtOAc) provides 2,2'-(thiophene-2,5-diyl)diethanol as a colorless oil (616 mg, 47%). $^1$H NMR (500 MHz, $CDCl_3$) δ 6.65 (s, 2H), 3.75 (t, *J* = 6.3 Hz, 4H), 2.94 (t, *J* = 6.3 Hz, 4H), 2.47 (s, 2H). $^{13}$C NMR (126 MHz, $CDCl_3$) δ 139.62, 125.44, 63.38, 33.52. GC-MS: *m/z* = 172.

2,2'-(Thiophene-2,5-diyl)diethanol (198 mg, 1.15 mmol, 1.0 equiv) was dissolved in $CHCl_3$ (5 mL), and $Et_3N$, *p*-TsCl in $CHCl_3$ (3 mL), and catalytic amount of DMAP (5%) were added. After stirring at room temperature overnight (24 hrs), the reaction was diluted with $H_2O$ (20 mL), and the aqueous layer was extracted with $CHCl_3$ (20 mL×2). The combined organic layers were dried ($MgSO_4$), filtered, and concentrated to provide 2,2'-(thiophene-2,5-diyl)bis(ethane-2,1-diyl)bis(4-methylbenzenesulfonate) as a brown oil, which was used without further purification.

The analytical sample as a colorless oil was purified by flash chromatography (3:1 hexanes:EtOAc). $^{1}$H NMR (600 MHz, $CDCl_3$) δ 7.72 (d, *J* = 8.1 Hz, 4H), 7.30 (d, *J* = 8.1 Hz, 4H), 6.56 (s, 2H), 4.14 (t, *J* = 6.8 Hz, 4H), 3.04 (t, *J* = 6.8 Hz, 4H), 2.42 (s, 6H). $^{13}$C NMR (151 MHz, $CDCl_3$) δ 144.99, 137.25, 132.92, 129.96, 127.96, 126.05, 70.04, 29.78, 21.74. MS (ESI) *m/z* calcd for $C_{22}H_{24}O_6S_3Na^+$: 503.1; found: 503.1.

The crude product and KSAc (657 mg, 5.75 mmol, 5.0 equiv) were combined in a 25 mL round bottom flask, dry DMF (12 mL) was added, and the suspension was stirred at 80 °C for 3 h. The reaction was diluted with $H_2O$ (50 mL) and $Et_2O$ (50 mL), and the aqueous layer was extracted with $Et_2O$ (50 mL×2). The combined organic layers were washed with $H_2O$ (30 mL×4), brine (20 mL), dried ($MgSO_4$), filtered, and concentrated to provide a yellow crystalline solid. Purification by flash chromatography (1:1 hexanes:$CHCl_3$, then $CHCl_3$) provided TA3 as a colorless crystalline solid (268 mg, 81% over two steps). $^{1}$H NMR (500 MHz, $CDCl_3$) δ 6.61 (s, 2H), 3.08 (t, J = 7.4 Hz, 4H), 2.97 (t, J = 7.1 Hz, 4H), 2.29 (s, 6H). $^{13}$C NMR (126 MHz, $CDCl_3$) δ 195.37, 140.93, 124.87, 30.66, 30.64, 30.21. MS (EI): *m/z* = 288.03.

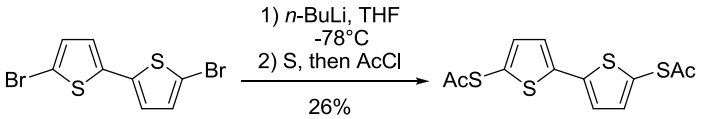


**OT2**

**Scheme 2.4:** *S*,*S*'-([2,2'-bithiophene]-5,5'-diyl)diethanethioate (OT2)

2,5-Dibromothiophene (405 mg, 1.25 mmol, 1.0 equiv) was dissolved in dry THF (25 mL), and the solution was cooled to -78 °C. n-BuLi (2.5 M in hexanes, 1.25 mL, 3.125 mmol, 2.5 equiv) was added dropwise via syringe, and the reaction was allowed to stir at -78 °C for 30 min, and 0 °C for 1 h. Dry sulfur (120 mg, 3.75 mmol, 3.0 equiv) power was added in one portion, and the reaction was stirred at 0 °C for another hour, before AcCl (267 μL, 3.75 mmol, 3.0 equiv) was added via syringe. The reaction was allowed to warm up to RT, and stirred overnight (15 hrs), before pouring into water (50 mL). The aqueous layer was extracted with Et2O (30 mL×2), and the combined organic layers were washed with brine (10 mL), dried over $MgSO_4$, filtered, and concentrated to provide a brown oil. Purification by flash chromatography with a gradient of 1:1 hexane:$CHCl_3$ to $CHCl_3$ provided OT2 as a yellowish solid (102 mg, 26%). $^{1}$H NMR (500 MHz, $CDCl_3$) δ 7.14 (d, *J* = 3.8 Hz, 2H), 7.04 (d, *J* = 3.8 Hz, 2H), 2.41 (s, 6H). $^{13}$C NMR (126 MHz, $CDCl_3$) δ 194.00, 142.72, 136.66, 125.13, 125.05, 29.83.

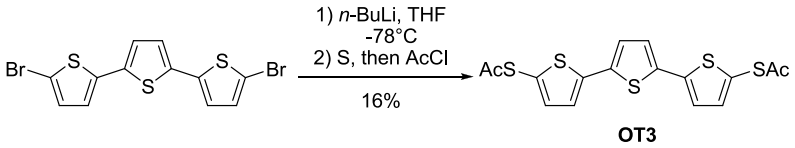


**Scheme 2.5:** *S*,*S*′-([2,2:5′,2″-terthiophene]-5,5″-diyl) diethanethioate (OT3)

OT3 was synthesized under similar conditions as OT2,[178] and purified by flash chromatography with 3:2 hexane:$CH_2Cl_2$ to provide a yellowish solid (yield = 16%). $^1$H NMR (600 MHz, $CDCl_3$) δ 7.12 (d, *J* = 3.7 Hz, 2H), 7.06 (s, 2H), 7.04 (d, *J* = 3.8 Hz, 2H), 2.41 (s, 6H). $^{13}$C NMR (151 MHz, $CDCl_3$) δ 194.10, 143.10, 136.70, 136.26, 125.34, 124.42, 124.37, 29.75.

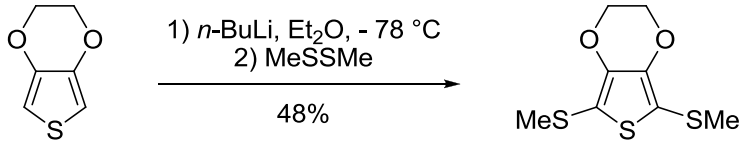


**Scheme 2.6:** 5,7-bis(methylthio)-2,3-dihydrothieno[3,4-b][1,4]dioxine (M1)

3,4-Ethylenedioxythiophene (EDOT, 1.068 mL, 10 mmol, 1.0 equiv) was dissolved in dry $Et_2O$ (100 mL) under Ar, and the solution was cooled to -78 °C in a dry ice/acetone bath. *n*-BuLi (2.5 M in hexane, 8.8 mL, 22 mmol, 2.2 equiv) was added slowly via syringe. The reaction mixture was stirred at -78 °C for 1 h and at room temperature for 3 h. A lot of white solid was observed. The reaction mixture was cooled in an ice bath, and MeSSMe (2.67 mL, 30 mmol, 3.0 equiv) was added via syringe. The reaction mixture was allowed to warm up to room temperature and stirred overnight (15 hrs), followed by quenching with addition of water (50 mL) in an ice bath. The aqueous layer was extracted with $Et_2O$ (50 mL × 3), and the combined organic layers were washed with brine (20 mL), dried over $Na_2SO_4$, filtered, and concentrated to provide a white solid. Purification by flash chromatography with hexanes: EtOAc (20:1, $R_f$ = 0.15) provide the title product as a white solid (1.12 g, 48%). $^1$H NMR (600 MHz, $CDCl_3$) δ 4.25 (s, 4H), 2.36 (s, 6H). $^{13}$C NMR (151 MHz, $CDCl_3$) δ 142.7, 110.7, 64.8, 21.1. GC-MS: 228.

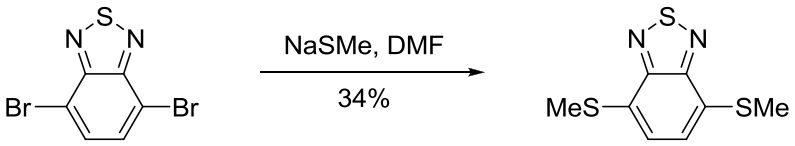


**Scheme 2.7:** 4,7-bis(methylthio)benzo[c][1,2,5]thiadiazole (M5)

4,7-Dibromo-2,1,3-benzothiadiazole (240 mg, 0.82 mmol, 1.0 equiv) and NaSMe (126 mg, 1.8 equiv, 2.2 equiv) were added in a sealable microwave tube, and dry DMF (4 mL) was added to yield a brown solution. The reaction was sealed under Ar, and stirred at 90 °C in an oil bath for 24 h. The reaction was diluted with EtOAc (100 mL), washed with water (20 mL× 3) and brine (10 mL), dried over $Na_2SO_4$, filtered, and concentrated to provide a yellow solid. Purification by flash chromatography with 10:1 pentane:$CH_2Cl_2$ (10:1, $R_f$ = 0.1) provide the title product as a yellow solid (64 mg, 34%). $^1$H NMR (600 MHz, $CD_2Cl_2$) δ 7.21 (s, 2H), 2.61 (s, 6H). $^{13}$C NMR (151 MHz, $CD_2Cl_2$) δ 153.3, 129.0, 124.2, 15.1. GC-MS: 234.

## 2.9 Measurement Methods

All absorption measurements were performed using a Perkin Elmer Lambda 750 spectrophotometer or Agilent Cary 60 at room temperature. All solution experiments were run in THF or $CH_2Cl_2$ in a quartz cuvette (1 cm length). Ultraviolet photoelectron spectroscopy was run on the Kratos Axis Ultra system under high vacuum conditions on the same gold-mica substrates used for STM-BJ measurements.

For STM-BJ measurements, five μL of a 0.05M tetrahydrofuran solution with the desired molecule at concentration of 10 mg/ml was drop cast by micropipette onto gold films. The gold films were thermally evaporated onto a freshly cleaved mica substrate to enable an atomically smooth surface. A modified STM break junction with an Au tip is then crashed into the gold substrate and withdrawn, with current and voltage measurements being acquired throughout the process. Both the STM Au tips and the Au thin films on mica were hydrogen flame annealed to ensure the removal of containments.

The measurement of the molecular conductance requires a bias of 5 mV to be applied between tip and substrate on approach. The STM gold tip is driven to the gold substrate with a rate of 1 nm/s until a conductance threshold of $1G_0$ is reached. The tip is then withdrawn at a rate of 0.5 nm/s, with a gold-gold junction first forming, followed by a junction with the molecule of interest. No voltage bias is applied upon the withdrawal process. This process is repeated until five thousand junction traces are acquired. These results are then analyzed by histogram statistics and the resulting histogram peaks gives the molecular conductance, with the full width half max of the peak being the error bar.

The measurement of the Seebeck coefficient required a temperature gradient across the substrate and tip. The substrate was heated via a specially constructed STM cell and Peltier heater, and the STM tip was connected to a thermal sink to ensure a constant temperature of 20°C. The power output to the Peltier heater was varied to control the temperature of the substrate. The gold STM tip is driven into the gold substrate until a conductance of $5G_0$ is measured. The tip-substrate voltage bias is then removed via a solid state relay, and this cycle is

repeated until two thousand junctions are acquired. Each trace is binned into a histogram. The peak voltage is the thermoelectric voltage at that temperature, and the FWHM the error bar. The Seebeck coefficient is calculated via a least-square linear fit of the measured molecule, with the temperature drop as the independent variable, the peak voltage as the dependent variable and the FWHM approximating the error in the measurement. Per convention, the Seebeck coefficient is the negative of the resulting slope. A subtraction of the Seebeck coefficient of the instrument (1.6 μV/K) is then performed.

## 2.10 Theoretical Methods

To calculate the conductance and Seebeck coefficient from the H, the Green's function, G, is constructed

$$G^r = (\varepsilon - H)^{-1} \tag{2.1}$$

which, along with the coupling, is used to calculated the transmission via the standard expression

$$T = Tr[\Gamma G^r \Gamma G^a] \tag{2.2}$$

where $G^r$ is the retarded Green's function and $G^a$ is the advanced Green's function. The transmission is related to the conductance and thermopower through the following relations:

$$G = G_0 T(E_F) \tag{2.3}$$

$$S = -\frac{\pi^2 k_B^2 T}{3e^2} \frac{d}{dE} \ln T(E = E_F) \tag{2.4}$$

where $G_0$ is the quantum of conductance.

In order to fit the parameters in the model, the experimental data was fit either to a linear or exponential trend. When fitting the experimental data the thermopower of the OT series was fit to a line with a positive slope and intercept: $S=S_{1C}+\beta_{1S}L$, the thermopower of the TA series was fit to a line with a negative slope and positive intercept: $S = S_{2C} - \beta_{2S}L$, and the conductance of the TA series was fit to a decaying exponential $G=G_{2C}\exp(-\beta_{2C}L)$. For each series the difference between the experimental fit and the value from the model was simultaneously minimized for all the data available with respect to the parameters in the model. The parameters in the model for the OT series were $\Gamma$, $E_s$, $E_b$, $\delta$, and $\tau$. The parameters for the model of the TA series use the parameters from the OT series but allow the coupling between the gateway state and the backbone as well as the position of the gateway energy to vary for each parameter; therefore, we minimize with respect to $E_s$ and $\tau$ for each TA2 and TA3 independently and keep $\Gamma$,and $E_b$ fixed.

## 2.11 Acknowledgements

We gratefully acknowledge support from the Air Force Office of Science Research (No. MURI FA9550-12-1-0002). Theoretical calculations were performed by Michele Kotiuga at the Molecular Foundry, a Lawrence Berkeley National Laboratory user facilities supported by the Office of Science, Office of Basic Energy Sciences, U.S. Department of Energy, under Contract No. DE-AC02-05CH11231. Synthesis was developed by Dr. Cheng-kang Mai at UC Santa Barbara.

# Chapter 3: Gold Nanocrystal Arrays as Platform for Scaled Molecular Thermoelectrics

Adapted from W. Chang, B. Russ, V. Ho, J. Urban, R. Segalman. Gold Nanocrystal Arrays as a Platform for Molecular Thermoelectrics. *Physical Chemistry Chemical Physics*, **17**, 6207-6211 **(2015)**. Reproduced by permission of The Royal Society of Chemistry

## 3.1 Gold Nanocrystals as Thermoelectrics

Efficiencies of bulk thermoelectric systems have been limited because the Seebeck coefficient and electrical conductivity are typically inversely correlated in traditional materials. Decoupling of these properties has been demonstrated in molecular junctions by capitalizing on the unique electronic transport at organic-inorganic interfaces. In this chapter, the thermoelectric properties of gold nanocrystal arrays with varying thiol-terminated ligands are compared to molecular junction experiments. Next, the thermal conductivity of these exchanged gold nanocrystal arrays are investigated, and the thermal conductivity is observed to decrease with length, and follows theoretical trends well. The degree of exchange in the nanocrystal arrays is examined by thermoelectric AFM and conductive AFM. With this foundation, we then will explore the effect of binding groups on the thermoelectric performance of the nanocrystal arrays, and we see that depending on the character of the ligand, either p or n-type thermoelectric behavior can be observed. An explanation for the switch in electron to hole transport is based on Landauer transport and the spectrochemical ligand series. The experimental results and supporting theory demonstrate that gold nanocrystal arrays are a valuable model system for mapping the applicability of molecular junction design to macroscopic organic-inorganic hybrid thermoelectric materials.

Thermoelectrics are a promising avenue for waste heat conversion to usable electrical energy. The efficiency of thermoelectrics is related to the thermoelectric figure of merit, ZT, and is described by the following Equation 3.1:

$$ZT = \frac{S^2\sigma}{\kappa}T \tag{3.1}$$

where the Seebeck coefficient, S, and the electrical conductivity, σ, define the power factor, $S^2\sigma$, and, κ is the thermal conductivity. In most materials, the Seebeck coefficient and the electrical conductivity are inversely correlated, limiting the power factor. To achieve greater efficiencies in thermoelectrics, these material properties must be individually controlled and decoupled. Single molecule studies have shown promise in changing the relationship between the Seebeck coefficient, S, and electrical conductance, G, (the single molecule equivalent of the electrical

conductivity) with experiments demonstrating simultaneous increases in S and G.[171] While an ideal model system for studying thermoelectrics on a fundamental level, single molecule junctions must be scaled to multi-dimensional architectures to fulfil the promise of being active components in devices and applications.[200] Nanocrystal arrays (NCAs) have already proven to be useful platforms for investigating macroscale molecular junction-induced thermal[201-202] and optoelectronic material properties.[203,69,204] We demonstrate in this chapter that NCAs are also attractive model systems for studying the scalability of molecular junction thermoelectric design principles.

We selected gold nanoparticles with organic surface ligands for fabricating our macroscale model of molecular junction arrays. Arrays of gold nanoparticles were an ideal material choice, providing a direct multi-dimensional system parallel to gold scanning tunnelling microscope (STM)-break junction tips.[205,206] Advances in ligand exchange strategies on the nanoparticle surface[203] enable an avenue to controllably tailor the molecular junctions throughout a NCA.[61,207] From the single molecule literature, a series of alkanethiols, alkanedithiols and oligophenyldithiols were chosen with varying molecular junction lengths. The thermoelectric properties of single molecule junctions with these ligands have been theoretically and experimentally determined, providing a robust reference for comparison to the NCA studies.[160,208,209] In our study, the thiol binding group was held constant to eliminate variables such as binding geometry and strength of electrode coupling, which can both significantly influence transport.[210]

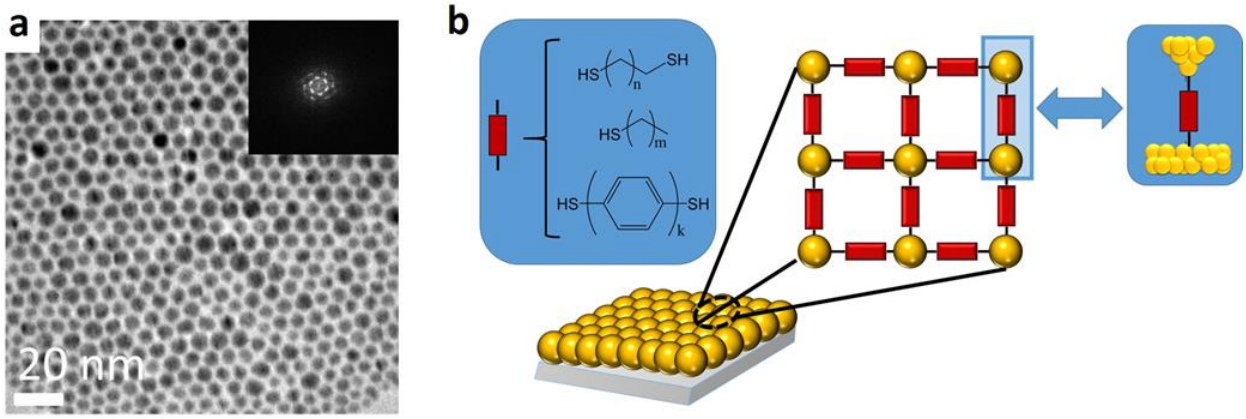


**Figure 3.1:** (a) Transmission electron microscopy of drop-casted gold nanocrystal arrays with oleylamine ligands, with a scale bar of 20 nm. Inset: the Fourier transform of this image shows the well-ordered nature of the thin film with oleylamine ligands ($R_{mean}$ = 3 nm, $\sigma_R$ = 1.5 nm). (b) Schematic of gold nanocrystal arrays used as a model system for mapping the applicability of molecular junction design rules to the design of macroscale organic-inorganic hybrid thermoelectric materials. Three classes of thiol-terminated ligands were used in these studies for

comparison to previously reported single molecule experiments: alkanedithiols (n=1,2,3,5,7), alkanethiols (m=1,2,3,4), and oligophenyldithiols (k=1,2,3). A single Au-ligand-Au element is highlighted to emphasize its similarity to the gold STM-break junction tips in single molecule experiments.

## 3.2 Experimental NCA Thermoelectric Results

Our experiments show that electron tunnelling from gold nanoparticle to nanoparticle follows an exponential decay with inter-particle separation distance, and electrical conductance can be correlated to the length of single molecule junctions in the framework of the electron tunnelling model.[211] In single molecular experiments, electrical conductance is facilitated by transmission through a molecular orbital in the junction. These molecular orbitals are hypothesized to be metal induced gap states (MIGS). In this transport regime, the Landauer transmission function dictates electron transport,[155] and the magnitude of resistance increases exponentially with length, as seen in Equation 2:

$$R = R_A e^{\beta L} \tag{3.2}$$

where R is the electrical resistance, the inverse of conductance, $R_A$ is the extrapolated resistance at zero length, β is the electronic decay parameter, and L is the ligand or molecular junction length.

The ligand length dependence of electrical conductance in the exchanged gold nanocrystal arrays displays a prominent similarity to trends observed for single molecule junctions.[74] Figure 3.2 shows how the electrical resistivity changes exponentially with increasing ligand lengths in these NCAs. The yellow diamond is the resistivity of a thermally evaporated 100nm thick gold film, which serves as the control for intrinsic conductivity of gold. The red triangles refer to monothiol ligands binding with a gold adatom (with increasing length: ammonium thiocyanate, ethanethiol, propanethiol, butanethiol and pentanethiol, $\beta = 2.3$ Å$^{-1}$). The blue squares are alkanedithiol ligands (with increasing length: ethanedithiol, propanedithiol, butanedithiol, hexanedithiol, octanedithiol, $\beta = 0.95$ Å$^{-1}$). The black circles represent oligophenyldithiol ligands (benzenedithiol, biphenyldithiol, terphenyldithiol, $\beta = 0.05$ Å$^{-1}$). Ligand lengths were calculated using Spartan'14, and a table is provided in the SI T1.

Notably, each class of ligand exhibits an exponential increase in the electrical resistivity with increasing ligand length, but the magnitude of the β decay parameter depends strongly on molecular conjugation and whether the ligand is monothiol or dithiol. Alkanedithiol NCAs has a β decay parameter of 0.95 Å$^{-1}$, which is similar to the value seen for single molecule alkanedithiol junctions, where a β decay parameter of 0.88 Å$^{-1}$ is reported.[212] Oligophenyldithiols in the single molecule literature typically exhibit smaller β decays than alkanedithiols, due to the presence of conjugation along the molecular backbone. This trend is also observed in NCAs with

oligophenyldithiols, with a β decay parameter of 0.05 $Å^{-1}$. In the single molecule literature, oligophenyldithiols have been observed to have a β decay parameter of 0.26 $Å^{-1}$.[62] The overall trends between classes of organic molecular ligands hold in the nanocrystal arrays. Given the macroscopic nature of the transport in gold nanocrystal arrays, it is reasonable to expect some deviation in absolute β decay values from the single molecule measurements.

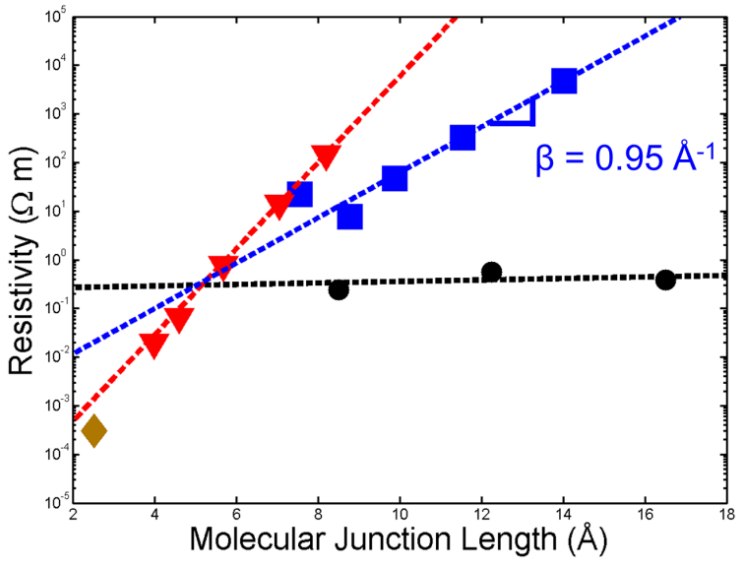


**Figure 3.2:** Electrical resistivity of gold nanocrystal arrays as a function of ligand length is shown. β decay parameters for alkanethiols (red triangles), alkanedithiols (blue squares) and oligophenyldithiols (black circles) are 2.3 $Å^{-1}$, 0.95 $Å^{-1}$, 0.05 $Å^{-1}$ respectively. A 100 nm gold thin film resistivity is the yellow diamond. Conjugation along the molecular backbone in oligophenyldithiols results in a lower decay parameter than in alkanedithiols. Error bars are on the scale of the data points.

While an increase in the electrical resistance with increasing ligand length was anticipated, it was surprising to observe that the Seebeck coefficient of these gold nanocrystal arrays switches from positive to negative in alkanethiols (Figure 3.2). A positive Seebeck coefficient indicates p-type (hole) transport, while a negative Seebeck coefficient demonstrates n-type (electron) transport. The colour scheme and naming in Figure 3.3 corresponds identically to that of Figure 3.2, with the exception of the absence of octanedithiol, which has a Seebeck coefficient so low that it was indistinguishable from the noise floor. With increasing alkane ligand length, a switch from p-type behaviour to n-type behaviour is observed at approximately 6 Ångstroms in alkanethiol NCAs.

Alkanedithiol NCAs show n-type transport, and a Seebeck coefficient that decreases in magnitude with ligand length. The relationship between the Seebeck coefficient and alkanedithiol length is 0.51 μV/(K Å). In contrast, the Seebeck coefficient of alkanedithiols in single molecule measurements is reported to be positive, indicating p-type transport, and the

change in Seebeck coefficient as a function of length has been observed to be -0.74 μV/(K Å).[161] In both single molecule junctions and NCAs, increasing alkanedithiol length results in a decreased Seebeck coefficient, albeit with different carrier type.

Oligophenyldithiols (black, Figure 3.3 inset) show a much larger Seebeck coefficient than alkanedithiols, with Seebeck coefficients of 40 μV/K. In the single molecule literature, oligophenyldithiols consistently show Seebeck coefficients that increase with molecule length, and have values much higher than alkanedithiols.[161] However, in the NCA film measurements, there is no discernible trend with oligophenyldithiols length versus Seebeck coefficient, which shows a peak value with biphenyldithiol. The large size and steric stiffness of terphenyldithiols, as compared to alkanedithiols, potentially introduce film defects during ligand exchange, which could explain the absence of a ligand size dependence of the Seebeck coefficient.

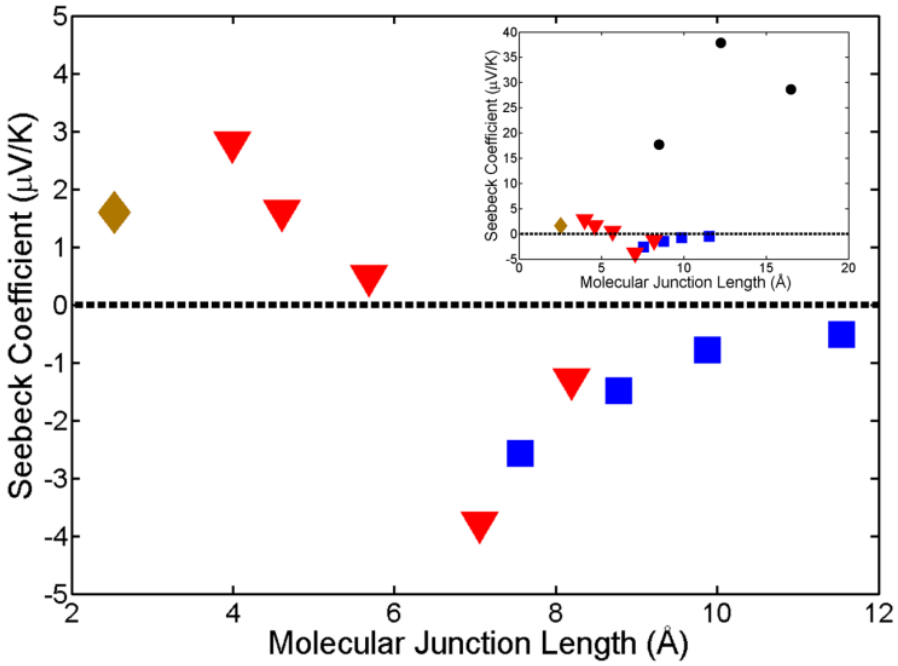


**Figure 3.3:** The Seebeck coefficient of gold nanocrystal arrays as a function of ligand length for alkanethiols (red triangles) and alkanedithiols (blue squares). As molecular junction length increases, a switch from hole transport to electron transport is observed at approximately 6 Ångstroms. The error bars are on the scale of the data point. (Inset) Oligophenyldithiols (black circles) show a much higher Seebeck coefficient than alkanedithiols (blue squares), as predicted from the single molecule literature.

## 3.3 Theoretical Modeling of Thermoelectric Transport

Several physical changes within the nanocrystal arrays are hypothesized to explain the origin of the n-type transport observed in the alkanedithiol system and the p-n type switch in alkanethiol NCAs. Small angle x-ray scattering experiments were performed to see if an order-disorder transition was present, since an ordered film could show different carrier transport than a disordered film.[213] However, the peak intensity decreases substantially upon ligand exchange, indicating that all films are disordered post-exchange, and thus this explanation cannot hold. An alternative explanation may be that there is a shift in the MIGS of the molecular junction responsible for transport. In single molecule junctions, the Seebeck coefficient is directly related to the slope of the logarithm of the Landauer transmission function, where the sign of the slope will dictate n-type or p-type behavior.[160] As alkanedithiol ligands grow longer, the transmission through metal induced gap states decreases in probability, resulting in decreasing Seebeck coefficient with length in alkanedithiols, as seen experimentally and theorectically.[214] Additionally, the observed shift from hole to electron transport in alkanethiols NCAs could be a result of a shifting in the energy level of these MIGS through a critical length scale. Thus, modulation in the MIG energy level could explain the Seebeck coefficient trends observed, and direct observation of these MIGS will be the subject of future experimental work.

To accurately compare the thermoelectric behaviour between single molecule junctions and nanocrystal array films, the theoretical power factor $S^2\sigma$ was calculated using the theory developed by Müller.[215] The power factor of a nanocrystal array was theoretically modelled based on the constituent molecular junction experimental thermoelectric properties. It can be shown that the Seebeck coefficient and electrical conductivity of the NCA is described by Equation 3.3 & 3.4:

$$S_{NCA} = S_{Junction} \tag{3.3}$$

$$\sigma_{NCA} = \frac{N_Y N_Z}{N_x L} M G_{Junction} \tag{3.4}$$

Where $N_{x,y,z}$ is the number of junctions in a given dimension, L is the nanoparticle diameter, M is the number of molecules bridging a junction, $G_{junction}$ is the electrical conductance of a single molecule junction, and $S_{junction}$ is the Seebeck coefficient of said junction. Given the sample geometry and knowledge of the nanoparticle size from TEM, and an approximation of the number of ligands participating in electron transmission at 1000, the theoretical power factor of a nanocrystal array based on molecular junction theory can be determined. This is shown in Figure 3.4, which directly compares the theoretical power factor of a gold NCA based on experimental single molecule experiments to experimental nanocrystal array power factors. The theoretical power factor predictions are well matched in both trend and value to those observed experimentally for alkanedithiols. In contrast, the predicted power factor of oligophenyldithiols is markedly lower than what is observed experimentally. This disparity is due to the conductivity of oligophenyldithiols being higher in NCAs than predicted from the single molecule literature, which may result from better energy level alignment at the gold nanoparticle/ligand interface

than in single molecule junctions. Multiple ligands binding to the same nanoparticle has been predicted to modulate the MIGS level, an effect not seen in molecular junctions consisting of only a single molecule.[215]

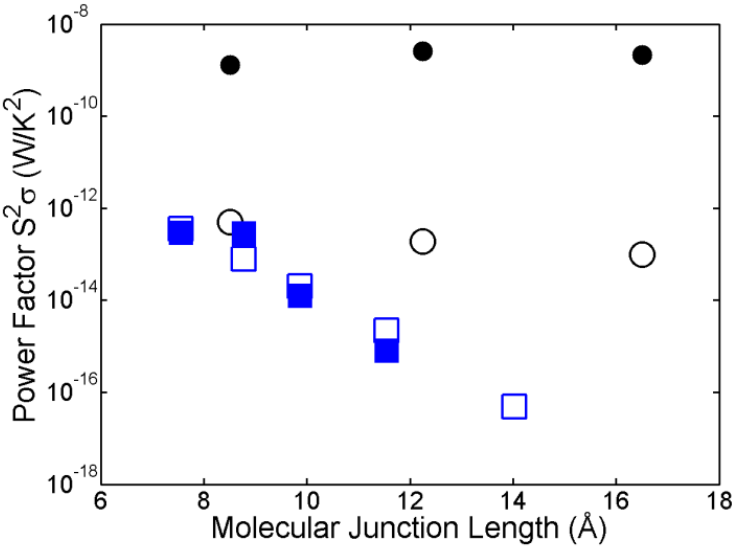


**Figure 3.4:** Comparison of the power factor $S^2\sigma$ in gold NCAs with alkanedithiol ligands (blue, filled squares) and oligophenyldithiols (black, filled circles) compared to theoretical NCAs based on STM/AFM break junction single molecule experiments (alkanedithiols in blue, open squares and oligophenyldithiols in black, open circles. The prediction from theory fits well to alkanedithiol experimental data with the parameters: L = 10 nm, $N_yN_z/N_x = 10^{-7}$ junctions, M = 1000 molecules.

## 3.4 Investigation of Metal Induced Gap States

To test the hypothesis that metal induced gap states are those responsible for the switch from hole transport to electron transport in alkanethiol nanocrystal arrays, ultraviolet photoelectron spectroscopy was performed on gold NCAs exchanged with ethanethiol, propanethiol, butanethiol and pentathiol. The UPS results near the Fermi edge are plotted in the Figure 3.5 below, where the data is not offset for clarity. Most importantly, what is observed that all materials demonstrate measureable intensity at zero binding energy, which suggests that the density of states at the Fermi energy is non-zero.[99,180–192] Additionally, from the observed trend, ethanethiol has the smallest density of states near the Fermi energy, followed by pentathiol. Butanethiol and propanethiol have similar density of states at the Fermi energy, which may correspond to the low Seebeck coefficient measured, as the slope of the density of states with relation to energy determines the magnitude of the Seebeck coefficient.[216,107,98,116] UPS can neither confirm nor deny the presence of metal induced gap states are the rationale behind the

observed p to n-type switch, as we are missing information about the LUMO level and transport through that orbital. Future inverse photoelectron spectroscopy may shed some light on this problem.

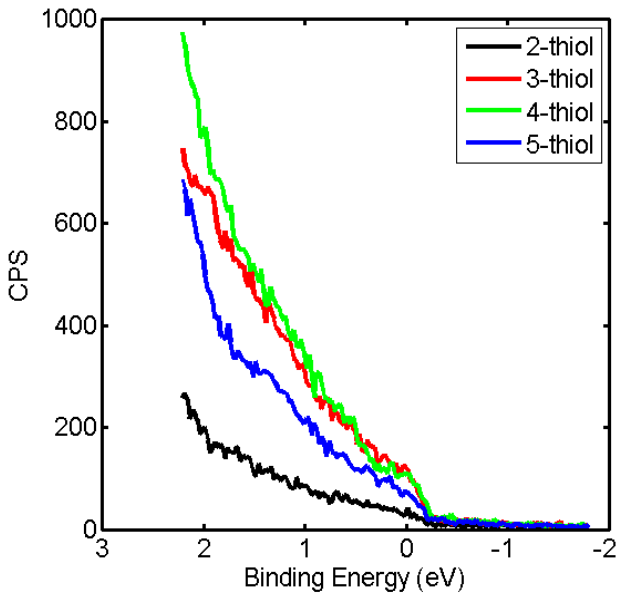


**Figure 3.5**: Ultraviolet photoelectron spectroscopy of gold nanocrystal arrays exchanged with the listed ligands. UPS determines the HOMO energy level of the molecules, along with information of the electronic density of states near the Fermi edge. This experiment was performed to ascertain the whether metal induced gap states (MIGS) were responsible for charge transport and change in carrier concentration; however, without information about LUMO transport, it is difficult to assign transport to either the HOMO or LUMO orbital.

## 3.5 Thermal Conductivity of Gold NCA

After experimentally measuring and understanding theoretically the role of scaled molecular junctions to the thermoelectric power factor of these gold nanocrystal arrays, the thermal conductivity was then assessed. While the power factor of these materials are not as large as state of the art thermoelectrics, fundamental understanding of the total thermoelectric characterization of these materials is important from a scientific, fundamental physics point of view.[197,57,217–220] In collaboration with the Dames group and particularly Geoff Wehmeyer, the thermal conductivity of these gold nanocrystal arrays with varying alkanethiol ligands. It was initially expected that the thermal conductivity of these materials would be very low due to their nanocrystalline nature, and this was indeed observed in Figure 3.6, where the thermal conductivity is close to the amorphous limit.[221–224,120,225]

The thermal conductivity was measured by the 3-ω technique, which is discussed briefly in the methods section. The ligands in the nanocrystal array are ammonium thiocyanate, along with alkanethiols such as ethanethiol, butanethiol, pentanethiol and heptanethiol. The electronic contribution to the thermal conductivity can be calculated using the Wiedemann-Franz relation in Equation 3.3, and as the films demonstrate electrical conductivity near 0.1 S/cm, the thermal conductivity is dominated by the phononic contribution.

$$\frac{\kappa}{\sigma} = LT,\ \mathrm{L} = 2.44\mathrm{e}^{-8}\ \mathrm{W}\ \Omega\ \mathrm{K}^{-2} \tag{3.3}$$

Therefore, the thermal conductivity of these materials is very low and near the amorphous limit, where the mean free path of phonons are very short, and is dominated by inter-particle coupling.[120,225] As the molecular ligands used increase in length, the inter-particle coupling decreases in strength, resulting in a lower thermal conductivity. This has also been observed with similar metal and semiconductor nanoparticles in the literature.[226] While the thermal conductivity of these nanocrystal arrays are quite low, it is of greater interest how the thermal conductivity of these molecular junctions behave when scaled to the macroscale.

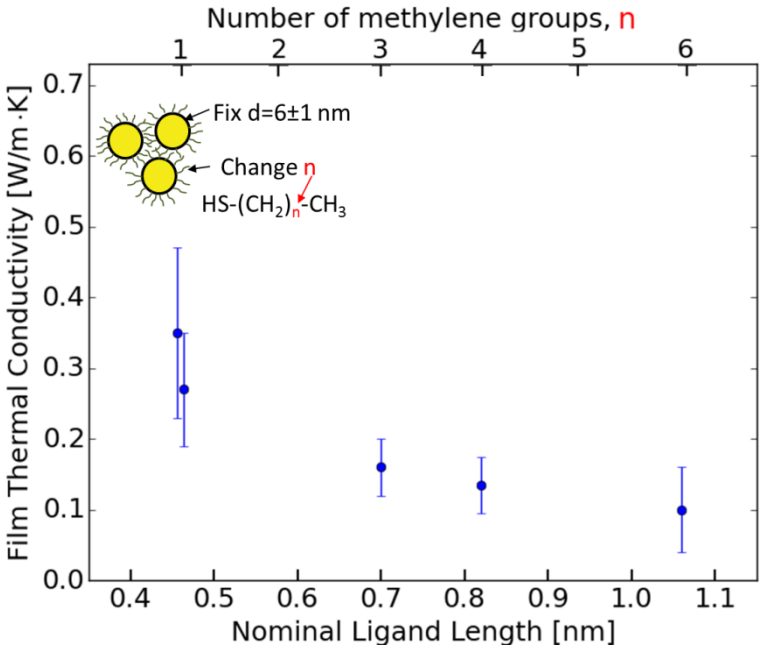


**Figure 3.6:** Thermal conductivity of gold nanocrystal arrays exchanged with alkanethiols. The electronic contribution to the thermal conductivity is neglible as calculated via the Wiedemann Franz, and so the thermal conductivity is primarily from the phononic contribution. As the length of alkanethiol increases, the phononic contribution to thermal conductivity also decreases, resulting in a very low thermal conductivity that is ideal for thermoelectric applications.

The thermal conductivity of single molecule junctions is a topic of great interest, and there are a few studies on the thermal transport on that length-scale.[227] Of most interest is the work of Lee *et al.*, where the thermal conductance is measured through an AFM-based thermal

sensing technique which makes a direct connection with STM-break junction measurements.[227] This work demonstrates an asymmetry in the thermal transport based on coupling of the molecule to the electrodes and Landauer transmission functions. With the experimental thermal conductances of these molecular junctions in hand, we can directly apply the theory of Müller to predict what the thermal conductivity of the scaled molecular junctions should be in an array, show in Equation 3.4.[215] This equation is analogous to the scaled electrical conductivity, dependent on the number of junctions, the length of the junction and the geometry of the nanocrystal. Of course, this theory does not account for any nuances of the mesoscale structure, such as degree of exchange, differences in ligand binding conformation, and certainly the effect of bulk transport such as long-range phonons.[228]

$$\kappa_{NCA} = \frac{N_Y N_Z}{N_x L} M \kappa_{Junction} \tag{3.4}$$

## 3.6 AFM Thermoelectric Measurements of Gold NCA

From the theoretical analysis of these scaled molecular junctions, it is important to investigate how exactly these films are exchanged, and the thermoelectric and electrical properties of the exchanged films. While we have demonstrated SEM and TEM microscopy of these films, conductivity and thermoelectric measurements of these films are lacking on the 100 nm length scale. To solve this issue, we collaborated with Dr. Sergei Maganov at NT-MDT Research, considered a world leader in AFM measurement techniques. The conductive AFM/scanning capacitance microscopy images in Figure 3.7 were taken by Dr. Maganov, while the thermoelectric AFM scans were taken by the author. The primary questions to be addressed in this AFM study was the microstructure after exchange, and if regions of partially exchanged ligands affected the conductivity and thermoelectric behavior.

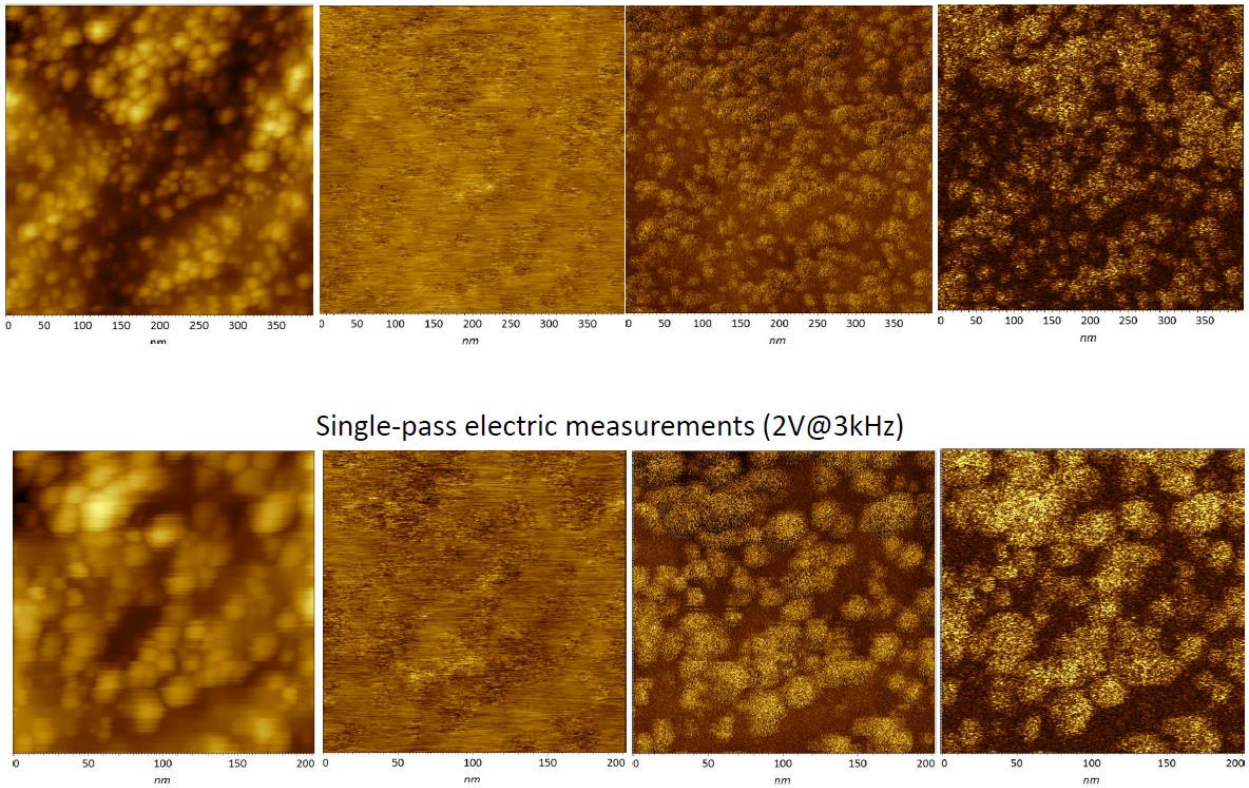


**Figure 3.7:** From left to right: Height topographical map, surface potential (Kelvin force), dC/dZ, dC/dV scans of ethanethiol exchanged gold nanocrystal arrays. The top row is for a 400 nm scan size, the bottom row is a 200 nm scan size. Topographical scans show that the 5 nm nanoparticles have coarsening significantly into domains nearly 20 nm in diameter, with significant porosity due to difference in size between the original oleylamine and ethanethiol. Certain regions in the capacitance scans demonstrate no activity due to lack of electrical conductivity. This indicates that on the surface, more than 10% of the visible scan has un-exchanged ligand domains.

The results in Figure 3.7 demonstrate that the nanocrystals have significantly broadened through the exchange and film-casting process, increasing from the initial 5 nm. The surface potential maps do not show any observations with enough resolution and detail to draw any strong conclusions. The most powerful scans are those related to capacitance, dC/dZ and dC/dV. dC/dZ is the change in capacitance with change in height, and from this we can certainly see that there are many regions throughout the film that are not measurable, because they are not conductive.[229–233] As a percolated network is necessary to enable conduction, we observe that approximately 10% of the film has not been exchanged, and this is only on the surface. It is even more likely that the native oleylamine ligands are present in abundance further down inside the film, as the solid-state ligand exchange depends on the diffusion of short conductive ligands and the back diffusion of the oleylamine molecules. In addition, the density change from an

oleylamine molecule to a shorter alkanethiol ligand results in cracking and porosity in the films, which can be observed in the topographical map and strongly affects the electrical properties.

Thermoelectric imaging of the same ethanedithiol gold nanocrystal array reveals a similar picture. Scanning Seebeck, also known as thermoelectric imaging, is used to detect defects and differences in doping concentrations in spark-sintered inorganic materials.[234–236] Here, instead of differences in doping concentrations, regions that have not undergone ligand exchange will have one Seebeck coefficient, and regions that have exchanged should have the Seebeck coefficient similar to that measured in thin film. Figure 3.8 depict the topographic height, phase and thermoelectric scans on an ethanethiol exchanged gold nanocrystal array. This technique is an extension of contact AFM techniques, compared to the previous set of AFM images which were acquired in tapping mode. Below we observe the same topographical height map, in an expanded 1 um scan size. The images are acquired at 45°C, which results in substantial thermal drift of the piezoelectric, resulting in images that seem stretched in the x-axis. The phase image demonstrates the differences in mechanical properties throughout the material, with three distinct regions. The three regions are the ligand-exchange domains, the un-exchanged domains and pores in the material due to the exchange process. The third and last image is the thermoelectric map with a temperature gradient of 45°C. There is a very clearly defined region (gold) that is in contrast to the dark brown domains. From the measured thermoelectric voltage, it is clear that the brown regions correspond to the electrically conductive, exchanged ligands, while the gold domains are the highly resistive regions with a high Seebeck coefficient. However, this does not alter the observation that the Seebeck coefficient of the conductive regions will be what we measure in the thin film in plane geometry, but the electrical conductivity is highly dependent of extent of exchange.

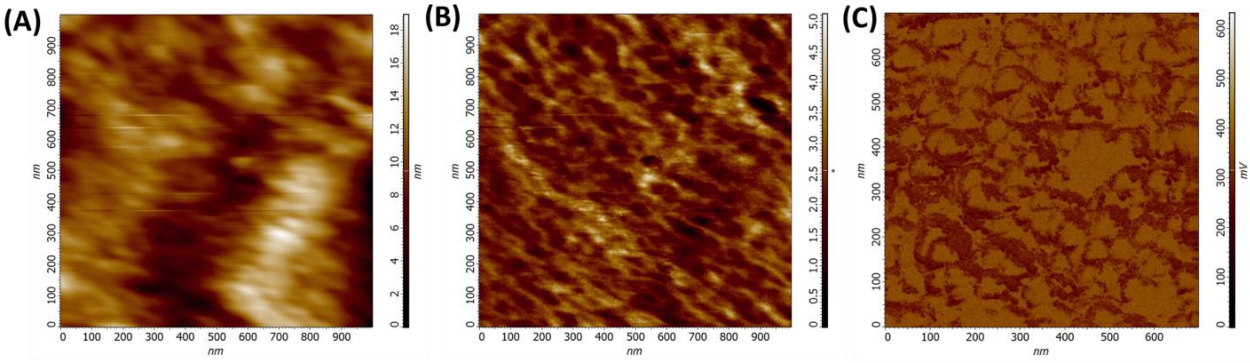


**Figure 3.8:** (A) 1 $um^2$ height scan of the topography of an ethanethiol exchanged gold nanocrystal array. The films appear to be quite smooth after the solid-state exchange. (B) Phase contrast of the same region, with phase contrast stemming from domain differences in mechanical properties (C) Thermoelectric AFM scan at 45°C on a 700 $nm^2$ subset of regions scanned in (A) and (B). Thermoelectric imaging is used to detect defects and regional

inhomegenities, and in this sample the dark regions are regions with complete ethanethiol exchange, and the light regions are native oleylamine bound regions.

## 3.7 Ligands for N-type Thermoelectrics

We have shown that the electrical conductivity and the Seebeck coefficient of the gold nanocrystal array closely match that observed in STM junctions, realizing the hope that gold nanocrystal arrays could be a decent platform for scaling STM junctions to the macroscale. As with Chapter 2, once we have understood the fundamental principles that control the thermoelectric properties on these molecular interfaces as a function of length, we can push forward to establish design rules for the role of binding groups on the thermoelectric properties. To accomplish this, we synthesized and measured the ligands M1-M6 shown in Figure 3.9. The six different binding groups are alkyltrimethyltin, trimethyltin, carboxylic acid, amine, nitrile and of course, thiol. With the help of the spectrochemical series and an understanding of ligand field theory, we can sort the ligands into two sets: "hard" ligands and "soft" ligands.[44–46,237–240] Soft ligands have low charge states and are easily polarizable. These ligands include thiols, amines and nitriles.[241] "Harder" ligands, such as carboanions, the end state of the trimethyltin ligands, have high charge states and are not easily polarizable.[170,237,239,241] The hard and soft ligand categorization is a representation of how much of the bond electron density resides on the molecule or on the metal atom.

There is a strong correlation of the character of the hard and soft ligands to p-type or n-type thermoelectric behavior in phenyl based ligands. With simple alkanethiols we observed a p to n-type switch based on length of the molecule, and with alkanedithiols we observed an overall negative Seebeck coefficients, in these phenyl-based systems we observe that "hard" ligands demonstrate n-type behavior when in a NCA, and "soft" ligands are p-type. There is no discernible trend in the electrical conductivity, unlike in alkanethiols. This is due to the differences in extent of exchange, and the number of bridging molecules in the system. While we can detect the degree of exchange, the number of bridging molecules in the system would be very difficult to experimentally determine.[45]

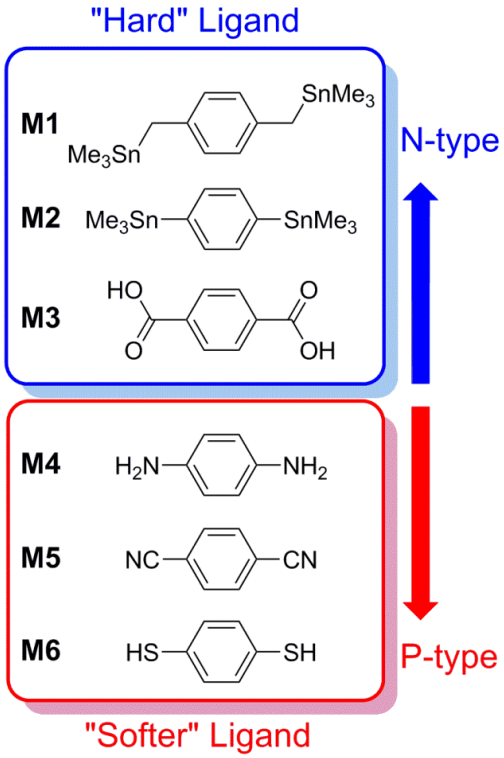


| | Au-Au Junction Length (Å) | σ (S/cm) | $S_{NCA}$ (μV/K) |
|---|---|---|---|
| M1 | 8.22 | 0.001 | -5.45 |
| M2 | 6.87 | 0.00025 | -4.87 |
| M3 | 11.6 | 3.95 | -1.77 |
| M4 | 8.46 | 19.15 | 0.33 |
| M5 | 7.06 | 0.016 | 1.69 |
| M6 | 8.51 | 0.033 | 17.7 |
| Ethanethiol | 4.60 | 0.8 | 2.8 |

**Figure 3.9 & Table 3.1:** The as-synthesized oleylamine ligands on gold nanocrystal arrays are exchanged for phenyl-based ligands, with the films becoming conductive as a result. The phenyl-based ligands are separated into "harder" ligands, which have high charge states and are weakly polarizable, and "softer" ligands which have low charge states and are highly polarizable. Hard ligands are observed to be n-type (electron transporting) while soft ligands are p-type (hole transporting). Typically, a characteristic trend with junction length and conductivity is observed; however, with these disparate binding groups the lack of trend is due to differences in conformation, number of junctions and extent of exchange.

Within Figure 3.10, we present an over-arching diagram to explain the difference between hard and soft ligands. Recall from the STM work where different binding groups primarily affect the coupling parameter, and change the FWHM of the Landauer transmission function. The binding groups, to a lesser extent also change ΔE, the difference in HOMO/LUMO energy level to the Fermi energy of gold. With so many molecules binding to the surface of the nanocrystal, the dominant effect becomes the change in energy upon binding. "Soft" ligands demonstrate higher HOMO energy levels when compared to "hard" ligands, while "hard" ligands have much lower LUMO energies compared to "soft" ligands.[237–239] Therefore, "hard" ligands should demonstrate LUMO transport, while "soft" ligands should have p-type transport. This same theory can be applied to the alkanethiol and alkanedithiol results; with only a single thiol binding, the HOMO energy is close to the Fermi energy, and with an increase of length, more electron density is localized on the molecule, resulting in a "harder" ligand and a lowering of both LUMO and HOMO energies.[237–239] With dithiol ligands, the LUMO levels are much closer to the Fermi energy due to the bond energy, resulting in an n-type material.

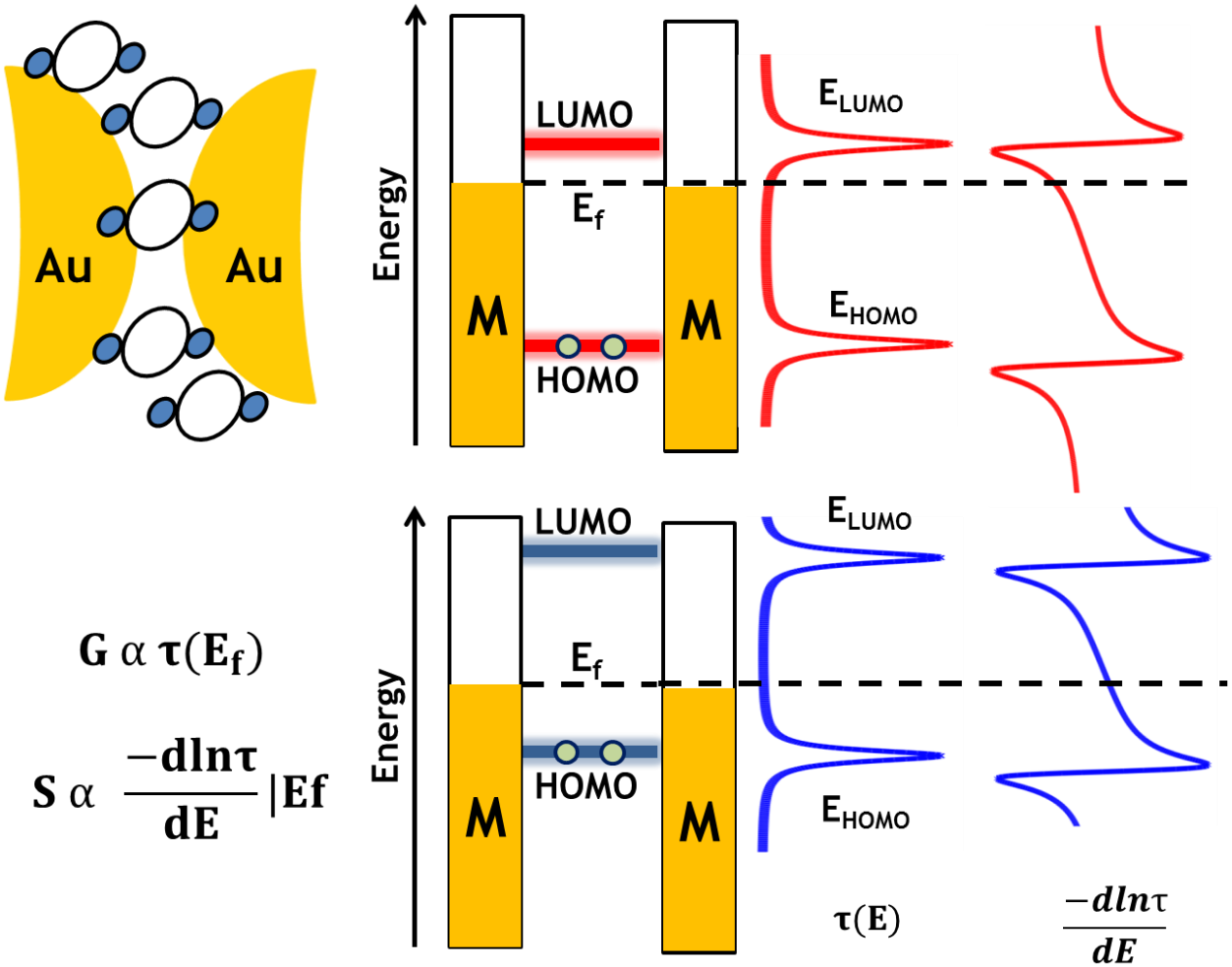


**Figure 3.10:** Transport through the gold nanocrystal junctions is modeled by Landauer transmission functions with transport mainly through the molecular HOMO energy level

($E_{HOMO}$) or LUMO energy level ($E_{LUMO}$). The electrical conductance is proportional to the value of the transmission function $\tau(E)$ at the Fermi energy $E_f$. The Seebeck coefficient is proportional to the derivative of the logarithm of the transmission function evaluated at the Fermi energy, and is negative for transport through the LUMO and positive for HOMO transport. Thus, harder ligands should demonstrate transport through the LUMO, and softer ligands through the HOMO, due to how ligand bonds change the HOMO LUMO energies of the resulting system.

## 3.8 Concluding Remarks on Gold Nanocrystals as Thermoelectric Materials

In this chapter, we demonstrate the potential of using gold nanocrystal arrays to investigate the applicability of single molecule junctions design rules to macroscopic thermoelectric materials. When scaling single molecule junctions to fully functionalized nanocrystal arrays, the ligand length dependence of the electrical conductivity draws a direct parallel to the length dependence of single molecule junction electrical conductance ($\beta_{conjugated}<\beta_{non\text{-}conjugated}$). The ligand length dependence of the Seebeck coefficient was in partial agreement with single molecule literature. Like with molecular junctions, increasing alkanedithiol length decreases the Seebeck coefficient in NCAs. However, the presence of alkanethiol ligands in NCAs resulted in an intriguing p-type to n-type switch in electrical transport with increasing ligand length. While the full nature of this transition is not yet well understood, these results suggest that it may be possible to use surface ligand design to selectively modulate the dominant charge carriers involved in electrical transport, a topic of great interest to the materials community at large.

Within the theoretical framework discussed in this chapter, we believe that two promising routes for enhancing the thermoelectric transport in NCAs are: (1) improving the transport efficiency of individual ligands and (2) increasing the number of ligands participating in inter-particle transport. Based on the high performance demonstrated by oligophenyldithiols in our study, continued efforts are underway to investigate the impact of alternative, highly conjugated ligands. Furthermore, control of particle geometry to improve film packing density in NCAs may help increase the quantity of transport-participating ligands and is also the subject of ongoing research. These initial studies on gold NCAs demonstrate the development of a model platform to build on single molecule thermoelectric research and guide the design of organic-inorganic hybrids that decouple traditionally linked material properties.

We find that tailored binding groups based on STM-BJ measurements can be sorted into hard or soft ligands, based on the textbook spectrochemical series. The ligand type controls the thermoelectric transport, with hard ligands giving n-type transport, and soft ligands resulting in p-type transport. Since hard ligands have lower LUMO energies than soft ligands, and soft ligands have higher HOMO energies in comparison, we can use single molecule theory and Landauer transport to explain the trends we observe.

We see that the conductivity is directly proportional to the number of binding ligands and degree of exchange. We can probe the degree of exchange by using AFM based measurement techniques, and from these measurements almost 10-25% of the film is un-exchanged and non-conductive at the surface. Finally, thermal conductivity of the gold nanocrystal arrays as a function of alkanethiol length allows us to calculate the phonon and electron contribution to the thermal conductivity. We find that these materials have a very low thermal conductivity, close to the amorphous limit, due to the presence of organic-inorganic interfaces and nano-crystalline microstructure.

## 3.9 Experimental Methods

Gold nanoparticles were synthesized following procedures reported previously.[242] 500 mg of gold (III) chloride hydrate (Sigma Aldrich) and 12.5mL of oleylamine were mixed with 62.5 mL toluene in a 250 mL flask. The solution was kept stirring under nitrogen for six hours at 65°C. The solution changed colours from orange to deep purple over the course of the reaction time. It was then cooled and 50 mL of ethanol were added to the reaction mixture and centrifuged at 6000 rpm for 3 min. The supernatant was removed and the precipitate dispersed in 3 mL heptane. To make samples for thermoelectric characterization, glass substrates were sequentially sonicated in the following series of solvents for 15 minutes each: water with 2% liquid alkaline detergent, water, 1M HCL, water, and ethanol. The substrates were then placed in a 5% filtered mercaptopropyl-trisilane in toluene solution overnight, and then sequentially rinsed in toluene, 50/50% toluene/ethanol, and ethanol. 20 µl of the 10 mg/ml Au NP solution was then drop-casted on the cleaned substrates. Upon drying under a heat lamp, films of approximately 1 µm thickness (1$cm^2$ in length) were obtained.

The NCAs are closed packed FCC arrays, with individual nanoparticles five to seven nanometers in diameter. A representative TEM of the gold NCA with native oleylamine ligand is shown in Figure 3.1. Fourier transform of the image in Figure 1a demonstrates the degree of ordering in these films. Ligand exchange from oleylamine to alkanethiols, alkanedithiols, and oligophenyldithiols of varying lengths was performed in the solid state, with each film placed in a two percent solution of the desired ligand in acetone for two hours, and then washed with acetone.[70] All ligand molecules were obtained from Sigma- Aldrich (chemical structures depicted in Figure 3.1). After exchange, the film undergoes changes in porosity with some cracking observed. However, the films remain well-connected electrically and thermally after exchange[207], and nanoparticle sizes did not change significantly. Ideally, the gold nanocrystal array is envisioned to represent the schematic in Figure 3.1. TEM imaging was conducted on a JEOL JEM-2100 microscope at an operating voltage of 200 kV. Films were prepared by spin-coating a dilute nanoparticle solution from a 1:1 Octane:hexane mixture (1000 rpm, 30s) onto silicon nitride grids (Ted Pella, 50 nm thick). Scanning Electron Microscopy (SEM) imaging was

conducted on a Zeiss FESEM-Ultra55 at an operating voltage of 5 kV. Drop cast gold nanoparticle thin films for SEM were prepared on silicon substrates (1cmx1cm).

Using a Nicolet 6700 FTIR-ATR, successful ligand exchange was confirmed by the disappearance of the characteristic IR amine stretch at 3000 $cm^{-1}$ from the oleylamine (SI S5).[243] Thin film absorption spectra were collected using a Cary 50 UV-VIS-NIR spectrometer. Drop-cast gold nanoparticle thin films for the UV-VIS-NIR measurements were prepared on glass substrates (1cmx1cm). The UV-VIS spectra for exchanged gold NCAs with the various dithiol ligands are shown in SI S6. All the UV-VIS spectrums of dithiol exchanged films show a different surface plasmon resonance peak than a film of Au NCA with oleylamine ligands, indicating a different dielectric environment for the gold nanoparticles due to ligand exchange.

Electrical conductivity measurements were made in a four point probe Van der Pauw configuration using Keithley 2400 source meters. Seebeck coefficient measurements were made in a two point probe configuration; a Keithley 2010 was used to sense the thermoelectric voltage under a temperature gradient applied via two Peltier heaters, one at an elevated temperature, and the counterpart held at room temperature. To obtain accurate average Seebeck coefficient readings, one thousand open circuit voltage data points were collected at each applied temperature difference, an approach which parallels the large sample statistics applied to single molecular junction thermoelectric measurements.

The 3-ω technique was used to measure thermal conductivity. Briefly, a polymer dielectric layer was spin-coated onto the gold nanocrystal thin film to electrically isolate the film for accurate thermal measurement. The gold 3-ω pattern was thermally evaporated using an Angstom glovebox evaporator. A current with a controlled frequency is applied across two of the four evaporated gold pads, with the resistance measured across the other two gold pads. By varying the frequency of the applied current and measuring the resistance change, the thermal conductivity of the underlying gold nanocrystal array can be calculated. [221,222,244]

## 3.10 Acknowledgements

We gratefully acknowledge support from the Air Force Office of Science Research (No. MURI FA9550-12-1-0002). Portions of the material characterization was performed at the Molecular Foundry, a Lawrence Berkeley National Laboratory user facilities supported by the Office of Science, Office of Basic Energy Sciences, U.S. Department of Energy, under Contract No. DE-AC02-05CH11231. Synthesis of novel ligands was developed by Dr. Cheng-kang Mai at UC Santa Barbara. Scanning capacitance microscopy was performed by Dr. Sergei Maganov at NT-MDT Research. Thermal conductivity measurements of gold nanocrystal arrays were performed by Geoff Wehmeyer at UC Berkeley.

# Chapter 4: The Role of Ions for Ionic and Mixed Conductor Thermoelectrics

## 4.1 Theoretical Treatment of Ionic Thermoelectrics

The movement of holes and electrons due to a thermal gradient, termed the thermoelectric or Seebeck effect, is a much investigated phenomena due to its potential as a means of recovering waste heat in the form of electrical work. This effect has been known for over 150 years and has been thoroughly investigated in many inorganic materials such as the prototypical $Bi_2Te_3$.[2,245] However, many conventional thermoelectric materials are brittle and inflexible limiting their potential utility in proposed thermoelectric applications such as wearable devices. In recent years, research has expanded towards the investigation of ion motion induced by a thermal gradient in solutions and ionic liquids.[246–249] These systems rely on a redox couple dissolved in solution to allow direct current measurements and are termed thermogalvanics, and implementation is difficult due to their liquid nature.[131,129,250,128,130,251] To our knowledge, no study to date has investigated thermally induced ion transport in single-ion conducting polymer systems to harvest waste heat.

Thermogalvanic and thermoelectric materials are characterized by the figure of merit $zT$ as shown in Equation 4.1, where $S$ is the Seebeck coefficient, $\sigma$ the electrical conductivity and $\kappa$ the thermal conductivity. The Seebeck coefficient, detailed in Equation 4.2, is the voltage measured across the material with respect to a varying temperature gradient under the open-circuit condition.

$$zT = \frac{S^2\sigma}{\kappa}T \tag{4.1}$$

$$S = -\frac{\Delta V}{\Delta T} \text{ @ Open-Circuit} \tag{4.2}$$

In this chapter section, we will primarily use the Newman analysis of thermogalvanic cells,[133] where the Seebeck coefficient of a thermogalvanic cell can be expressed as the summation of the electrochemical potential gradient under a temperature gradient, divided by Faraday's constant (Equation 4.3). The Seebeck coefficient is comprised of two important terms, the first term being the entropy change of the reaction, and the second term is the related to the concentration of an ionic species $c_i$ and thermodiffusion of said ionic species ($D^T$), via Equation 4.4. Since the index for the solvent is 0, the thermodiffusion of each ionic species is always in relation to the solvent.

$$S = -\frac{\nabla\mu_n}{F\nabla \mathrm{T}} = \frac{\bar{S}_n}{\mathrm{F}} + \frac{z_n F}{T\sigma}\sum_i z_i c_i A_i^0 \tag{4.3}$$

$$A_j^i = \frac{D_j^T}{\rho_j} - \frac{D_i^T}{\rho_i} \tag{4.4}$$

This thermodiffusion component is directly related to the Soret effect, where the Soret coefficient is presented in Equation 4.5 as a summation of the thermodiffusion of each ion in relation to the solvent and the transference number divided by the diffusion coefficient. Hence, it is shown that the Seebeck coefficient is simply the result of entropy changes per ion manifesting as a thermoelectric voltage, where the entropy changes can stem from either the chemical reaction or result in thermodiffusion of ions.

$$\sigma_T = \frac{1}{DT}\left(t_-^0 A_+^0 + t_+^0 A_-^0\right) \tag{4.5}$$

This chapter section demonstrates experimentally a novel application of these above principles to ion conducting, solid-state polymer systems where a temperature gradient drives ion motion and results in a voltage difference, giving rise to the observed Seebeck effect. This phenomenon is demonstrated in two ion conducting polymers which exhibit opposite voltage differences with the same temperature gradient. A switch is observed in the sign of the Seebeck coefficient from positive to negative corresponding to a change in the direction of ion motion from along the thermal gradient to against the thermal gradient, and is seen to be both dependent on the ion concentration and the humidity.[135] The analysis of the Seebeck coefficient from Newman will be directly applied to this work,[133] and can be simplified since there is only one ionic species capable of thermodiffusion in this cation conductor, since the anions are tethered to the polymer backbone. It is demonstrated that such a switch can be theoretically explained via the Soret effect outlined in Equation 4.5. These results have implications for engineering materials with negative or positive Seebeck coefficient even for a fixed type of mobile ion.

To investigate the thermogalvanic effect in single-ion conductors, two novel material systems were used, silver Nafion (Ag-Nafion) and silver polystyrene-sulfonate (Ag-PSS). Both of these systems are water processable, solid-state ionomers with sulfonate groups exhibiting high ionic conductivity, with the precursor Nafion being the most widely studied ionomer due to its high proton conductivity derived from water in channels.[252] The incorporated silver ions in Ag-Nafion and Ag-PSS generate a voltage via an ion concentration gradient by the generalized Soret effect, where a temperature gradient results in a migration of molecules along or against a temperature gradient bounded by silver electrodes.[247,253–255] This allows a temperature gradient across the film to be directly converted to an electric current via electrochemical reactions at the electrodes, resulting in silver entering the system at the cathode and depositing at the anode. The direction of the ion current is dependent on the Soret coefficient and will depend strongly on the local environment surrounding the ions.[135,255] Lastly, since the sulfonate ion is tethered to the polymer backbone, only the silver ion is mobile under the applied temperature gradient, so that the Seebeck coefficient is purely a result of silver ion motion, simplifying the analysis. In conventional thermoelectrics, oppositely charged minority carriers under the influence of a temperature bias would result in a thermoelectric potential opposing that of the majority carrier,

reducing the magnitude of the Seebeck coefficient, which can be avoided by tethering the counterion.[2]

## 4.2 Silver Polyelectrolytes Thermoelectric Properties

A general schematic for the experimental setup is shown in Figure 4.1A. The two ion-conducting materials, Ag-PSS and Ag-Nafion, are shown in Figure 4.1B. Briefly, the ion-conducting polymer is deposited via drop casting from an aqueous solution (1 wt%) on 1 $cm^2$ glass substrates and electrical contact is made by depositing silver electrodes. The thermoelectric voltage and current are measured across said electrodes with a Keithley 2400 multimeter. Accurate temperatures on the hot and the cold side were measured with thermocouples placed parallel to the electrodes. Figure 4.1C depicts the effect of increasing $Ag^+$ concentration on the measured Seebeck coefficient, with Ag-PSS exhibiting a positive Seebeck coefficient of 5 mV/K, and Ag-Nafion demonstrating a negative maximum Seebeck coefficient of -1.5 mV/K. These measurements are done at room temperature, with the Ag-Nafion at a RH of 75% and Ag-PSS at a RH of 40%. The difference in the sign of the Seebeck coefficient is both interesting and unexpected; while both systems are ionomers containing sulfonate counterions with mobile $Ag^+$ ions and silver electrodes, $Ag^+$ in Ag-PSS experiences $Ag^+$ thermophoresis from hot to cold, while $Ag^+$ in Ag-Nafion moves from the cold to hot electrode.

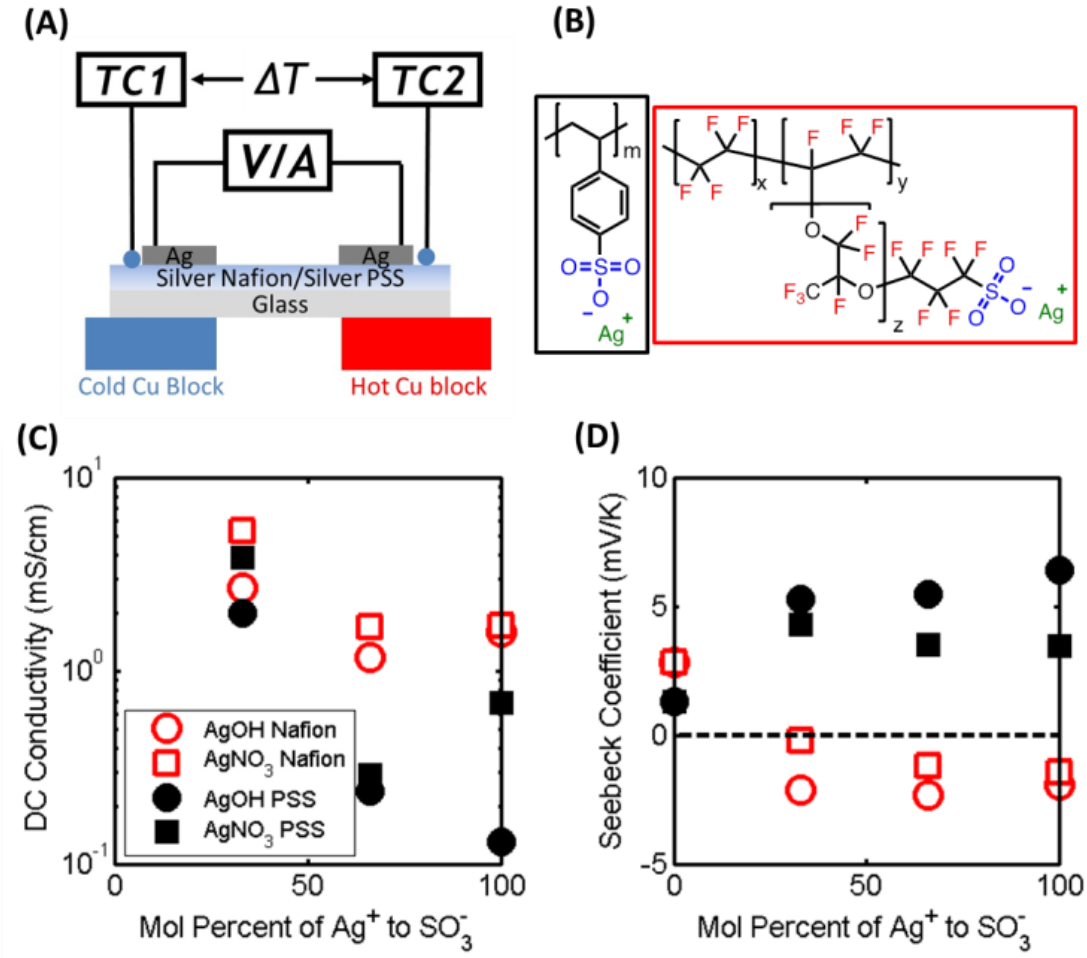


**Figure 4.1:** (A) Schematic of measurement setup in humidity-controlled environment, where either silver Nafion or silver PSS is measured in the setup. The leads are stainless steel to copper wires, which have a known Seebeck coefficient of 5μV/K, which is much smaller than the polymer. (B) Chemical structures of Ag-PSS (black box) and Ag-Nafion (red box) (C) DC conductivity of Ag-Nafion (open red symbols) and Ag-PSS (filled black symbols) with increasing molar ratio of $Ag^+$ to polymer $SO_3^-$ groups. The initial protons are exchanged using silver hydroxide, AgOH (circles) and silver nitrate, $AgNO_3$ (squares). The DC conductivity is observed to be highest at 33% $Ag^+$:$SO_3^-$ (D) Plot of Seebeck coefficient of Ag-Nafion and Ag-PSS with increasing molar ratio of AgOH and $AgNO_3$ to $SO_3^-$ groups. The legend scheme is identical to Figure 4.1B. The Seebeck coefficient increases in magnitude with additional $Ag^+$ concentration. The addition of $Ag^+$ causes a further enhancement in the Seebeck coefficient of Ag-PSS, while the Seebeck coefficient of Ag-Nafion becomes negative; indicating a flux of $Ag^+$ from cold to hot, counter to the temperature gradient. The error bars are on the scale of the data point. It should be noted that Ag-Nafion was measured at RH=75% and Ag-PSS was measured at RH=40%.

Samples with different $Ag^+$ concentration were prepared by varying the molar ratio of the Ag salt to the sulfonate functionality in the polymer. At 0% $Ag^+$ concentration, the system has purely proton conduction, and protons are progressively exchanged to $Ag^+$ ions to by introduction of AgOH and $AgNO_3$ and dialysis. X-ray photoelectron spectroscopy data suggest successful incorporation of $Ag^+$ into the polymer with no detectable signal from other impurities, as seen in Figure 4.2.

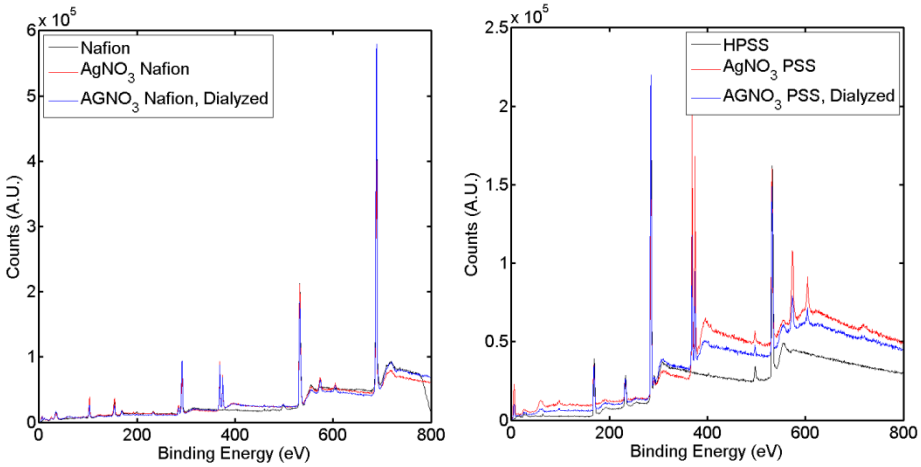


**Figure 4.2:** (Left) Full XPS spectrum of 100% $AgNO_3$ Nafion, dialyzed 100% $AgNO_3$ Nafion, and proton form Nafion. Peaks near 390 eV indicate quantitative silver exchange. There is not a noticeable difference between material peaks pre and post-dialysis. (Right) Full XPS spectrum of 100% $AgNO_3$ PSS, dialyzed 100% $AgNO_3$ PSS, and polystryrenesulfonic acid. Peaks near 390 eV indicate quantitative silver exchange.

As the concentration of $Ag^+$ is increased in the ion conducting polymers, the conductivity and Seebeck coefficient is expected to change dramatically. Figure 4.1B demonstrates a decreasing DC conductivity with increasing silver concentration, with peak conductivities measured at 33% $Ag^+$:$SO_3^-$ molar ratios resulting in values of 2.7 mS/cm for Ag-PSS and 4.3 mS/cm for Ag-Nafion. Electrical conductivity was measured with four point probe Van de Pauw technique, and checked with I-V sweeps shown in Figure 4.3. With no Ag+ ions free to move within the film, the films demonstrate capacitive behavior, with the film resistance increasing over time, resulting in a non-linear IV sweep.

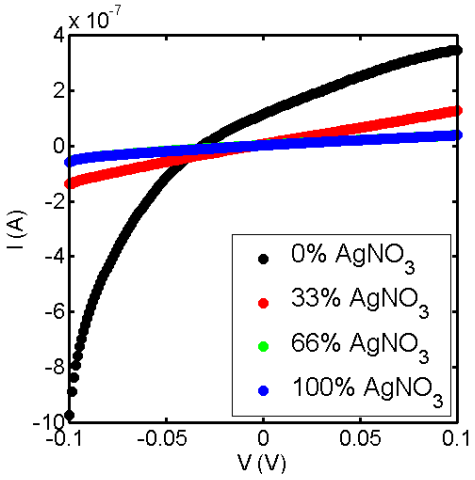


**Figure 4.3:** Current-voltage plots for concentration dependence of $AgNO_3$ in Nafion. No silver in the film results in a non-linear I-V sweep, indicative of a capacitive film with no charge extraction.

Figure 4.4 shows that these ion conductivities in these materials are indeed stable over time and remain so as long as silver is available at the electrodes. At higher applied voltages ($\Delta V>1V$) and an electrode spacing of 500 μm, silver dendrite formation occurs in silver Nafion, which is qualitatively similar to dendrite growth in batteries and could be solved via similar design of polymer structures.[256] The concentration study of Ag-Nafion was performed at a relative humidity of RH=75%, while the Ag-PSS was performed at RH = 40%. It will be shown that humidity strongly influences the ion conductivity and Seebeck coefficient in these materials.

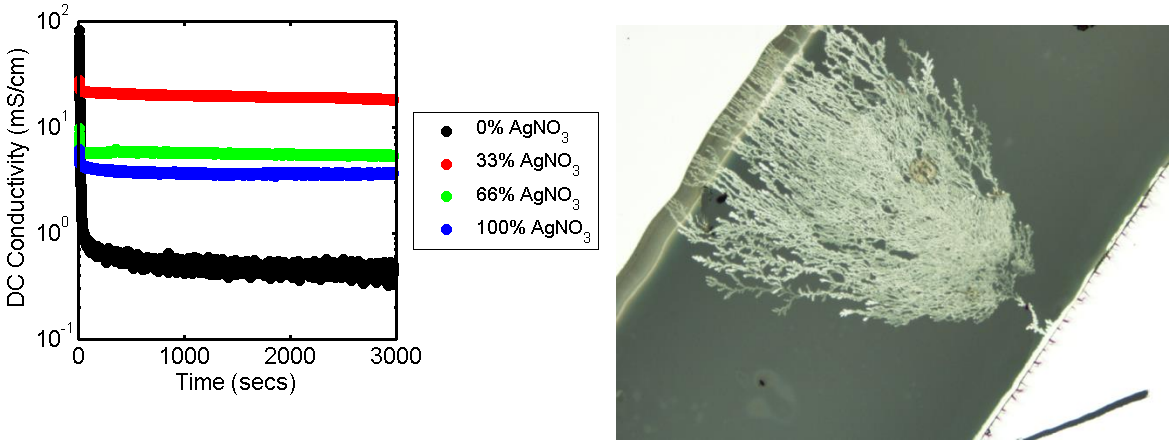


**Figure 4.4**: Electrical conductivity measured over time at constant 100 mV potential of silver Nafion with silver electrodes. Conductivity of system remains stable, until dendrite bridging results in material failure.Dendrite formation in 100%$AgNO_3$ in PSS, spun coated on glass, with

10 μA applied over one hour. Electrical resistance drops from 160 MΩ to 30 MΩ. Distance between electrodes is 500 μm.

Figure 4.5 are repersentative thermoelectric voltage plots for 100% Ag-Nafion and 100% Ag-PSS. Since Ag-Nafion as a positive slope and the Seebeck coefficient is the negative of the slope, Ag-Nafion has a negative Seebeek coefficient. While in conventional thermoelectrics, positive and negative Seebeck coefficients refer to whether the material transports holes or electrons. This is clearly not the case in Ag-Nafion and Ag-PSS; both materials do not transport electrons or holes, and the only moving ions are the Ag+ ions. Therefore, from the thermoelectric experiments, Ag+ ions must move from the cold to hot electrode, with a negative thermodiffusion coefficient. The opposite is true for Ag-PSS.

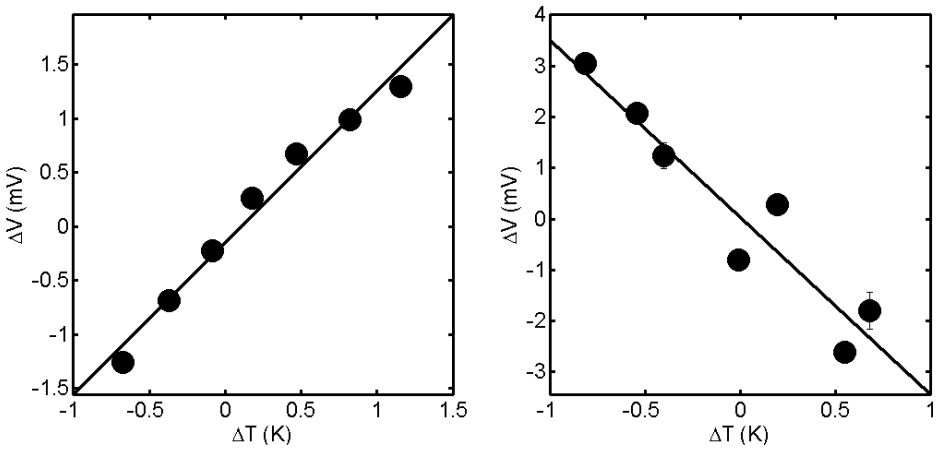


**Figure 4.5:** (Left) Thermoelectric voltage versus temperature gradient for 100% $AgNO_3$ Nafion, where Seebeck coefficient was measured to be -1.4 mV/K. Thermoelectric voltage versus temperature gradient for 100% $AgNO_3$ PSS, where the Seebeck coefficient was measured to be S= 3.4 mV/K

In order to confirm that Ag-Nafion was indeed n-type, we can use to our advantage the fact that these materials should output a thermoelectric current that is a product of the Seebeck coefficient and the conductance of the film. By measuring the thermoelectric current produces as a function of temperature gradient, we can test whether the materials have a negative Seebeck coefficient. These results are displayed in Figure 4.6, and indeed confirm that the Seebeck coefficient of 100% Ag-Nafion is negative, and that the Seebeck coefficient calculated using the Joule-Thompson equation gives a value very close to that observed in the open-circuit voltage measurements.

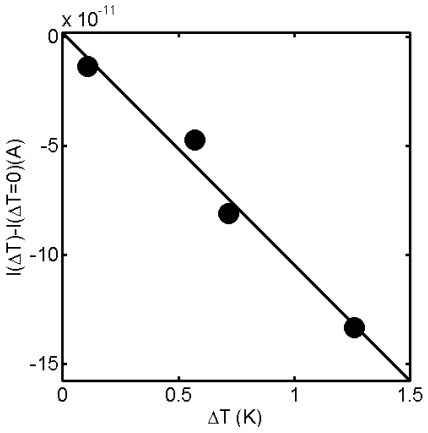


**Figure 4.6:** Thermoelectric current with temperature gradient of 100% $AgNO_3$ Nafion. SG= -1.06$e^{-10}$ A/K

## 4.3 Humidity Effects on Thermoelectric Properties of Silver Polyelectrolytes

It is well known that the ionic conductivity of Nafion is extremely humidity dependent due to water-assisted ion transport, and so the effects of humidity on the conductivity and Seebeck coefficient of these materials are of great interest.[257] Humidity-controlled measurements of the Seebeck coefficient and DC conductivity at 100% $Ag^+$:$SO_3^-$ molar ratios of Ag-Nafion and Ag-PSS were conducted to investigate these effects. Figure 4.7 shows the exponential increase in the measured DC ionic conductivity in Ag-Nafion and Ag-PSS, where a change in humidity over 80% can control the conductivity by over three orders of magnitude. Ag-Nafion exhibits DC conductivity slightly lower than Ag-PSS but a higher $Ag^+$ mobility, since the $Ag^+$ concentration in Ag-PSS is over five times higher than in Ag-Nafion due to the higher $SO_3^-$ concentration in Ag-PSS. The higher ion mobility in Ag-Nafion is attributed to the presence of percolated channels in Nafion.[258,126]

In conventional thermoelectrics based on electron transport, the conductivity and Seebeck coefficient are often inversely correlated.[2] However, this is not true for in Ag-Nafion and Ag-PSS, as shown in Figure 4.7. Initially, at RH=30%, the Seebeck coefficient of both Ag-Nafion and Ag-PSS are positive, while the DC conductivity of the materials is low. When the materials are exposed to an increased humidity of RH=40%, the Seebeck coefficient decreases but remains positive for Ag-PSS, and is near zero for Ag-Nafion, which is the beginning of the switch of the sign of the Seebeck coefficient. At RH > 50% there is an observable increase in the magnitude of the Seebeck coefficient of Ag-PSS and Ag-Nafion, plateauing at -2 mV/K for Ag-Nafion and 5 mV/K for Ag-PSS. This happens concurrently with the exponential increase in the conductivity of these polymers, demonstrating simultaneous increase in both S and σ with increasing relative humidity. Not only does humidity demonstrate a strong role in tuning the DC ion conductivity

and Seebeck coefficient of Ag-PSS and Ag-Nafion, it also reveals a decoupling of $S$ and $\sigma$ at higher humidity, with the power factor $S^2\sigma$ increasing with increasing relative humidity.

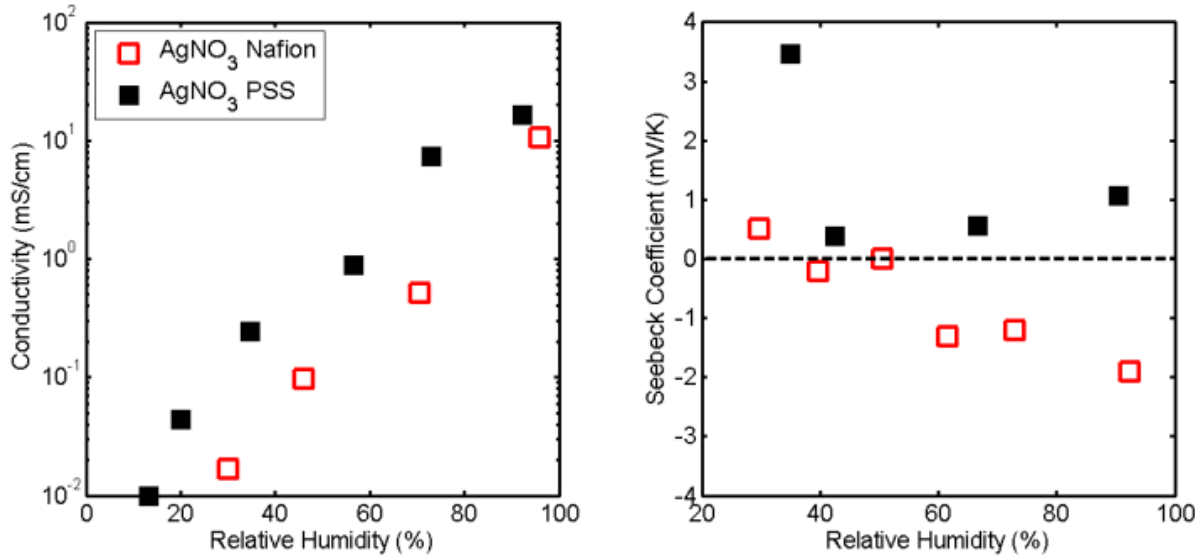


**Figure 4.7:** (Left) DC ionic conductivity versus relative humidity for 100% $Ag^+$:$SO_3^-$ PSS (black filled squares) and 100% $Ag^+$:$SO_3^-$ Nafion (red open squares). The DC ionic conductivity ranges over three orders of magnitude, over the range of 10% to 100% relative humidity. The strong DC ionic conductivity dependence emphasizes the dominance of water to the ion transport through ionomers (Right) Seebeck coefficient versus relative humidity for 100% $Ag^+$:$SO_3^-$ PSS (black filled squares) and 100% $Ag^+$:$SO_3^-$ Nafion (red open squares). Initially at RH<40%, the Seebeck coefficient of Ag-PSS and Ag-Nafion are positive. At RH > 40%, the Seebeck coefficient of Ag-PSS begins to increase to 1 mV/K, and Ag-Nafion begins to switch from positive to negative. Of interest is the decoupling of S and σ from the conventional inverse relationship with increasing humidity, and highlights the importance of controlled humidity for tuning the properties of Ag-PSS and Ag-Nafion.

In addition, as these materials are conjugated polyelectrolytes with relatively high dielectric constants, we hypothesized that the dielectric constant would be a strong function of temperature. To test this, we performed AC-impedance on Ag-PSS at a relative humidity of 90%. These results are plotted in Figure 4.8. From AC-impedance, the dielectric constant can be normalized with relation to the high frequency dielectric constant data. With this treatment, it is observed that with increasing temperature, the dielectric constant of the material decrease significantly. While it was proposed that in Ag-Nafion the dielectric constant would have a different temperature dependence compared to Ag-Nafion, experimentally we found that the two materials have similar temperature dependences, and that the dielectric constant changing as a function of temperature is not the rationale for the switch in sign of the Seebeck coefficient.

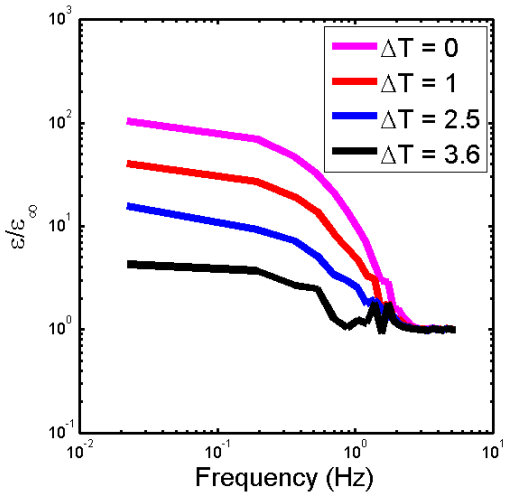


**Figure 4.8:** Normalized dielectric constant of Ag-PSS at 90% relative humidity measured as a function of frequency. These trends are similar to those observed for Ag-Nafion.

## 4.4 Theoretical Analysis of Negative Seebeck Coefficients in Ion Conductors

In order to decipher the origin of the switch in the Seebeck coefficient from positive to negative in Ag-Nafion, a return to Equation 4.3 is necessary. The electrochemical half-cell reactions occurring at each electrode can be described by the following reaction:

Electrode 1: $\boldsymbol{Ag_{(s)}} \leftrightarrow \boldsymbol{Ag^{+}_{ionomer}}$ , Electrode 2: $\boldsymbol{Ag^{+}_{ionomer}} \leftrightarrow \boldsymbol{Ag_{(s)}}$

It is noted that the entropy change of this chemical reaction should be minimal, as the number of moles of product and reactants are the same. Therefore, Equation 4.5 can be simplified to the following equation, as $\Delta S_{rxn}$ is negligible:

$$S = \frac{F}{T\sigma} c_{Ag+} A_{Ag+}^{H20} \tag{4.5}$$

This demonstrates that the main contribution to the Seebeck coefficient observed must come from the Soret effect, as described in Equation 4.6. Since these materials are ion conductors mediated by water, and the counterions are tethered to the backone, the 0 index is assigned to water. From Equation 4.5, $\boldsymbol{A_{Ag}^{H20}}$ can be further simplified to the following Equation 4.7, since the thermodiffusion of the anion is negligible:

$$A_{Ag+}^{H20} = \left(\frac{D_{Ag+}^{T}}{\rho_{Ag+}} - \frac{D_{H20}^{T}}{\rho_{H20}}\right) = DT\sigma_T \tag{4.6}$$

Now, the origin of sign of the Seebeck coefficient is clearly a result of the balance of the thermodiffusion coefficient of $Ag^+$ and water inside Ag-Nafion. Therefore, in Ag-Nafion, $\frac{D_{H20}^T}{\rho_{H20}}$ must be greater than $\frac{D_{Ag+}^T}{\rho_{Ag+}}$, resulting in a negative Soret coefficient as water diffuses from the hot to cold much more readily than $Ag^+$, resulting in silver flux from cold to hot, which is perceived as a negative value. It should be noted that with Ag-Nafion, a Seebeck coefficient of -1 mV/K is equivalent to a Soret coefficient of -0.04 $K^{-1}$ via Equation 4.7, which is derived for single-ion conductors where the entropy change from the chemical reaction is negligible and where the diffusion coefficient and ionic conductivity are related via Einstein kinetic theory. The Soret coefficient calculated is similar in magnitude to experimental Soret coefficients observed with polystyrene beads which also move from cold to hot under certain temperature regimes.[255]

$$S = \frac{Fk_BT}{q^2}\sigma_T \tag{4.7}$$

## 4.5 Flexible Thermogalvanic Devices using Silver Polyelectrolytes

We can construct devices by using Ag-Nafion and Ag-PSS, as the Seebeck coefficient for both materials have different signs. The first device constructed was a four leg device on glass with bridging painted silver electrodes in a conventional thermoelectric module geometry, from which useable power can be extracted from a temperature gradient, as seen in Figure 4.9. The current flow from the device and the voltage drop across a 1 kΩ resistor was monitored with different temperature gradients. The power output from this device with a temperature gradient of 1.5 K and 4 K was $1e^{-13}$ W and $6e^{-13}$ W, respectively.

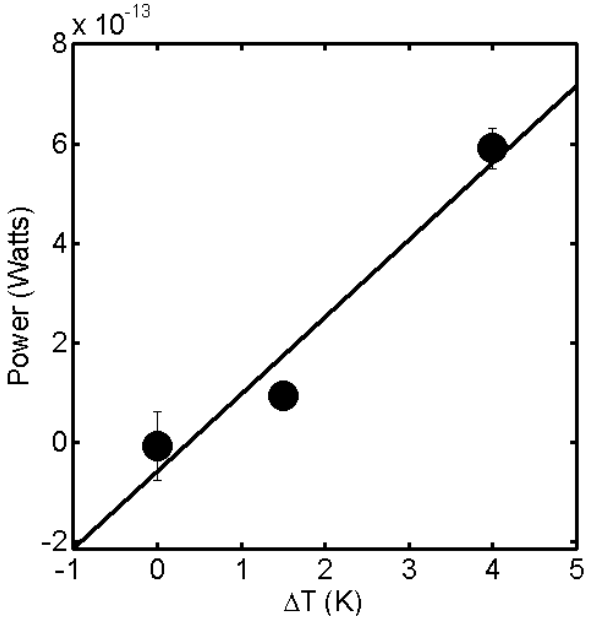

**Figure 4.9**: Power output from four leg module on glass across a 3.7 kΩ resistor. Since the device had a 0.5 MΩ resistance, the power output is not impedance matched, and is non-optimal. However, this shows that these materials can produce useable electrical power from a temperature gradient. $P = 1.55e^{-13}\Delta T$

Furthermore, the water processeability enables construction of a flexible module on a Kapton membrane supported by paper, as seen in Figure 4.10A. The device has six legs thermally in parallel, with alternating legs of 100% Ag-PSS (positive Seebeck coefficient, denoted by p) and 100% Ag-Nafion (negative Seebeck coefficient, denoted by n) connected via silver paint. Measurements of the thermoelectric voltage were then taken across an increasing combination of legs, from the full six legs to a single leg, as shown in Figure 4.10B. With each additional leg, an increased thermoelectric voltage with temperature bias is measured, and the resulting Seebeck coefficient of each additional pairs of legs is plotted in Figure 4.10C, showing that with each additional leg, the overall module Seebeck coefficient across the device is increased. It is apparent in the module Seebeck coefficient that Ag-PSS and Ag-Nafion are strongly sensitive to humidity, since the Ag-PSS legs strongly out-perform the Ag-Nafion legs at room humidity (RH=50%).

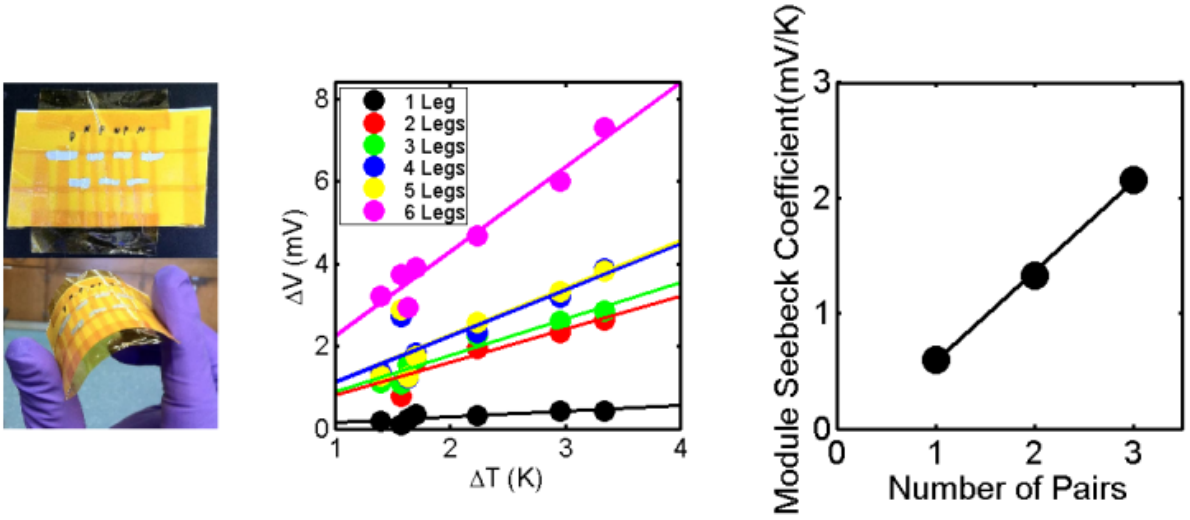


**Figure 4.10:** (Left) Picture of a six leg flexible module, constructed using a Kapton membrane and paper, with p labeling the Ag-PSS legs and n labeling the Ag-Nafion legs. (Middle) The thermoelectric voltage of the module increases with each additional leg at each temperature bias, measured from right to left. (Right) The module Seebeck coefficient is shown to increase with additional pair of legs. These were measured at room temperature and room humidity (RH=50%).

Now, there remains the question of whether the origin of the measured voltage is due specifically to the thermodynamics at the electrodes or due to thermal transport within the polymer itself, as claimed previously for Equation 4.6. In order to test this, three devices were

constructed with varying number of paired legs. The silver contacts connecting each Ag-Nafion and Ag-PSS leg was eliminated, and the polymers were cast in intimate contact with one another, so that the only silver contacts present were at the terminal end of the device. This allows one to vary the number of paired legs while holding the number of silver contacts constant at two. The two paired leg device is shown in the inset of Figure 4.11. The thermoelectric voltage is measured in these three devices in Figure 4.11, and the Seebeck coefficient of these devices are extracted and plotted. From this, it is observed that regardless of the number of Ag contacts, the Seebeck coefficient of the devices scale with the number of paired legs; therefore, the voltage measured must be from transport within the polymer, and not due to the chemical reaction and entropy of reaction at the silver-polymer interface, and that the assumptions that lead to Equation 4.6 are valid.

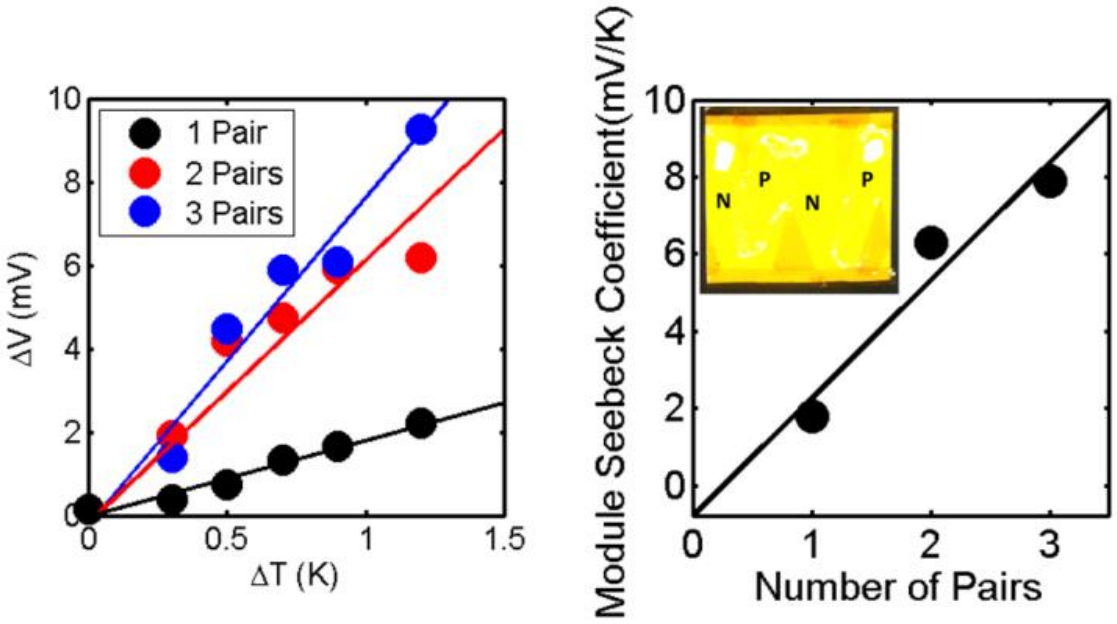


**Figure 4.11:** (Left) Thermoelectric voltage of three different two silver contact devices, ranging from one pair (Ag-Nafion/Ag-PSS) of legs to three pair of legs. The measurements was made at RH= 70%. (Right) The Seebeck coefficient of each device is plotted with respect to the number of pairs measured. By holding the number of contacts constant, and varying the number of legs, the module Seebeck coefficient is shown to be related to transport within the polymer, and not to the thermodynamics at the electrode-polymer interface (Inset) A two leg device with terminal contacts is displayed.

Both Ag-PSS and Ag-Nafion have ion conductivities in the range of mS/cm, so thermal conductivity is expected to be dominated by phonon transport through the ionomer, not by the heat transported by ions or electrons. The thermal conductivity values measured via time-domain thermoreflectance[259] confirm this, showing that Ag-Nafion has a thermal conductivity of 0.22±0.02 W/(m K), which is essentially the same as the measured thermal conductivity of

proton form Nafion, 0.20±0.02 W/(m K) . The measured thermal conductivity is similar to that measured by other methods in the literature for Nafion.[260] This confirms that the addition of silver does not significantly change the thermal conductivity of these materials, within error. The thermal conductivity of Ag-PSS was measured to be 0.40±0.02 W/(m K) , and with these thermal conductivity values the figure of merit zT for Ag-Nafion and Ag-PSS was calculated. At 26°C and room humidity (RH=50%), a maximum ZT of 0.006 for 33% $AgNO_3$ PSS, and 0.003 for 33% AgOH Nafion is observed. While these figures of merit are competitive with organic thermoelectrics and lower than conventional inorganic thermoelectrics such as $Bi_2Te_3$, the prospect of a decoupled Seebeck coefficient from conductivity and the extensive library of ionomers could lead to great future discoveries.[2,261,262]

## 4.6 Conclusion of Pure Ion Conductor Thermoelectrics

Ag-Nafion and Ag-PSS are ion conducting polymers, and exhibit DC conductivity and a very large Seebeck coefficient, with a low thermal conductivity. Thermogalvanic properties for both silver conducting ionomers are strongly controlled by humidity. An analysis of the ion transport under a temperature gradient is stated, rooted in the entropy of the chemical reaction and the Soret effect, and a possible explanation of the switch in the sign of the Seebeck coefficient of Ag-Nafion is given in terms of thermodiffusion of $Ag^+$ and water molecules. The effects of the entropy of the chemical reaction on the Seebeck coefficient is found to be small by constructing devices with varying pairs of legs but constant number of contacts. Finally, a flexible, water processable, solid state polymer thermogalvanic device was demonstrated. The zT of Ag-Nafion and Ag-PSS was found to be 0.006 and 0.003, comparable to organic thermoelectrics. To the best of our knowledge, this is the first solid-state, polymer thermogalvanic device in the literature using single-ion conductors, featuring solution processability, flexibility and air stability.

## 4.7 Mixed Conductors for Thermoelectric Applications

Conductive polymers such as PEDOT:PSS hold great promise as flexible thermoelectric devices. The ionic Seebeck effect transiently enhances the Seebeck coefficient in PEDOT:PSS at high relative humidity. In this section an underlying fundamental theory to the transient decay in the ionic thermoelectric voltage is proposed, and from this understanding it is possible to design a material where the ionic effect can be extended in time. The proposed model incorporates the observed phenomenon of the thermoelectric transport of the holes and ions in systems where there is no chemical reaction at the electrodes and in the situation where ions are injected and extracted from the system. Using fundamental design rules, a material is designed with long-

lived ionic Seebeck enhancements. The thermal properties of the material are discussed, along with shortcomings of the ionic Seebeck effect.

Thermoelectrics are of interest as a solid-state technology to harvest useable electrical power from waste heat or as a cooling material for thermal management applications.[2] Conventional thermoelectrics are typically hard, inflexible inorganics such as $Bi_2Te_3$, and are useful for waste heat recovery in automobile engines.[245] However, there are many near room temperature applications such as flexible thermoelectric fabrics for cooling are enabled by the processeability and flexibility intrinsic to polymers.[261] Thermoelectric performance is characterized by the figure of merit ZT.

Conducting polymers as thermoelectric materials are of interest, where the electrical conductivity ($\sigma$) can be as high as 1000 S/cm with Seebeck coefficients (S) near 20 uV/K,[261,96] and a thermal conductivity ($\kappa$) of 1 W/(m K).[94] In organic thermoelectric materials, there are well-known methods to control the electrical conductivity, but strategies to increase the Seebeck coefficient without changing the electrical conductivity are a topic of great interest, as the Seebeck coefficient and electrical conductivity are normaly inversely coupled.[2] While improvements to the Seebeck coefficient of inorganic materials has been demonstrated via band structure engineering,[3,4,6,83,263] implementation is difficult in conjugated polymers due to the large degree of disorder and lack of a band structure.[73,107,264,100,265] However, the disordered nature of the conjugated polymer can be turned into an advantage, since many polymers such as poly-styrenesulfonic acid (H-PSS), at high relative humidity conditions, allow conduction of ions at room temperature due to water uptake.[257,262,266,267] The movement of ions under a temperature gradient in the mixed conductor PEDOT:PSS has been shown to result in a high ionic Seebeck coefficient, as shown recently by Wang *et al.;* however, the ionic Seebeck effect decays rapidly with time, resulting in an enhancement to the thermoelectric power factor for a few seconds.[268] The understanding of this transient thermoelectric voltage that is present in mixed conductors, whether organic or inorganic, is lacking.

In this section an underlying fundamental theory to the transient decay in the ionic thermoelectric voltage is proposed, and from this understanding it is possible to design a material where the ionic effect can be extended in time. The proposed model incorporates the observed phenomenon of the thermoelectric transport of the holes and ions in systems where there is no chemical reaction at the electrodes and in the situation where ions are injected and extracted from the system. A method is described to improve the ionic Seebeck coefficient of PEDOT:PSS using silver poly-styrenesulfonate (Ag:PSS) and silver electrodes, and a characterization of the material's electrical, thermal conductivity and Seebeck coefficient is shown in comparison to PEDOT:PSS. By incorporating Ag:PSS into the PEDOT:PSS matrix, there is a significant power factor enhancement over time compared to PEDOT:PSS. The electrical conductivity decreases by an order of magnitude due to the addition of non-conjugated polymer. The ionic Seebeck effect is further characterized by a thermoelectric voltage relaxation response upon the removal of the temperature gradient, and is shown that since the ionic Seebeck effect relies on a constant

flux of ions to generate a high thermoelectric voltage, and by applying the proper ion and electrode combination, the ionic Seebeck effect is made to last significantly longer.

## 4.8 Structure of PEDOT:PSS as a Function of Humidity

The ionic Seebeck effect in PEDOT:PSS is dependent on both the chemical structure and the morphology of the biphasic material. Figure 4.12A depicts the chemical structures of the two materials systems investigated, one being the conventional PEDOT:PSS which has been significantly studied as a thermoelectric conducting polymer in the literature,[96] and the other being PEDOT:PSS with silver polystyrenesulfonate (Ag:PSS). The morphology of PEDOT:PSS is highly debated, and the most commonly used interpretation of the morphology is that of PEDOT-rich disc domains within an insulating PSS-rich matrix,[89] as seen in the morphological schematic Figure 4.12B. The incorporation of Ag:PSS to PEDOT:PSS results in a system that exhibits electrical conductivity along the PEDOT-rich domains and silver ion or proton transport in the percolated PSS-rich regions. PSS is classified as an ionomer and is well-known to exhibit strong humidity dependent properties due to environmental water uptake, and typically exhibit higher ionic conductivities due to the presence of water in the ion conducting domains than that in the dry state.[269] Water uptake in the PSS domains should result in significant swelling, increasing the spacing between PEDOT discs (L), and changing the electrical and ionic conductivity of the material; therefore, it is imperative to accurately control the humidity and de-convolute the electronic conductivity and ionic conductivity to assess the role of ionic conductivity to the overall Seebeck coefficient.

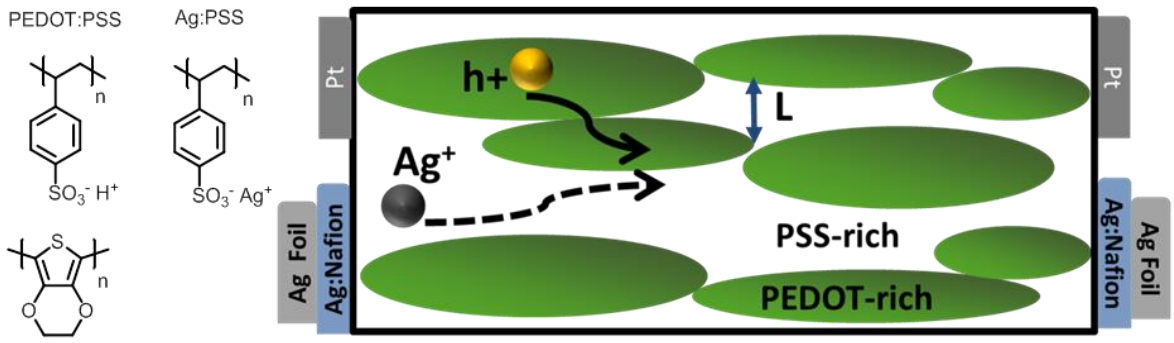


**Figure 4.12:** The chemical structures of PEDOT:PSS and Ag:PSS are presented. These materials have the morphology of a mixed conductor, with $Ag^+$ ions transported by the PSS rich domains and hole transport in the PEDOT rich regions. Electrical conductivity was measured by using ion blocking Pt contacts, and Ag:Nafion/Ag foil contacts were used to measure ionic conductivity in PEDOT:Ag:PSS, while Nafion/Ag:Nafion/Ag foil was used to measure ionic conductivity in PEDOT:PSS. L, the distance between PEDOT rich domains, would increase with humidity due to water swelling the PSS-rich regions.

## 4.9 Thermoelectric Behavior of Mixed Conductors

As seen in the literature and in Figure 4.13, the ionic thermoelectric voltage decays rapidly in an exponential manner,[268] and is due to ion motion results in ionic Seebeck coefficients much larger than the electronic Seebeck coefficient.[88] Figure 4.13 shows the voltage drop and current passing through a two kΩ resistor generated by a 3μm thick film of PEDOT:PSS (green) or PEDOT:Ag:PSS (black) under different temperature gradients at a constant RH=100%. The experiment is divided into five segments of thirty minutes each; the first segment the mixed conductor film experiences ΔT=0 K, the second segment ΔT = 1 K, the third segment ΔT = 0 K, the fourth segment ΔT = 3.5 K, and the final segment ΔT = 0 K. The trend in the decay of the thermoelectric voltage with PEDOT:PSS is clear; the thermoelectric voltage and current from the ionic Seebeck effect decays exponentially over the thirty minute segment, and the residual voltage and current baseline is solely due to the electronic contribution due to PEDOT:PSS; the same phenomenon has observed by Wang *et al*. in PEDOT:PSS.[268]

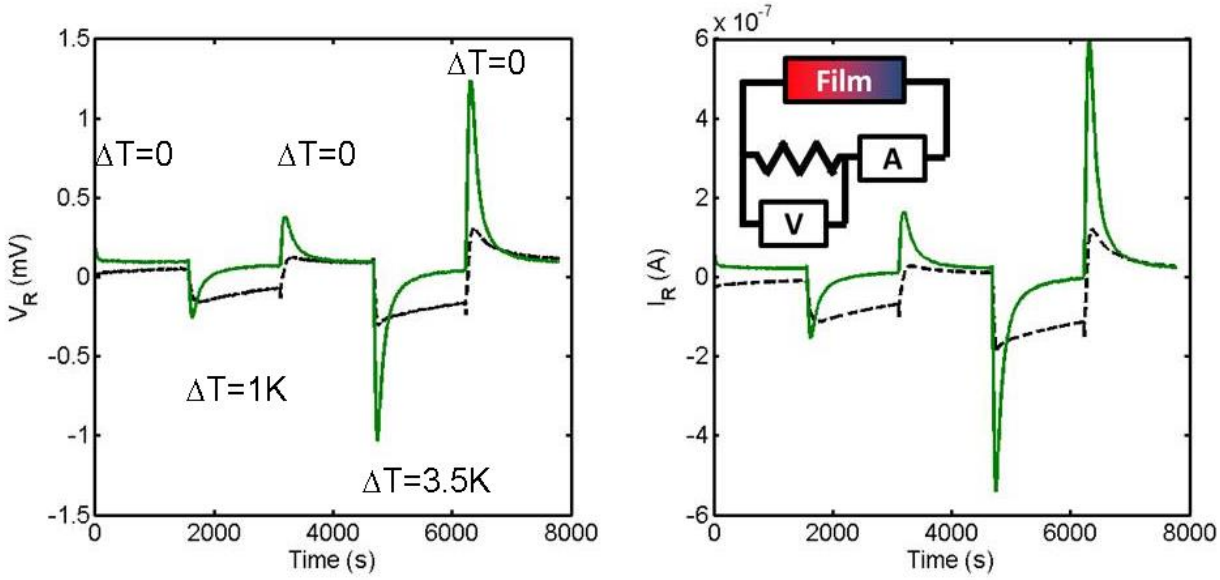


**Figure 4.13:** (Left) Temperature gradient applied to PEDOT:PSS and PEDOT:Ag:PSS 3 μm drop-coated films on glass. Thermoelectric voltage from PEDOT:PSS (green) and PEDOT:Ag:PSS (black) across a 2 kOhm resistor. Upon relaxation of the temperature gradient a symmetric, opposite voltage is observed as the ion flux is reversed. (Right,inset) : Circuit demonstrating measurement of thermoelectric voltage and current generated through a 2 kΩ resistor. (Right, outset) Thermoelectric current through the resistor as measured through the circuit displayed. PEDOT:Ag:PSS demonstrates a lower maximum thermoelectric voltage, but is much more time stable compared to PEDOT:PSS which quickly decays exponentially.

It is also observed that upon relaxation of the temperature gradient in PEDOT:PSS, a symmetric voltage and current due to relaxation of both charge carrier concentrations is produced. As can be seen in Figure 4.14 which is PEDOT:PSS at a relative humidity of 20%, solely electronic conductors do not experience exponential decay or reversed thermoelectric voltage upon temperature relaxation. This observation where the relaxation of the ionic gradient will lead to a measureable, near-symmetric thermoelectric voltage strongly implies that it is the flux of ions from hot to cold that results in the measured voltage, and that the exponential decay in the thermoelectric voltage is due to motion of holes under the thermoelectric voltage. Upon relaxation of the temperature gradient, the flux of ions and holes down their respective concentration gradients results in the reversed thermoelectric voltage signal.

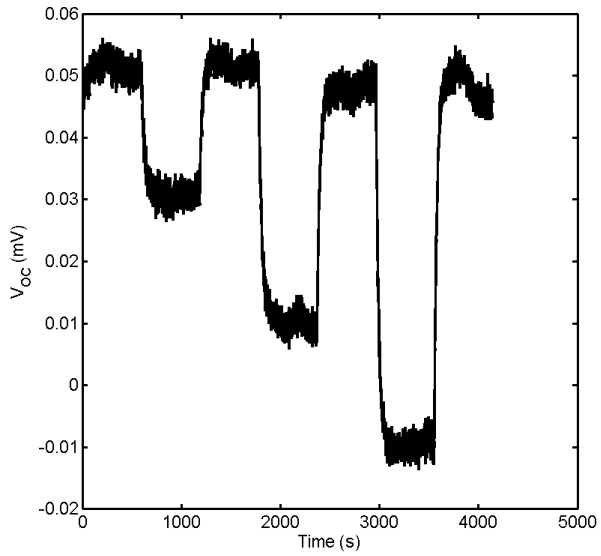


**Figure 4.14:** PEDOT:PSS measured at RH=20% in the open circuit condition. The temperature profile applied was as follows: $\Delta T = 0K$, $\Delta T = 1K$, $\Delta T = 0K$, $\Delta T = 2.5K$, $\Delta T = 0K$, $\Delta T = 3.5K$, $\Delta T = 0K$

In the measurement setup, the voltage was measured across a resistor in order to make sure that the baseline did not shift. This shifting baseline is observed in Figure 4.15, where at zero applied temperature gradient a change in the baseline is observed. The origins of this baseline changing over time are unclear, but by adding a resistor in series to the film and measuring the thermoelectric voltage produced by the film across the resistor, we can have data with a flat baseline. One hypothesis for the shifting baseline is the presence of a background chemical reaction or if the ions were not given enough time to fully equilibrate across the film. However, neither of these explanations can justify why the addition of a resistor would lead to a flattening of the baseline.

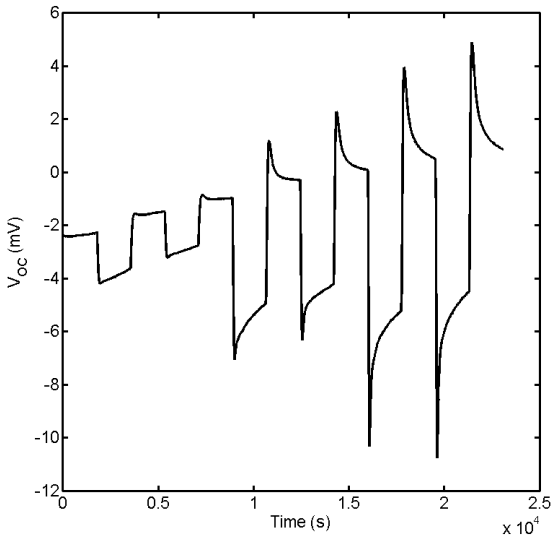


**Figure 4.15:** PEDOT:PSS Open circuit thermoelectric measurement at RH=100%. Temperature profile applied as follows: ΔT = 0K, ΔT = 1K, ΔT = 0K, ΔT = 1K, ΔT = 0K, ΔT = 2.5K, ΔT = 0K, ΔT = 2.5K, ΔT = 0K, ΔT = 3.5K, ΔT = 0K, ΔT = 3.5K, ΔT = 0K. Note the shifting baseline in comparison to Figure 4.14, where the addition of a resistor in series leads to a flat baseline.

## 4.10 Transport Equations for Mixed Conductor Thermoelectrics

The transient thermoelectric voltage due to ionic motion in PEDOT:PSS can be modeled using fundamental charged particle transport equations and scaling relations. The flux (*J*) of a charged ion with charge $z_1q$ within the temperature gradient is due to the concentration gradient, temperature gradient and electric field as shown in Equation 4.8.

$$J = z_1 q D \frac{dc}{dx} - cqD_T \frac{dT}{dx} - \sigma \frac{dV}{dx} \tag{4.8}$$

Where *D* is the mass diffusion coefficient; $D_T$ is the thermal diffusion coefficient, and σ the electrical conductivity. The thermal diffusion coefficient is intrinsically related to the Soret effect, leading to concentration gradient of molecules when under a temperature gradient. In the steady state when net flux is zero, the resulting thermoelectric voltage is related to the carrier concentration, the thermal diffusion coefficient, the diffusion coefficient and the electrical conductivity. An extension of Equation 4.8 can be directly applied to model a system of two different, equivalently charged particles as seen in Equation 4.9, where the two carriers experience the same temperature gradient and electric field.

$$J = z_1 q D_1 \frac{dc_1}{dx} + z_2 q D_2 \frac{dc_2}{dx} - \left(c_1 z_1 q D_{1,T} + c_2 z_2 q D_{T,2}\right) \frac{dT}{dx} - (\sigma_1 + \sigma_2) \frac{dV}{dx} \tag{4.9}$$

Now, by analyzing this equation in the case where the temperature gradient is zero (dT/dx = 0) and flux is zero, a relationship can be written between the concentration gradients of the two species, and the electric field in the system. Of importance is the relative diffusion coefficients of the two carriers.

$$\frac{dV}{dx} = \frac{z_1 q D_1}{\sigma_1 + \sigma_2}\frac{dc_1}{dx} + \frac{z_2 q D_2}{\sigma_1 + \sigma_2}\frac{dc_2}{dx} \tag{4.10}$$

The first scenario is when the ionic species does not undergo a chemical reaction at the electrode, such as with protons and gold or silver electrodes at voltages lower than the redox potential. The ionic species will be denoted as species 1 and species 2 will be the holes in PEDOT:PSS, which are free to enter and leave the system at the electrodes. From kinetic theory, the diffusion coefficient is directly proportional to the conductivity by the relation $\boldsymbol{D = \frac{k_B T}{nq^2}\sigma}$. By substituting into Equation 4.10, we find that the species transference number, which is the ratio of the conductivity of each species over the summation of both carrier conductivities, is extremely important to determining which carrier contributes most to flux under an electric field. It is noted that in PEDOT:PSS or PEDOT:Ag:PSS the ratio of ionic conductivity to electrical conductivity is 0.01 and 0.1 respectively at the highest relative humidity conditions. Therefore, from the previous equations that model the thermoelectric behavior of these mixed conductors, there should be four key experimental observations. First, ions and electrons are expected to migrate under a temperature gradient, resulting in a voltage gradient. If the ions do not participate in an electrochemical reaction, there will also be a concentration gradient of ions. Secondly, charge carriers will then move under the thermoelectric voltage, with the extent of motion governed by the transference number of each carrier, setting up a concentration gradient to oppose the internal electric field. This will manifest as a peak in the thermoelectric voltage over time, followed by a relaxation process and decay. Thirdly, once the temperature gradient is released, both concentration gradients of ions and holes will return to equilibrium, which will result in a symmetric peak in the thermoelectric voltage. Lastly, we expect that in a system with electrodes that allow an electrical reaction there will be a reduced ion concentration gradient due to electrochemistry at the electrodes, resulting in a constant flux of ions from hot to cold. This is the underlying design rationale with PEDOT:Ag:PSS and silver electrodes, as the silver is free to move and react at the silver electrodes.

As demonstrated in Figure 4.13, the addition of Ag:PSS and silver electrodes result in a significantly prolonged in time ionic Seebeck effect, since the PEDOT:Ag:PSS system with silver electrodes is a mixed conductor where silver ions are free to enter and exit the system through the silver electrodes. The presence of a chemical reaction allows generation and consumption of silver ions. The ionic Seebeck effect will be constituted from two sources: the entropy of the chemical reaction and the thermodiffusion of ions seen in Equation 4.11.[133]

$$S = \frac{\Delta S}{nF} + \frac{F}{\sigma T} z c D_T \tag{4.11}$$

A reverse, symmetric spike in the thermoelectric voltage is not expected upon relaxation of the temperature gradient, as there are no ion concentration gradients being formed, and holes are consumed at the silver electrodes to generate silver ions that thermodiffuse. However, as there are still protons in the film, there should be a residual effect from the proton concentration gradient. Therefore, in order to observe a constant enhanced thermoelectric voltage from the ionic Seebeck effect, it would be necessary to design a material system that minimizes the accumulation and depletion of ions due to the thermal gradient, and allows a constant flux of ions from hot to cold. This is achieved through the addition of Ag:PSS and silver electrodes; silver ions are free to move within the PSS domains, and the electrodes function as a constant source and sink of silver. This is depicted in Figure 4.13, where the ionic Seebeck voltage and current no longer has the same exponential behavior or symmetric thermoelectric voltage upon removal of the temperature gradient as observed in PEDOT:PSS. Indeed, over a time period of thirty minutes, the thermoelectric current and voltage produced by PEDOT:Ag:PSS drop by 35% and are linear in behavior compared to PEDOT:PSS which has the ionic Seebeck effect fully decay within minutes. However, PEDOT:Ag:PSS still has residual mobile protons due to the PSS incorporated from the starting PEDOT:PSS dispersion, and results in a residual proton ionic thermoelectric voltage, which can be seen in Figure 4.13. Although PEDOT:Ag:PSS has a lower conductivity than PEDOT:PSS, the overall Seebeck coefficient over time is much higher, resulting in an stable ion enhanced power factor, higher thermoelectric voltages and currents. The same experiment can be performed on Ag:PSS, a purely ionic conducting system with matching silver electrodes, and demonstrates that the purely ionic system has significantly lower thermoelectric voltage and current that PEDOT:Ag:PSS. Therefore, the thermoelectric performance of Ag:PSS is enhanced by PEDOT:PSS, while the ionic Seebeck effect from Ag:PSS is retained in PEDOT:Ag:PSS. Future experiments with PEDOT:PSS and palladium/hydrogen electrodes will elucidate if the ionic enhancement over long time periods can be extended to PEDOT:PSS, which should function in a similar manner to PEDOT:Ag:PSS. However, implementation of said system as a working thermoelectric material would be of significant challenge compared to PEDOT:Ag:PSS with silver electrodes.

The diffusion of the holes over time caused the thermoelectric voltage built by the ionic Seebeck effect ($V_{ion}$) can be modeled to first-approximation by Fick's second law, and from Equation 4.8 it follows that a concentration gradient of charge carriers is directly related to the thermoelectric voltage. Equation 5 models the experimental transient thermoelectric voltages well, which is derived from Fick's second law and Equation 4.9.

$$V = V_{ion}e^{-\lambda_{ion}D_{ion}t} + V_{ion}e^{\lambda_{h+}D_{h+}t} \quad [4.12]$$

$\lambda_{h+}$ is determined from the boundary conditions and geometry of the film, while $D_{h+}$ is the diffusion coefficient of holes in PEDOT. The transient thermoelectric voltage and the corresponding exponential decay coefficient for PEDOT:PSS in Figure 4.13 will correspond to the diffusion coefficient of holes in PEDOT:PSS calculated using the relation $D = \frac{k_B T}{nq^2}\sigma$. The

diffusion coefficient for holes extracted from Figure 4.13 is 0.116 $cm^2/s$, and can be converted to a conductivity of 0.296 S/cm, using a carrier concentration of $10^{20}$ $cm^{-3}$. This closely matches the experimental conductivity measured in Figure 4.13. On removal of the temperature gradient, the reverse, near-symmetric thermoelectric voltage measured is caused by both holes and ions returning to the equilibrium states. This can be modeled by Equation 4.12, where holes and ions diffuse in opposite directions due to the previously established concentration gradients. The calculated ion diffusion coefficient is 0.01148 $cm^2/s$. Using a carrier concentration of $10^{19}$ $cm^{-3}$ calculated from the molar density of HPSS, we calculate a proton conductivity of 0.005 S/cm, which is close to the measured ion conductivity in Figure 4.16.

## 4.11 Humidity Controls Power Factor in Mixed Conductors

An experimental investigation of the difference in conductivity between ion and hole as a function of humidity is shown in Figure 4.16. The measurement of the electrical conductivity and ionic conductivity were decoupled by using electron blocking electrodes and ion blocking electrodes as described by Shetzline *et al*., and can be seen in Figure 4.12.[269] Silver Nafion and Nafion membranes are important to block electron flow through PEDOT:PSS, and the silver Nafion/silver foil interface allow extraction of ion charge carriers. The entire setup was run in a humidity controlled potentiostat setup, and experimental details are described in the methods section. Figure 4.16 is the humidity controlled electronic (circles) and ionic (square) conductivity of PEDOT:PSS (green) and PEDOT:Ag:PSS (black). By increasing the humidity that the mixed conductor is exposed to, the electronic conductivity decreases in both systems, which is attributed to the swelling of the insulating PSS domains in the polymer morphology. This effect is observed to saturate at a relative humidity of 75% for PEDOT:PSS and 82% for PEDOT:Ag:PSS. While the electrical conductivity decreases by a factor of 2.8 and 3.3 for PEDOT:PSS and PEDOT:Ag:PSS, the overall electrical conductivity remains high at 0.15 and 0.01 S/cm at RH=100%, respectively. Ionic conductivity in these two mixed conductors shows an increasing trend with humidity, with evidence of a plateau in ionic conductivity in PEDOT:PSS at 75% relative humidity, and no clear plateau for PEDOT:Ag:PSS. While ionic conductivity typically scales exponentially with water uptake and humidity in pure ion conductors,[252] the ion conductivity measured in these two systems increases with humidity.

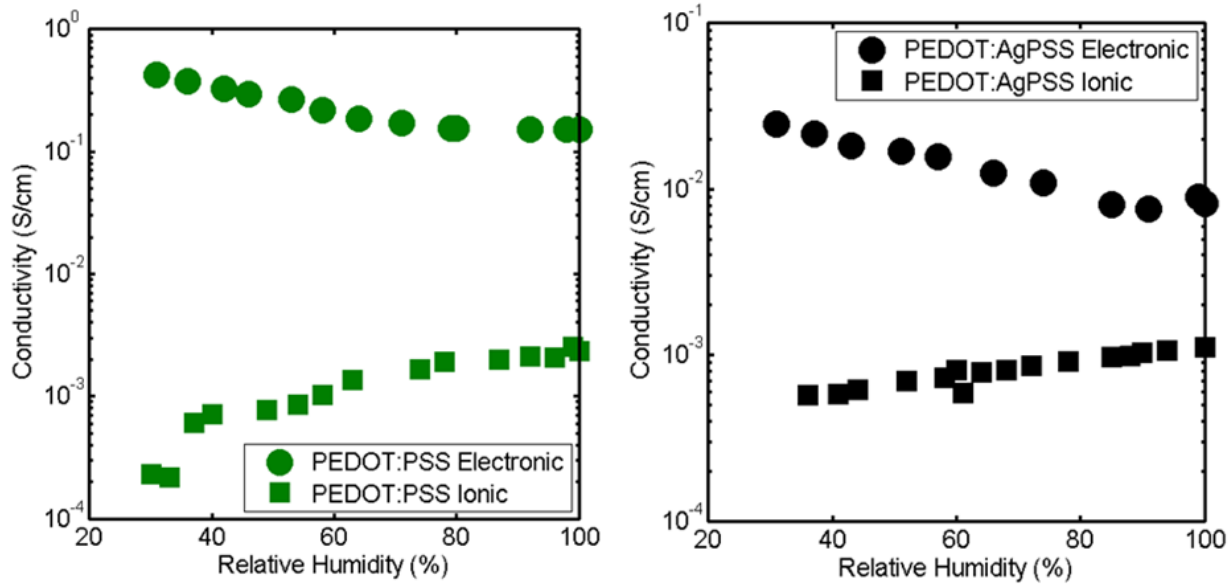


**Figure 4.16:** Electrical conductivity (circle) and ionic conductivity (square) of PEDOT:PSS (green) and PEDOT:Ag:PSS (black) is measured as a function of humidity. As humidity increases, the electrical conductivity decreases due to an increase in L, and the ionic conductivity increases due to water uptake facilitating ion transport. The electron conductivity of PEDOT:Ag:PSS is reduced by nearly one order of magnitude compared to PEDOT:PSS due to the addition of the insulating Ag:PSS. The ratio of the conductivity of ions and holes are extremely important to the transient ionic Seebeck effect. Isolation of ion-electronic contributions via the use of blocking electrodes demonstrates that the ionic contribution to conduction is an order of magnitude less than the electronic counterpart.

Measurements of the Seebeck coefficient of PEDOT:PSS and PEDOT:Ag:PSS were then performed at controlled relative humidity conditions to further investigate the mechanism leading to ionic Seebeck coefficients. The results are depicted in Figure 4.17A, where the Seebeck coefficients of PEDOT:PSS and PEDOT:Ag:PSS were calculated using the peak thermoelectric voltage in the open circuit condition before the exponential decay is observed and the sloped baseline observed. As the Seebeck coefficient in Figure 4.17A is plotted on a logarithmic scale, the increase in Seebeck coefficient is exponential with regards to relative humidity in both PEDOT:PSS and PEDOT:Ag:PSS. The maximum Seebeck coefficient of PEDOT:Ag:PSS is almost an order of magnitude smaller than PEDOT:PSS at the highest relative humidity, but much more stable over time, which is not reflected in Figure 4.17A. The ionic Seebeck effect can only be observed at a threshold relative humidity of 60%, below this threshold both materials show purely electronic Seebeck coefficients of 18 μV/K for PEDOT:PSS and 8 μV/K for PEDOT:Ag:PSS. At a relative humidity of 100%, the maximum observed Seebeck coefficient for PEDOT:PSS is 2.4 mV/K, and 0.10 mV/K for PEDOT:Ag:PSS. The electronic conductivity of PEDOT:Ag:PSS is expected to be lower since the addition of

Ag:PSS, an electrically insulating material, results in a decrease of electron mobility through the material.

## 4.12 Thermal Conductivity and Degradation of Mixed Conductors

Finally, investigation of the thermal conductivity of PEDOT:Ag:PSS is important since the material now contains silver. Time-domain thermoreflectance (TDTR) method has been used to measure thermal conductivity of PEDOT:Ag:PSS thin film, as shown in Figure 4.17C. The thermal conductivity of ≈0.24 W/(m K) demonstrates that even with the addition of silver ions to the polymer, the thermal conductivity is unchanged from PEDOT:PSS (≈0.3 W/(m K)).[94] The incorporation of Ag:PSS into PEDOT:PSS does not significantly enhance the thermal conductivity. The thermal conductivity is phonon-dominated as the electrical conductivity of these materials are not high enough to see a significant contribution due to the Wiedemann-Franz law, nor is there a percolated silver network.

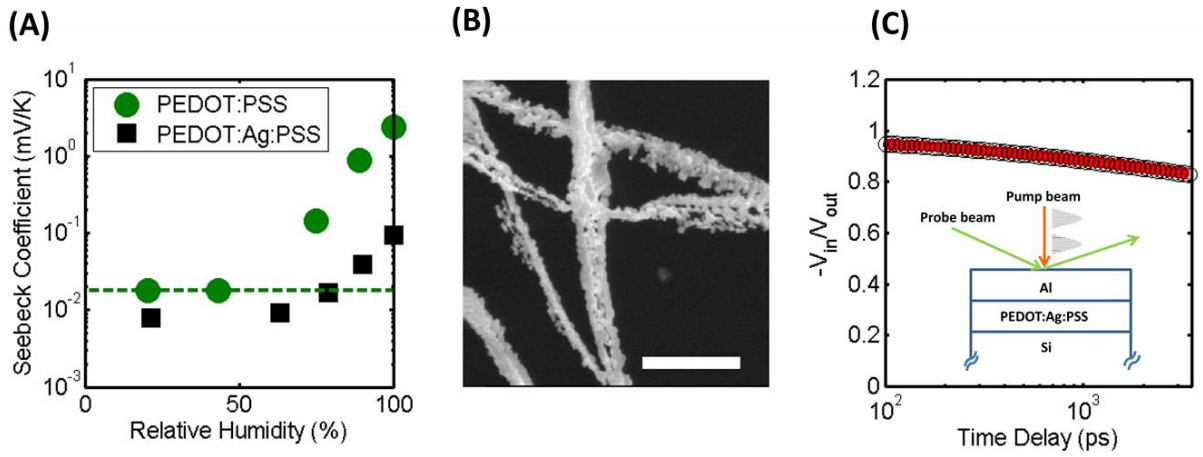


**Figure 4.17:** (A) Humidity dependent Seebeck measurement of PEDOT:PSS (green circles) and PEDOT:Ag:PSS (black squares) show an exponential increase in the Seebeck coefficient due to the ion motion above a threshold of RH=60%. The Seebeck coefficient is calculated by using the maximum observed thermoelectric voltage observed before decay is observed. (B) High current flow through PEDOT:Ag:PSS results in silver microwire formation. The precipitation of silver is hypothesized to be the cause of PEDOT:Ag:PSS performance decreasing over operation. Scale bar = 500 nm (C) Thermal conductivity measurement of PEDOT:Ag:PSS via time-domain thermoreflectance method(the inset figure shows the schematics of this method and sample configuration) results in a phonon dominated thermal conductivity of 0.24 W/(m K). The measurement data (open circle) and the best-fit (red-line) for measuring a ≈50-nm thick PEDOT:Ag:PSS thin film.

It should be noted that when PEDOT:Ag:PSS is subjected to a high current at above the humidity threshold, silver is observed to migrate from one electrode to the other resulting in silver formation on the electrodes as seen in Figure 4.18, and silver microwires are observed to form at the polymer/electrode interface (Figure 4.17B). The formation of silver microwires are hypothesized to be the reason that PEDOT:Ag:PSS performance degrades by 35% at long times. TEM images in Figure 4.19 show the prescence of silver clusters throughout the polymer at lengthscales less than 20 nm. It remains to be seen how this structure changes with humidity.

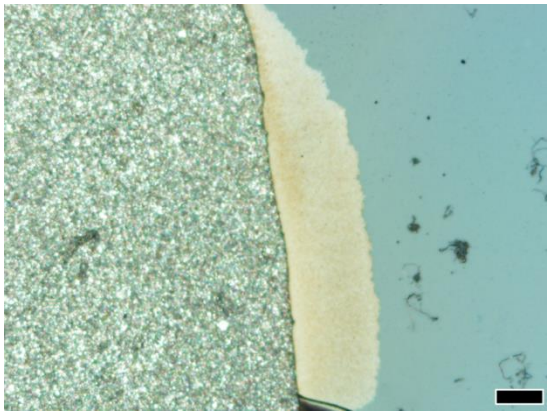

**Figure 4.18:** Silver growth on painted silver electrode on PEDOT:Ag:PSS during thermoelectric operation. Black bar = 100 μm.

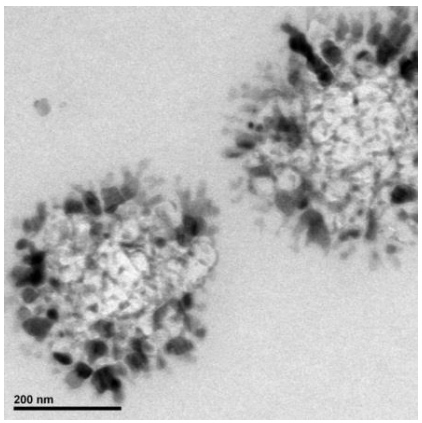


**Figure 4.19:** TEM images of PEDOT:Ag:PSS dehydrated spun coat films on silicon nitride windows. The morphology upon hydration is of great future interest. The dark regions are silver-rich, and the light regions are polymer-rich.

## 4.13 Concluding Remarks on Thermoelectric Mixed Conductors

PEDOT:Ag:PSS was synthesized, and the electrical conductivity (0.01 S/cm) and thermoelectric properties (S = 0.1 mV/K) were characterized as a function of humidity. The electrical conductivity trends with relative humidity oppose the ionic conductivity trends in both PEDOT:PSS and PEDOT:Ag:PSS, and is explained through understanding the polymer morphology. The ionic Seebeck effect is observed to occur at a certain threshold relative humidity greater than 60%. PEDOT:Ag:PSS displays a lower Seebeck coefficient and electrical conductivity than PEDOT:PSS with humidity; however, the ion enhanced thermoelectric current and voltage is observed to be much more stable than that observed with PEDOT:PSS over time. A symmetric thermoelectric voltage signal upon relaxation of the temperature difference is observed, and it is reasoned that the ionic Seebeck effect is dependent on ion flux. The fundamental underpinnings of thermoelectric mixed conductors are discussed. The stability in the thermoelectric voltage and current observed in PEDOT:Ag:PSS is caused by constant silver ion flux from the hot silver electrode to the cold silver electrode. Upon a high current flow through the material, silver microwire formation is observed in the material, which may be the cause of degradation in material performance. The thermal conductivity of PEDOT:Ag:PSS is measured to be 0.24 W/(m K), which is unchanged from the pristine PEDOT:PSS. Through the careful selection of electrodes and ionic species, the thermoelectric performance of pristine PEDOT:PSS can be improved with an ionic Seebeck effect that is stable over time, while retaining the material properties that make PEDOT:PSS an attractive thermoelectric material.

We would like to conclude by proposing that if the electrical conductivity of PEDOT:Ag:PSS can be improved to the values observed for PEDOT:PSS treated with ethylene glycol or DMSO and the ionic Seebeck effect can be preserved,[268] extremely high figure of merits will be observed, with ZT greater or equal to 1 possible. Future work along these avenues is on-going, as preliminary experiments of PEDOT:Ag:PSS treated with DMSO exhibit only electrical conductivity with no ionic conductivity, as also observed in similar systems by Wang *et al*.[268] This could be hypothesized to be a result of the DMSO treatment breaking the percolation of the PSS network, resulting in much diminished ionic conductivity.[89]

## 4.14 Experimental Methods

Nafion 117, polystyrenesulfonic acid (18 wt% in water), and silver nitrate were purchased from Sigma Aldrich. Silver hydroxide (AgOH) was synthesized via the following steps: 4.22 g (25 mmol) of $AgNO_3$ was dissolved in 3 mL of deionized water, and was mixed into a centrifudge vial containing 1g of NaOH in 3 mL of deionized water. The brown solid precipitate was then centrifuged with the supernatant discarded, a total of three times. The AgOH product was then dried at 70°C in a vacuum oven to remove water. Ag-Nafion was prepared with 200 µl of Nafion 117 solution (5wt% in mixed aliphatic alcohols) was added to 800 µL of deionized water with either 1.12 mg of AgOH or 1.53 mg of $AgNO_3$ for 1:1 silver to sulfonate molar ratio solutions. Ag-PSS was prepared with 40 µL of 18 wt% polystyrenesulfonic acid in water added to 1 mL of deionized water with either 4.3 mg of AgOH or 5.7 mg of $AgNO_3$ for 1:1 silver to sulfonate molar ratio solutions. The Ag-Nafion and Ag-PSS solutions were covered in foil and stirred overnight. Additional purification through dialysis was performed; however, material properties did not vary significantly pre-dialysis to post-dialysis. Films were cast on 1x1 $cm^2$ glass substrates, washed in water with detergent, deionized water, and isopropyl alcohol. 50 µL of Ag-Nafion and Ag-PSS were drop-cast on glass or silicon substrates on a 50°C hot plate and covered. Films were characterized using X-ray photoelectron spectroscopy to determine the silver content to sulfonate content using a Kratos Axis Ultra X-ray Photoelectron Spectroscopy system.

DC electrical conductivity was performed using the Van der Pauw method using two Keithley 2400 multimeters and by voltage-current sweeps up to 100 mV. Film thickness measurements were performed using a Dektak profilometer. Seebeck coefficient measurements were made using two Peltier units to generate a temperature gradient, and a Keithley 2100 voltmeter to measure the thermoelectric voltage. Two type K thermocouples were used to monitor the temperature drop across the film. 100 nm silver electrodes were evaporated using an Angstrom thermal evaporator, or silver paint was applied for electrodes. One thousand data points were collected at each temperature interval, and a wait time of 180 seconds was sufficient to maintain a stable temperature gradient. AC impedance was performed on the same sample and geometry as Seebeck measurement, using a Biologic VSP-300.

Modules were fabricated by drop-casting films on stiff glass microscope slides or a flexible Kapton membrane on paper. Testing of the module was accomplished by placing the module between two 40 mm x 40 mm Peltier heaters, which were capable of applying stable temperature differences of 3 K. The terminal legs of the module were connected electrically in series to a Keithley 2400 multimeter and a 100 Ω resistor, and the voltage drop across the resistor was monitored by a Keithley 2100 voltmeter. Silver paint was applied to wire the device

electrically in series, with the silver paint also functioning as the necessary silver electrode for the thermogalvanic reaction. Stainless steel probes are used to connect the device to copper wires linked to the measurement setup, which has a known Seebeck coefficient of 5 μV/K.

We used time-domain thermoreflectance (TDTR) method to measure thermal conductivity of all the samples. Prior to the TDTR measurements, Al thin films were deposited on the samples by magnetron sputtering. TDTR is a well-established method to measure thermal properties of thin film materials.[1] We used a modulation frequency *f*=9.2 MHz, with a *1/e*$^2$ radius of the focused laser beams of $w_0 = 11.7\ \mu$m . For each sample, we fit the TDTR ratio data[1] to extract the thermal conductivity of the polymer thin films. In the fitting model, the heat capacities of Al and Si are adopted from literature values.[2,3] The thickness of Al thin film was obtained from picosecond acoustics using a longitudinal speed of sound 6.42 nm/ps.[4] The thickness of the polymer films was measured by atomic force microscope (AFM). The thermal conductivity of the Al thin film was calculated using the WFL and the electrical resistance of the same transducer layer deposited on a ≈315 nm $SiO_2$ on Si reference sample. Density of the polymer films were determined by measuring the mass and volume of the material. The measured density is as follows: Nafion: 1.8 g/cm^3, Ag-Nafion: 1.7 g/cm^3, Ag-PSS: 1.27 g/cm^3. Specific heat capacity was measured using Perkin Elmer DSC 8000. The specific heat were measured to be the following: Nafion: 1.89 J/cm3 K, Ag-Nafion: 1.95 J/cm3 K, Ag-PSS: 1.7 J/g k. We set the interface thermal conductance between Al and polymer thin film $G_1$, and interfacial thermal conductance between polymer thin film and Si substrate $G_2$, as 100 MW/m$^2$K. The sensitivity of the data analysis to the interfacial thermal conductance is small when the thermal conductivity Λ is low. As shown in figure 20,[5] the ratio data are much less sensitive to *G* in comparison to Λ over the range of thermal conductivities ( $0.2 < \Lambda < 0.5$ W m$^{-1}$ K$^{-1}$ ). The error bars of the TDTR measurements can be obtained by taking into account the individual uncertainties and sensitivities of the parameters in the thermal model.[1] The thermal conductivity of Nafion was measured to be 0.20 W/mK, Ag-Nafion to be 0.22 W/mK, and Ag-PSS to be 0.40 W/mK. The error bars on these measurements are 10%.

Ag:PSS was prepared with 40 μL of 18 wt% polystyrenesulfonic acid in water purchased from Sigma Aldrich added to 1 mL of deionized water with 5.7 mg of AgNO3 for 1:1 silver to sulfonate molar ratio solutions. The Ag:PSS solutions were covered in foil and stirred over-night. PEDOT:Ag:PSS was made by adding 25 μl of a 10 mg/ml solution Ag:PSS to 50 μl of PEDOT:PSS (Clevios PH1000, Lot 2014P0344), and casting on a 1 cm$^2$ glass substrate at 50 °C. Silver electrodes were thermally evaporated or painted using silver paint. SEM and EDS was performed on the FEI XL40 Sirion FEG Digital SEM. Electrical conductivity was measured using platinum electrodes and running a cyclic voltammetry sweep on a Biologic VSP300 at 0.1 mV/sec to a peak voltage of +/- 1mV,[269] and checked by four point Van de Pauw measurements on gold electrodes using two Keithley 2400s. Film thickness was measured using a Dektak

profilometer. Ionic conductivity was measured by a specialized cell which allows an electrode stack of film, Nafion (Ag/H) and silver foil to block out electronic contributions. The humidity chamber was custom built, using dry compressed air flowed through two water bubblers to achieve saturation. Humidity was equilibrated for 15 to 30 minutes before measurement. Seebeck coefficient measurements were conducted using two Peltier heaters in the humidity chamber with two thermocouples. The voltage was measured with a Keithley 2010.

The time-domain thermoreflectance (TDTR) method was used to measure thermal conductivity of PEDOT:Ag:PSS thin film samples. Details of TDTR methods can be found elsewhere.[1] Prior to the TDTR measurements, ≈80nm-thick Al thin films were deposited on the samples by magnetron sputtering. We used a modulation frequency *f*=9.2 MHz, with a $1/e^2$ radius of the focused laser beams of $w_0 = 11.7\ \mu\text{m}$. For each sample, we fit the TDTR ratio data[1] with thermal diffusion model to extract the thermal conductivity of the polymer thin films. In the fitting model, the heat capacities of Al and Si are adopted from literature values.[2,3] The thickness of Al thin film was obtained from picosecond acoustics using a longitudinal speed of sound 6.42 nm/ps.[4] The thickness of the polymer films was measured by atomic force microscope (AFM). The thermal conductivity of the Al thin film was calculated using the WFL and the electrical resistance of the same transducer layer deposited on a ≈315 nm $SiO_2$ on Si reference sample. Density of the polymer films were determined by measuring the mass and volume of the material. Specific heat capacity was measured using Perkin Elmer DSC 8000. We set the interface thermal conductance between Al and polymer thin film $G_1$, and interfacial thermal conductance between polymer thin film and Si substrate $G_2$, as 100 MW//$m^2$K. The sensitivity of the data analysis to the interfacial thermal conductance is small when the thermal conductivity $\Lambda$ is low. The error bars of the TDTR measurements can be obtained by taking into account the individual uncertainties and sensitivities of the parameters in the thermal model.[1] The thermal conductivity of ≈50 nm thick PEDOT:Ag:PSS thin film was measured to be $0.24 \pm 0.02$ W/mK.

## 4.15 The Thermoelectric AFM Technique

In this section, we will discuss the design principles behind thermoelectric AFM, along with the use of thermoelectric AFM to understand the morphological changes behind PEDOT:PSS upon addition of DMSO. In conjunction with NT-MDT Research, a thermoelectric AFM hybrid mode has been developed to give thermoelectric voltage scans along with adhesion and height images. The hybrid mode means that on a single pass, the AFM tip is gathering simultaneous height, thermovoltage, surface adhesion and phase information. No other AFM technique has been developed that can give insight into all these properties concurrently. Microprobe techniques in the literature have limited microscale scan resolutions.[234–236,270–273] Thermoelectric scans are typically used to investigate differences in doping densities, along with inhomogeneities in the crystal structure which may strongly affect the thermoelectric performance.[235,270] Previous scanning Seebeck work done by Snyder looks at compositional and doping fluctuations due to heterogeneities in inorganics, with a larger length scale.[235,236,274]

Within the morphology of conducting polymers, there are the crystalline and amorphous phases, which typically have significantly different carrier mobility.[275,85,90] In PEDOT:PSS, not only is the material a composite with insulating PSS regions, but upon the addition of DMSO it is hypothesized that the morphology changes immensely.[276,84,86]Here, we attempt to use thermoelectric scans to give insight into the conjugated polymer morphology of PEDOT:PSS, and with the addition of DMSO, attempt to decipher why the addition of high boiling point solvents such as DMF, DMSO and EG can result in a film that is three orders of magnitude more conductive than pristine PEDOT:PSS.[91] From our results, it is clear that the addition of DMSO homogenizes the morphology of PEDOT:PSS, reducing PSS rich domains, improving thermoelectric performance.

A schematic of the thermoelectric AFM is shown in Figure 4.20, and comprises the most important parameters within the scanning Seebeck. The substrate is typically silicon or sapphire, both materials with high thermal conductivity. A thin film of PEDOT:PSS is drop-coated onto the substrate, and is then placed on a PID controlled heater under the AFM head. The laser diode is brought into alignment with the AFM tip, which in this study was an NTMDT NSG01. This specific tip is coated in conductive platinum iridium, which is very necessary for robustness sake since the tip spends much of the time in contact with the surface. The tip has a tip radius below 30 nanometers, a resonant frequency at approximately 160 kHz and a force constant of 5 N/m. A temperature gradient is established between the tip and the substrate, since the tip is thermally in contact with a thermal sink that is at room temperature. A gold wire is then used to connect the voltage pre-amplifier in the cantilever holder to the tip. The AFM tip first makes contact with the substrate with a certain force dictated by the force constant and the deflection of the tip. The

thermoelectric voltage is then measured. The tip is then removed from the surface with a certain set displacement, and the adhesion force and phase of the material is recorded upon withdrawal. The entire image is then rastered to produce simultaneous height, thermoelectric, adhesion force and phase scans.

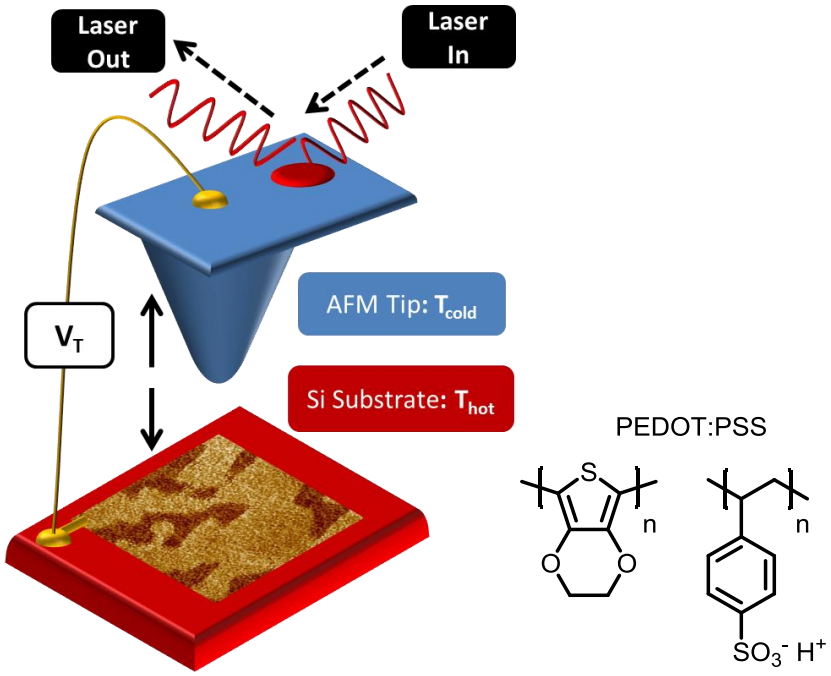


**Figure 4.20:** (Left) Schematic of the AFM setup enabling height, adhesion and thermoelectric imaging. The substrate is a heated 1 $cm^2$ silicon wafer with a 1 um thick PEDOT:PSS drop-casted film electrically connected by a gold wire. The AFM tip is kept at room temperature through a thermal sink, and brought repeated in and out of contact with the film in a raster pattern. The thermoelectric voltage, height and adhesion force is measured at each point. (Right) Chemical structure of PEDOT:PSS, with the proposed morphology seen in Figure 4.12.

## 4.16 Thermoelectric Scans on PEDOT:PSS

Figure 4.21 demonstrates the ability for simultaneous height, adhesion and thermoelectric voltage scans with the NT-MDT system on PEDOT:PSS with no DMSO treatment. First of all, from the height images it is clear that there are 100 nm oval shaped aggregates filled with polymer that shows a higher height that the aggregates. This is confirmed in the adhesion force images, which demonstrate that the particular nature of PEDOT shows fused semicircles of these aggregates, since the adhesion images can distinguish between the PEDOT-rich domains and the PSS-rich domains. However, it is difficult to ascertain from the height and adhesion images

which region corresponds to the PEDOT-rich domains and vice-versa. To solve this issue, we turn to the thermoelectric scans. From the thermoelectric scans, we find that under 25% of the scan is dark brown, and the rest show a high thermoelectric voltage. Since we know that the Seebeck coefficient of PEDOT:PSS without DMSO treatment is near 30 uV/K and the temperature gradient is 65ºC, the dark regions are the PEDOT-rich domains that are highly electrically conducting, and the light regions are PSS-rich insulating domains, which dominate at nearly a 3:1 ratio to the PEDOT domains.[96] This is very much in line with the composition of PEDOT:PSS PH1000 when purchased from Clevios, where PSS is 75 wt% of the dispersion. We note that there are many regions that are not connected the percolated PEDOT:PSS network. We find these results corroborate the prevalent opinion on the morphology of PEDOT:PSS, which is that PEDOT is encapsulated in PSS aggregates, which are oval shaped.[275,91,277] These aggregates are believed to be fused with less PSS on the exterior with the addition of DMSO.

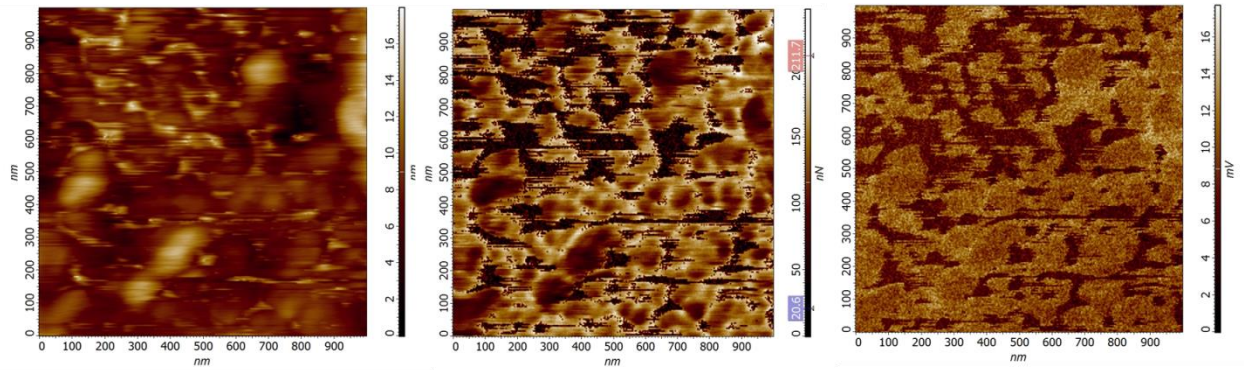

**Figure 4.21:** Simultaneous height (a), adhesion (b), and thermoelectric voltage (c) at 65 ºC of PEDOT:PSS with no DMSO treatment. All scans clearly demonstrate the biphasic nature of PEDOT:PSS. The thermoelectric scans allow identification of the two phases. The dark regions in the adhesion image and thermoelectric voltage image are the PEDOT-rich percolated network, and the light regions are the PSS-rich domains. Manipulation of these two domains and interfaces are key to developing PEDOT:PSS as a thermoelectric material.

To test these theories, we perform thermoelectric scans on PEDOT:PSS and compared to films treated with DMSO. These results are displayed in Figure 4.22, where the top row corresponds to PEDOT:PSS and the bottom row corresponds to PEDOT:PSS treated with DMSO. One can easily see that the surface of PEDOT:PSS without DMSO is fairly rough, with micron sized aggregates present throughout the 7 um scan size. The overall roughness of the topography is strongly reduced upon addition of DMSO. The thermoelectric scans tell a similar story; the aggregates observed in the height scan have a high Seebeck coefficient and are expected to be more resistive than the majority of the film. Upon addition of DMSO, the overall thermoelectric scans are much more uniform, except the presence of one aggregate. This is evidence that upon addition of DMSO, the PSS aggregates are broken up, and the overall film becomes more uniform, thus improving electrical conductivity by improve carrier mobility.

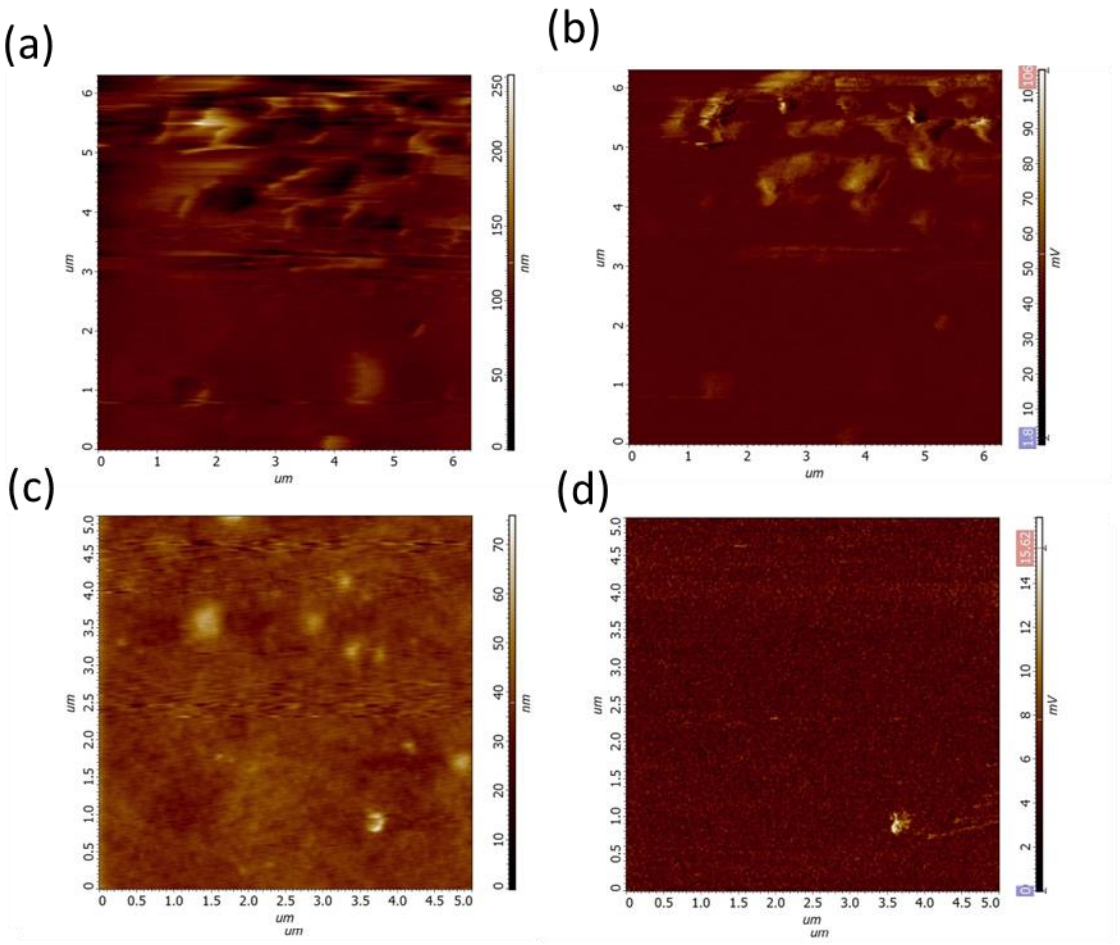


**Figure 4.22:** PEDOT:PSS height (a) and thermoelectric scans (b) compared to PEDOT:PSS with 5% DMSO height (c) and thermoelectric scans (d) at 55ºC. Images reveal large sub-micron inhomogeneities in PEDOT:PSS that are detrimental to the thermoelectric performance, and are identified to be PSS-rich aggregates. The addition of 5% DMSO to the casting solvent results in a more uniform film, with significantly reduced PSS aggregates. One of the strengths of thermoelectric imaging is the ability to distinguish which phases enhance and inhibit the thermoelectric performance.

By taking different thermoelectric scans at different substrate temperature intervals, the Seebeck coefficient of the film can be ascertained. Since the temperature drop is primarily in a dome shape structure through the film as calculated in Figure 4.25, the Seebeck coefficient that is measured will be a mixture of the in-plane Seebeck coefficient and thru-plane Seebeck coefficient. Figure 4.23 plots out the relationship between the average thermoelectric voltage of PEDOT:PSS treated with DMSO and the temperature gradient between the tip and film, and we find it to be very linear. We find that the Seebeck coefficient of PEDOT:PSS with DMSO is 26

uV/K. Since these two values for the Seebeck coefficient has been measured for PEDOT:PSS, we find that there is good agreement between the value measured via thermoelectric AFM scans and literature values.[96]

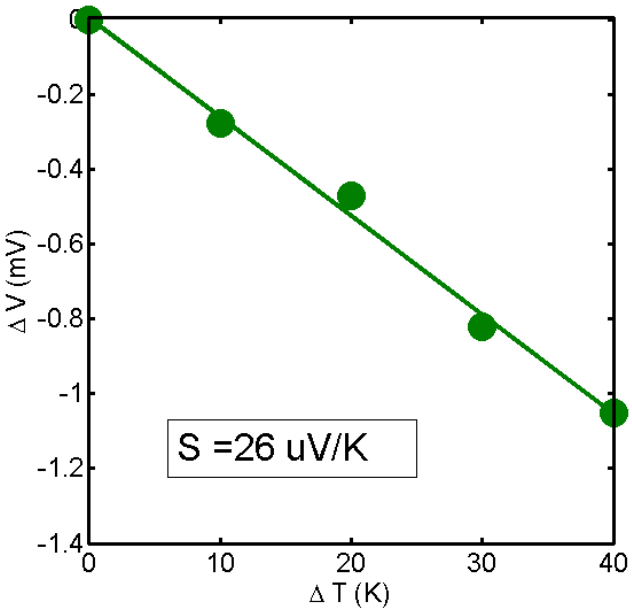


**Figure 4.23:** Thermoelectric voltage versus temperature gradient for PEDOT:PSS with DMSO measured by thermoelectric AFM. The scanning Seebeck technique shows a Seebeck coefficient of 26 uV/K, which is very close to the literature measurement.

## 4.17 Theoretical and Experimental Limits of Scanning Seebeck

To further characterize the scanning Seebeck technique, we turn to an inorganic system, bismuth tin. Bismuth tin, when mixed correctly, forms a low-melting eutectic alloy which phase separates into two regions: a bismuth rich region that is p-type, and a tin region that is n-type.[278,279] Figure 4.24 illustrates height and thermoelectric scans of a 6 um scan size of BiSn. The thermoelectric scans are done at a substrate temperature of 65 ºC, and demonstrate that indeed, there are two contrasting regions, the p-type region and the n-type region. This has become the standard sample to test thermoelectric imaging on, as it is fully characterized and has enhanced contrast due to differences between p-type and n-type regions, magnifying the difference in the Seebeck coefficient of the two domains.

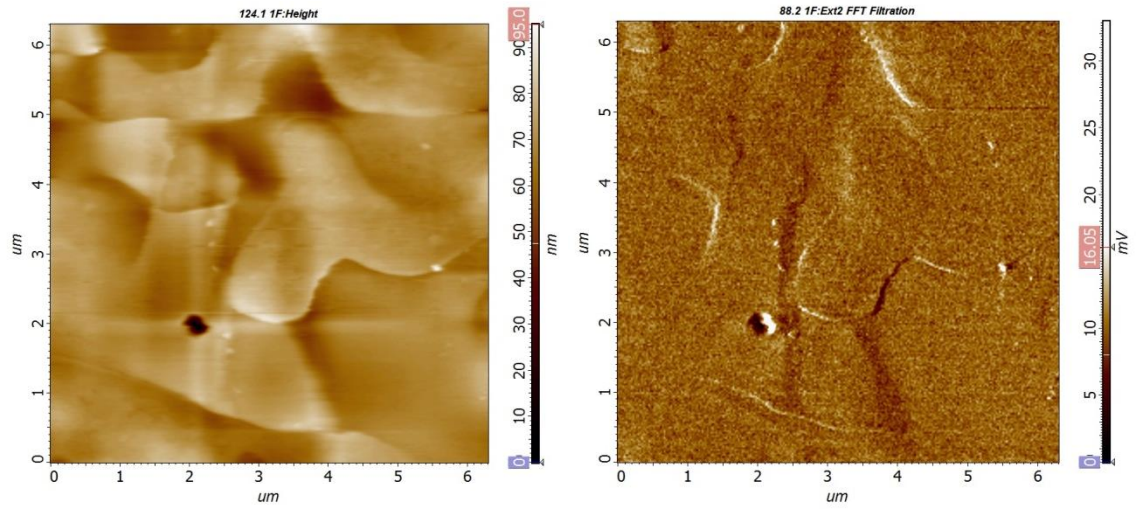


**Figure 4.24:** (Left) Height and (right) thermoelectric scans on a 6 um scan size of BiSn at 65 ºC. BiSn has become the standard substrate to perform thermoelectric imaging on, since BiSn forms a low-melting eutectic that phase separates into a Bi-rich domain that has a positive Seebeck coefficient and a Sn-rich domain that has a negative Seebeck coefficient. This phase separation occurs on the micron length scale and leads to enhanced contrast in the thermoelectric images, which can be corroborated to the height map.

Lastly, the resolution of the thermoelectric imaging is discussed using theoretical finite element modeling with COMSOL, and the results are displayed in Figure 4.25. The extent of the heat spreading on the AFM tip limits the resolution of the thermoelectric scan, and with a tip radius of 40 nanometers, we see that a majority of the temperature drop occurs within 10-20 nanometers of the edge of the tip, similar to that seen in other heat transfer nanoscale measurements.[227] The penetration depth of the heat drop is dome shaped in nature, so that the thermoelectric voltage measured is equally due to the in-plane Seebeck coefficient and the in-plane Seebeck coefficient. The modeling was done with the assumption that the thermal conductivity of the tip was greater than 100 W/mK, and the thermal conductivity of the polymer film was low at 0.5 W/mK. If the substrate has a higher thermal conductivity, we would expect larger heat-spreading and decreased imaging resolution.

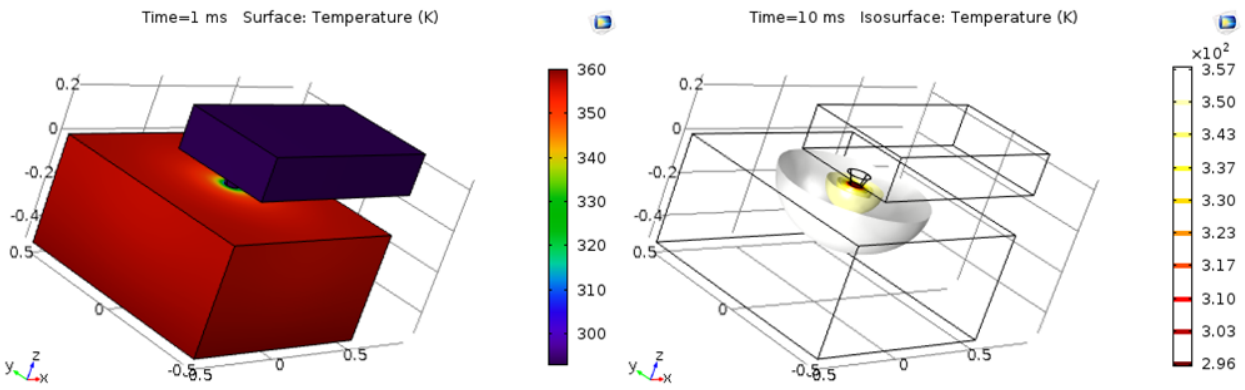


**Figure 4.25:** Finite element model of the temperature drop at the AFM tip/film contact. The temperature drop is responsible for the thermoelectric voltage observed, and is related to the special resolution of probe in thermoelectric imaging. The model shows that most of the temperature drop is concentrated within the tip diameter of 40 nm, and so the thermoelectric scans cannot resolve features lower than the diameter of the tip sufficiently well. Since the thermal conductivity of the tip is much higher than the thermal conductivity of the polymer film, and the tip is thermally connected to a heat sink, the temperature drop is mostly through the polymer film upon contact.

## 4.18 Concluding Remarks on the Scanning Seebeck Technique

In conclusion, we find that thermoelectric AFM can be used to examine how the morphology of PEDOT:PSS changes the thermoelectric performance of the overall film. We find that the morphology of PEDOT:PSS is quite interesting, and that a combination of information from height, adhesion and thermoelectric scans are necessary to discern the PEDOT-rich domains from the PSS-rich domains. We find that upon application of DMSO, there is a substantial drop in the number of aggregates that are highly resistive, leading to better film quality. A decrease in PSS aggregation is observed, which improves percolation of PEDOT domains. By taking thermoelectric scans over different temperature intervals, the Seebeck coefficient of PEDOT:PSS was also measured, and it was found to be very close to literature values. Thermoelectric scans of the model system BiSn was also used to fully characterize the system. Finally, finite element modeling of the thermoelectric AFM tip and substrate was used to determine the temperature drop across the tip junction. These results show that with a sharp tip radius of less than 30 nanometers, a thermoelectric imaging resolution of approximately 40 nanometers is achievable, resulting in orders of magnitude improvements over conventional microprobe scanning Seebeck setups, pushing resolutions in the nanoscale.

## 4.19 Acknowledgements

We gratefully acknowledge support from the Air Force Office of Science Research for this work (No. MURI FA9550-12-1-0002). Scanning Seebeck research and development was performed at NT-MDT Research. Thermal conductivity measurements were performed by Dr. Jun Liu at University of Illinois, Urbana-Champaign.

# Chapter 5: Conclusion and Remarks on the Future of Transport in Organic-Inorganic Thermoelectrics

To conclude, we demonstrate that decoupling thermoelectric transport can be achieved in many different systems ranging from molecular junctions to gold nanocrystal arrays to ion transport in polymers. Each of these systems hold great promise by breaking the conventional inverse correlation of the Seebeck coefficient to the electrical conductivity inherent to normal three dimensional electronic band structure. However, each of these systems still require further optimization and materials development in order to achieve thermoelectric power factors close to that observed for current state of the art thermoelectrics.

From the chapter discussion on molecular junctions measured via the STM-break junction technique, we come to the conclusion that further increases in the power factor must come from the incorporation of different binding groups that form covalent bonds with the metal, to further minimize the energy gap between the molecular orbital energy to the metal Fermi energy. From our work, we have designed the best candidates in terms of length and electron richness; however, we did not experimentally observe a very large increase in the thermoelectric power factor. Future work should investigate similar molecules but with trimethyl tin binding groups and with metals that have higher Fermi energies than gold, such as silver. It is unknown whether trimethyl tin binding groups will also result in the same binding with silver as it does with gold. From our investigation into the molecular energy levels with UPS, we find that the best aligned molecule has a HOMO energy 0.54 eV away from the Fermi level of gold. However, our theoretical calculations show that this value needs to be ~5 $k_bT$ to see truly large enhancements in the power factor, given the molecule-electrode coupling observed with alkylthiols. By using spectroscopic techniques to assess where the distance between the Fermi energy and the HOMO energy is, proper screening of molecules can be performed before length experimental measurements.

Our work on gold nanocrystal arrays demonstrate the suitability of using solid-state ligand exchanged films as a platform for scaled molecular junctions. However, as conductive AFM and thermoelectric scans demonstrate, the overall performance of these materials is dependent on extent of ligand exchange and defects throughout the film. We predict that with solid-state ligand exchange, while a fast and effective method to replace oleylamine with conductive ligands, results in too many film defects for optimal thermoelectric power factors. Bi-

phasic solution ligand exchanges, followed by optimizing film processing conditions, should result in higher performing arrays. An electrical conductivity of 1000 S/cm is a good metric to determine whether a material has potential as a thermoelectric device. Secondly, with the vast library of molecular junctions, many potential molecules are widely available for testing. Specifically, future investigation on the role of molecules with HOMO and LUMO levels well aligned to the nanocrystal Fermi energy should result in increased power factors. We have shown that the thermal conductivity of gold nanocrystal arrays with alkanethiol ligands is comparable to polymers, although it remains to be seen if stiff conjugated molecular ligands also have the same low thermal conductivity.

Polymer thermoelectrics have much room to grow as thermoelectric materials, and may soon settle into a niche market as flexible, wearable thermoelectrics. Since we observed early on that PEDOT:PSS can easily achieve an electrical conductivity of 1000 S/cm, it is clear that improvements to the Seebeck coefficient were necessary for improvements to the power factor. To address this, we study polymers that conduct only ions, in order to uncover whether ion transport can be a legitimate method to enhance the Seebeck coefficient. We find that the thermoelectric behavior of ion conductors is well-described by the Newman analysis of thermoelectric and thermogalvanics. We find that ion conductors have too low intrinsic ion conductivity to achieve a high figure of merit. To address this, we investigated mixed conductors, in the hope that the high Seebeck coefficient of the ions and the high electrical conductivity could result in a material with high thermoelectric performance. With PEDOT:Ag:PSS we found a material that has a high Seebeck coefficient and an electrical conductivity orders of magnitude higher than the ionic conductivity. This system has a power factor close to that of PEDOT:PSS treated with DMSO. Future work should investigate methods to further enhance the electrical conductivity of mixed conductors, with the final goal of achieving materials with figure of merits higher than 1.

We also discussed the implementation of a thermoelectric AFM developed in conjunction with NT-MDT, that has the ability to probe the thermoelectric response of 50 nanometer domains within the diverse morphology of conductive polymers. By concurrently acquiring the height, adhesion, phase and thermoelectric information of the material in a single scan, any sort of topological change in the material, along with structural mechanical response can be correlated to thermoelectric performance. We predict that this instrument will be of great use in future investigations of composite thermoelectric systems, ranging from conjugated polyelectrolyte carbon nanotube systems, to inorganic-organic hybrids such as PEDOT with tellurium nanowires.

Throughout this work, we have emphasized the need for understanding the electron transport through monomer subunits at the nanoscale to formulate design rules for better thermoelectrics. Our journey has taken us from the single molecule scale, where molecular junction transport has been leveraged into materials that have a positively correlated Seebeck coefficient and electrical conductivity. We have demonstrated how the organic –inorganic

interface between polymers and mobile ions have resulted in materials with extremely high Seebeck coefficients and great potential as flexible thermogalvanic materials. We hope that we have demonstrated the need for understanding the fundamental physical picture behind each thermoelectric material discussed, and that there is still a need to further optimize and improve the thermoelectric performance of these materials.

## References


(1) Tritt, T.; Subramanian, M. *MRS Bull.* **2006**, *31*.

(2) Snyder, G. J.; Toberer, E. S. *Nat. Mater.* **2008**, *7*, 105–114.

(3) Heremans, J. P.; Dresselhaus, M. S.; Bell, L. E.; Morelli, D. T. *Nat. Nanotechnol.* **2013**, *8*, 471–473.

(4) Wang, H.; Pei, Y.; Lalonde, A. D.; Snyder, G. J. *Thermoelectric Nanomaterials*; Koumoto, K.; Mori, T., Eds.; Springer Series in Materials Science; Springer Berlin Heidelberg: Berlin, Heidelberg, 2013; Vol. 182.

(5) Chen, C.-L.; Wang, H.; Chen, Y.-Y.; Day, T.; Snyder, G. J. *J. Mater. Chem. A* **2014**, *2*, 11171–11176.

(6) Lan, Y.; Poudel, B.; Ma, Y.; Wang, D.; Dresselhaus, M. S.; Chen, G.; Ren, Z. *Nano Lett.* **2009**, *9*, 1419–1422.

(7) Dresselhaus, M. S.; Chen, G.; Tang, M. Y.; Yang, R.; Lee, H.; Wang, D.; Ren, Z.; Fleurial, J. P.; Gogna, P. *Adv. Mater.* **2007**, *19*, 1043–1053.

(8) Tao, N. J. *Nano Lett.* **2004**, *4*, 267–271.

(9) Büttiker, M.; Imry, Y.; Landauer, R.; Pinhas, S. *Phys. Rev. B* **1985**, *31*, 6207–6215.

(10) Paulsson, M.; Datta, S. *Phys. Rev. B* **2003**, *67*, 241403.

(11) Yee, S. K.; Malen, J. a; Majumdar, A.; Segalman, R. a. *Nano Lett.* **2011**, *11*, 4089–4094.

(12) Reddy, P.; Jang, S.-Y.; Segalman, R. a; Majumdar, A. *Science* **2007**, *315*, 1568–1571.

(13) Cheng, Z.-L.; Skouta, R.; Vazquez, H.; Widawsky, J. R.; Schneebeli, S.; Chen, W.; Hybertsen, M. S.; Breslow, R.; Venkataraman, L. *Nat. Nanotechnol.* **2011**, *6*, 353–357.

(14) Kim, K.; Liu, J.; Namboothiry, M. A. G.; Carroll, D. L. *Appl. Phys. Lett.* **2007**, *90*.

(15) Stalder, R.; Mei, J.; Reynolds, J. R. *Macromolecules* **2010**, *43*, 8348–8352.

(16) Ku, S. Y.; Brady, M. A.; Treat, N. D.; Cochran, J. E.; Robb, M. J.; Kramer, E. J.; Chabinyc, M. L.; Hawker, C. J. *J. Am. Chem. Soc.* **2012**, *134*, 16040–16046.

(17) Li, J.; Dierschke, F.; Wu, J.; Grimsdale, A. C.; Müllen, K. Poly(2,7-carbazole) and perylene tetracarboxydiimide: a promising donor/acceptor pair for polymer solar cells. *Journal of Materials Chemistry*, 2006, *16*, 96.

(18) McNeill, C. R.; Abrusci, A.; Zaumseil, J.; Wilson, R.; McKiernan, M. J.; Burroughes, J. H.; Halls, J. J. M.; Greenham, N. C.; Friend, R. H. *Appl. Phys. Lett.* **2007**, *90*.

(19) Lin, L.; Morisaki, Y.; Chujo, Y. *Int. J. Polym. Sci.* **2010**, *2010*.

(20) Wang, M.; Hu, X.; Liu, P.; Li, W.; Gong, X.; Huang, F.; Cao, Y. *J. Am. Chem. Soc.* **2011**, *133*, 9638–9641.

(21) Li, W.; Roelofs, W. S. C.; Turbiez, M.; Wienk, M. M.; Janssen, R. a J. *Adv. Mater.* **2014**, *26*, 3304–3309.

(22) Sendur, M.; Balan, A.; Baran, D.; Karabay, B.; Toppare, L. *Org. Electron. physics, Mater. Appl.* **2010**, *11*, 1877–1885.

(23) Cravino, A.; Zerza, G.; Maggini, M.; Bucella, S.; Svensson, M.; Andersson, M. R.; Neugebauer, H.; Brabec, C. J.; Sariciftci, N. S. *Monatshefte fur Chemie* **2003**, *134*, 519–527.

(24) Yu, G.; Heeger, A. J. *J. Appl. Phys.* **1995**, *78*, 4510–4515.

(25) Wang, J.; Higashihara, T. *Polym. Chem.* **2013**, *4*, 5518–5526.

(26) Tada, K.; Hosoda, K.; Hirohata, M.; Hidayat, R.; Kawai, T.; Onoda, M.; Teraguchi, M.; Masuda, T.; Zakhidov, A. A.; Yoshino, K. Donor polymer (PAT6) — acceptor polymer (CNPPV) fractal network photocells. *Synthetic Metals*, 1997, *85*, 1305–1306.

(27) Griffini, G.; Douglas, J. D.; Piliego, C.; Holcombe, T. W.; Turri, S.; Fréchet, J. M. J.; Mynar, J. L. *Adv. Mater.* **2011**, *23*, 1660–1664.

(28) Kronemeijer, A. J.; Gili, E.; Shahid, M.; Rivnay, J.; Salleo, A.; Heeney, M.; Sirringhaus, H. *Adv. Mater.* **2012**, *24*, 1558–1565.

(29) Yu, G.; Gao, J.; Hummelen, J. C.; Wudl, F.; Heeger, A. J. Polymer Photovoltaic Cells: Enhanced Efficiencies via a Network of Internal Donor-Acceptor Heterojunctions. *Science*, 1995, *270*, 1789–1791.

(30) Xu, B.; Wu, X.; Li, H.; Tong, H.; Wang, L. *Macromolecules* **2011**, *44*, 5089–5092.

(31) Fang, Z.; Eshbaugh, A. A.; Schanze, K. S. *J. Am. Chem. Soc.* **2011**, *133*, 3063–3069.

(32) Kumar, A.; Pace, G.; Bakulin, A. a.; Fang, J.; Ho, P. K. H.; Huck, W. T. S.; Friend, R. H.; Greenham, N. C. *Energy Environ. Sci.* **2013**, *6*, 1589.

(33) Van Mullekom, H. A. M.; Vekemans, J. A. J. M.; Havinga, E. E.; Meijer, E. W. *Mater. Sci. Eng. R Reports* **2001**, *32*, 1–40.

(34) Zhang, Q.; Cirpan, A.; Russell, T. P.; Emrick, T. *Macromolecules* **2009**, *42*, 1079–1082.

(35) Facchetti, A. Polymer donor-polymer acceptor (all-polymer) solar cells. *Materials Today*, 2013, *16*, 123–132.

(36) Frost, J. M.; Cheynis, F.; Tuladhar, S. M.; Nelson, J. *Nano Lett.* **2006**, *6*, 1674–1681.

(37) Wang, D. H.; Kim, D. Y.; Choi, K. W.; Seo, J. H.; Im, S. H.; Park, J. H.; Park, O. O.; Heeger, A. J. *Angew. Chem. Int. Ed. Engl.* **2011**, *50*, 5519–5523.

(38) Malen, J. a; Doak, P.; Baheti, K.; Tilley, T. D.; Majumdar, A.; Segalman, R. a. *Nano Lett.* **2009**, *9*, 3406–3412.

(39) Fagas, G.; Greer, J. C. *Nanotechnology* **2007**, *18*, 424010.

(40) Jalili, S.; Pangh, A. *Int. J. Mod. Phys. B* **2009**, *23*, 5657–5669.

(41) Tao, N. *Phys. Rev. Lett.* **1996**, *76*, 4066–4069.

(42) Qu, L.; Peng, X. *J. Am. Chem. Soc.* **2002**, *124*, 2049–2055.

(43) Pradhan, N.; Reifsnyder, D.; Xie, R.; Aldana, J.; Peng, X. *J. Am. Chem. Soc.* **2007**, *129*, 9500–9509.

(44) Leff, D. V; Brandt, L.; Heath, J. R. *Langmuir* **1996**, *12*, 4723–4730.

(45) Hinterwirth, H.; Kappel, S.; Waitz, T.; Prohaska, T.; Lindner, W.; Lämmerhofer, M. *ACS Nano* **2013**, *7*, 1129–1136.

(46) Kjellgren, J.; Sundén, H.; Szabó, K. J. *J. Am. Chem. Soc.* **2004**, *126*, 474–475.

(47) Bealing, C. R.; Baumgardner, W. J.; Choi, J. J.; Hanrath, T.; Hennig, R. G. *ACS Nano* **2012**, *6*, 2118–2127.

(48) Bian, K.; Choi, J. J.; Kaushik, A.; Clancy, P.; Smilgies, D. M.; Hanrath, T. *ACS Nano* **2011**, *5*, 2815–2823.

(49) Chemseddine, A.; Moritz, T. *Eur. J. Inorg. Chem.* **1999**, *1999*, 235–245.

(50) Kovalenko, M. V.; Bodnarchuk, M. I.; Lechner, R. T.; Hesser, G.; Schäffler, F.; Heiss, W. *J. Am. Chem. Soc.* **2007**, *129*, 6352–6353.

(51) Puntes, V. F.; Krishnan, K. M.; Alivisatos, A. P. *Science* **2001**, *291*, 2115–2117.

(52) Salant, A.; Shalom, M.; Tachan, Z.; Buhbut, S.; Zaban, A.; Banin, U. *Nano Lett.* **2012**, *12*, 2095–2100.

(53) Xia, Y.; Xiong, Y.; Lim, B.; Skrabalak, S. E. Shape-controlled synthesis of metal nanocrystals: Simple chemistry meets complex physics? *Angewandte Chemie - International Edition*, 2009, *48*, 60–103.

(54) Yin, Y.; Alivisatos, A. P. *Nature* **2005**, *437*, 664–670.

(55) Zhong, H.; Scholes, G. D. *J. Am. Chem. Soc.* **2009**, *131*, 9170–9171.

(56) Jana, N. R.; Chen, Y.; Peng, X. *Chem. Mater.* **2004**, *16*, 3931–3935.

(57) Mentzel, T. S.; Porter, V. J.; Geyer, S.; MacLean, K.; Bawendi, M. G.; Kastner, M. A. *Phys. Rev. B - Condens. Matter Mater. Phys.* **2008**, *77*.

(58) Hinterwirth, H.; Kappel, S.; Waitz, T.; Prohaska, T.; Lindner, W.; Lämmerhofer, M. *ACS Nano* **2013**, *7*, 1129–1136.

(59) Ghosh, S. K.; Nath, S.; Kundu, S.; Esumi, K.; Pal, T. *J. Phys. Chem. B* **2004**, *108*, 13963–13971.

(60) Smith, D. K.; Korgel, B. a. *Langmuir* **2008**, *24*, 644–649.

(61) Prasad, B. L. V; Sorensen, C. M.; Klabunde, K. J. *Chem. Soc. Rev.* **2008**, *37*, 1871–1883.

(62) Peng, G.; Strange, M.; Thygesen, K. S.; Mavrikakis, M. *J. Phys. Chem. C* **2009**, *113*, 20967–20973.

(63) Woehrle, G. H.; Brown, L. O.; Hutchison, J. E. *J. Am. Chem. Soc.* **2005**, *127*, 2172–2183.

(64) Dong, A.; Ye, X.; Chen, J.; Kang, Y.; Gordon, T.; Kikkawa, J. M.; Murray, C. B. *J. Am. Chem. Soc.* **2011**, *133*, 998–1006.

(65) Dubois, F.; Mahler, B.; Dubertret, B.; Doris, E.; Mioskowski, C. *J. Am. Chem. Soc.* **2007**, *129*, 482–483.

(66) Von Holt, B.; Kudera, S.; Weiss, A.; Schrader, T. E.; Manna, L.; Parak, W. J.; Braun, M. Ligand exchange of CdSe nanocrystals probed by optical spectroscopy in the visible and mid-IR. *Journal of Materials Chemistry*, 2008, *18*, 2728.

(67) Webber, D. H.; Brutchey, R. L. *J. Am. Chem. Soc.* **2012**, *134*, 1085–1092.

(68) Caragheorgheopol, A.; Chechik, V. *Phys. Chem. Chem. Phys.* **2008**, *10*, 5029–5041.

(69) Pelaz, B.; Jaber, S.; de Aberasturi, D. J.; Wulf, V.; Aida, T.; de la Fuente, J. M.; Feldmann, J.; Gaub, H. E.; Josephson, L.; Kagan, C. R.; Kotov, N. A.; Liz-Marzán, L. M.; Mattoussi, H.; Mulvaney, P.; Murray, C. B.; Rogach, A. L.; Weiss, P. S.; Willner, I.; Parak, W. J. *ACS Nano* **2012**, *6*, 8468–8483.

(70) Fafarman, A. T.; Koh, W.; Diroll, B. T.; Kim, D. K.; Ko, D.-K.; Oh, S. J.; Ye, X.; Doan-Nguyen, V.; Crump, M. R.; Reifsnyder, D. C.; Murray, C. B.; Kagan, C. R. *J. Am. Chem. Soc.* **2011**, *133*, 15753–15761.

(71) Chen, S.; Zhao, Z.; Liu, H. *Annu. Rev. Phys. Chem.* **2013**, *64*, 221–245.

(72) Cutler, M.; Mott, N. F. *Phys. Rev.* **1969**, *181*.

(73) Mott, N. F. *Philos. Mag.* **1969**, *19*, 835–852.

(74) Fishelson, N.; Shkrob, I.; Lev, O.; Gun, J.; Modestov, A. *Langmuir* **2001**, 403–412.

(75) Tung, R. T. Recent advances in Schottky barrier concepts. *Materials Science and Engineering: R: Reports*, 2001, *35*, 1–138.

(76) Werner, J. H.; Güttler, H. H. *J. Appl. Phys.* **1991**, *69*, 1522–1533.

(77) Tersoff, J. *Phys. Rev. Lett.* **1984**, *52*, 465–468.

(78) Ishii, H.; Sugiyama, K.; Ito, E.; Seki, K. *Adv. Mater.* **1999**, *11*, 605–625.

(79) Klausen, R. S.; Widawsky, J. R.; Steigerwald, M. L.; Venkataraman, L.; Nuckolls, C. *J. Am. Chem. Soc.* **2012**, *134*, 4541–4544.

(80) Grupe, C. *Nat. Nanotechnol.* **2013**, *8*, 385–389.

(81) Shinohara, Y.; Ohara, K.; Imai, Y.; Isoda, Y.; Nakanishi, H. *Proc. ICT'03. 22nd Int. Conf. Thermoelectr. (IEEE Cat. No.03TH8726)* **2003**.

(82) He, M.; Qiu, F.; Lin, Z. *Energy Environ. Sci.* **2013**, *6*, 1352.

(83) Poudel, B.; Hao, Q.; Ma, Y.; Lan, Y.; Minnich, A.; Yu, B.; Yan, X.; Wang, D.; Muto, A.; Vashaee, D.; Chen, X.; Liu, J.; Dresselhaus, M. S.; Chen, G.; Ren, Z. *Science* **2008**, *320*, 634–638.

(84) Nardes, A. M.; Kemerink, M.; Janssen, R. A. J.; Bastiaansen, J. A. M.; Kiggen, N. M. M.; Langeveld, B. M. W.; van Breemen, A. J. J. M.; de Kok, M. M. *Adv. Mater.* **2007**, *19*, 1196–1200.

(85) Na, S.-I.; Wang, G.; Kim, S.-S.; Kim, T.-W.; Oh, S.-H.; Yu, B.-K.; Lee, T.; Kim, D.-Y. *J. Mater. Chem.* **2009**, *19*, 9045–9053.

(86) Timpanaro, S.; Kemerink, M.; Touwslager, F. J.; De Kok, M. M.; Schrader, S. *Chem. Phys. Lett.* **2004**, *394*, 339–343.

(87) Döbbelin, M.; Marcilla, R.; Salsamendi, M.; Pozo-Gonzalo, C.; Carrasco, P. M.; Pomposo, J. A.; Mecerreyes, D. *Chem. Mater.* **2007**, *19*, 2147–2149.

(88) Wei, Q.; Mukaida, M.; Kirihara, K.; Naitoh, Y.; Ishida, T. *Appl. Phys. Express* **2014**, *7*, 3–6.

(89) Timpanaro, S.; Kemerink, M.; Touwslager, F. J.; De Kok, M. M.; Schrader, S. *Chem. Phys. Lett.* **2004**, *394*, 339–343.

(90) Nardes, A. M.; Janssen, R. A. J.; Kemerink, M. *Adv. Funct. Mater.* **2008**, *18*, 865–871.

(91) Jönsson, S. K. M.; Birgerson, J.; Crispin, X.; Greczynski, G.; Osikowicz, W.; Denier van der Gon, A. W.; Salaneck, W. R.; Fahlman, M. *Synth. Met.* **2003**, *139*, 1–10.

(92) Stöcker, T.; Köhler, A.; Moos, R. *J. Polym. Sci. Part B Polym. Phys.* **2012**, *50*, 976–983.

(93) Huang, J.; Miller, P. F.; de Mello, J. C.; de Mello, A. J.; Bradley, D. D. C. *Synth. Met.* **2003**, *139*, 569–572.

(94) Liu, J.; Wang, X.; Li, D.; Coates, N. E.; Segalman, R. A.; Cahill, D. G. *Macromolecules* **2015**, *48*, 585–591.

(95) Schlitz, R. A.; Brunetti, F. G.; Glaudell, A. M.; Miller, P. L.; Brady, M. A.; Takacs, C. J.; Hawker, C. J.; Chabinyc, M. L. *Adv. Mater.* **2014**, *26*, 2825–2830.

(96) Kim, G.-H.; Shao, L.; Zhang, K.; Pipe, K. P. *Nat. Mater.* **2013**, *12*, 719–723.

(97) Russ, B.; Robb, M. J.; Brunetti, F. G.; Miller, P. L.; Perry, E. E.; Patel, S. N.; Ho, V.; Chang, W. B.; Urban, J. J.; Chabinyc, M. L.; Hawker, C. J.; Segalman, R. A. *Adv. Mater.* **2014**, *26*, 3473–3477.

(98) Xuan, Y.; Liu, X.; Desbief, S.; Leclère, P.; Fahlman, M.; Lazzaroni, R.; Berggren, M.; Cornil, J.; Emin, D.; Crispin, X. *Phys. Rev. B - Condens. Matter Mater. Phys.* **2010**, *82*.

(99) Duhm, S.; Xin, Q.; Hosoumi, S.; Fukagawa, H.; Sato, K.; Ueno, N.; Kera, S. *Adv. Mater.* **2012**, *24*, 901–905.

(100) Li, L.; Meller, G.; Kosina, H. *Microelectronics J.* **2007**, *38*, 47–51.

(101) Choi, S. H.; Risko, C.; Carmen Ruiz Delgado, M.; Kim, B.; Brédas, J. L.; Daniel Frisbie, C. *J. Am. Chem. Soc.* **2010**, *132*, 4358–4368.

(102) Pai, D.; Yanus, J.; Stolka, M. *J. Phys. Chem.* **1984**, *429*, 4714–4717.

(103) Bässler, H.; Schönherr, G.; Abkowitz, M.; Pai, D. M. *Phys. Rev. B* **1982**, *26*, 3105–3113.

(104) Bedoya-Pinto, A.; Malindretos, J.; Roever, M.; Mai, D. D.; Rizzi, A. *Phys. Rev. B - Condens. Matter Mater. Phys.* **2009**, *80*.

(105) Arkhipov, V. I.; Bässler, H. *J. Non. Cryst. Solids* **1996**, *198-200*, 242–245.

(106) Monroe, D. *Phys. Rev. Lett.* **1985**, *54*, 146–149.

(107) Novikov, S. V. *arXiv* **2013**.

(108) Pfister, G.; Grammatica, S.; Mort, J. *Phys. Rev. Lett.* **1976**, *37*, 1360–1363.

(109) Lu, Q.; Liu, K.; Zhang, H.; Du, Z.; Wang, X.; Wang, F. *ACS Nano* **2009**, *3*, 3861–3868.

(110) Bisquert, J. *J. Phys. Chem. C* **2007**, *111*, 17163–17168.

(111) Qiu, H.; Xu, T.; Wang, Z.; Ren, W.; Nan, H.; Ni, Z.; Chen, Q.; Yuan, S.; Miao, F.; Song, F.; Long, G.; Shi, Y.; Sun, L.; Wang, J.; Wang, X. *Nat. Commun.* **2013**, *4*, 2642.

(112) Movaghar, B.; Grünewald, M.; Pohlmann, B.; Würtz, D.; Schirmacher, W. *J. Stat. Phys.* **1983**, *30*, 315–334.

(113) Lunde, A. M.; Flensberg, K. *J. Phys. Condens. Matter* **2005**, *17*, 3879–3884.

(114) Jonson, M.; Mahan, G. *Phys. Rev. B* **1980**, *21*.

(115) Cutler, M.; Mott, N. *Phys. Rev.* **1969**, *181*.

(116) Mott, N. *J. Phys. C Solid State Phys.* **1987**, *3075*.

(117) Kunets, V. P.; Dias, M. R. S.; Rembert, T.; Ware, M. E.; Mazur, Y. I.; Lopez-Richard, V.; Mantooth, H. A.; Marques, G. E.; Salamo, G. J. *J. Appl. Phys.* **2013**, *113*.

(118) Deskins, N.; Dupuis, M. Electron transport via polaron hopping in bulk TiO2: A density functional theory characterization. *Physical Review B*, 2007, *75*.

(119) Bak, T.; Nowotny, J.; Rekas, M.; Sorrell, C. C. *Ionics (Kiel).* **2004**, *10*.

(120) Singh, V.; Bougher, T. L.; Weathers, A.; Cai, Y.; Bi, K.; Pettes, M. T.; McMenamin, S. a; Lv, W.; Resler, D. P.; Gattuso, T. R.; Altman, D. H.; Sandhage, K. H.; Shi, L.; Henry, A.; Cola, B. a. *Nat. Nanotechnol.* **2014**, *9*, 384–390.

(121) Kim, D.; Kim, Y.; Choi, K.; Grunlan, J. C.; Yu, C. *ACS Nano* **2010**, *4*, 513–523.

(122) Wickramasinghe, H. K. *Acta Mater.* **2000**, *48*, 347–358.

(123) Kwon, H. J.; Osada, Y.; Gong, J. P. Polyelectrolyte Gels-Fundamentals and Applications. *Polymer Journal*, 2006, *38*, 1211–1219.

(124) Ballauff, M.; Borisov, O. Polyelectrolyte brushes. *Current Opinion in Colloid & Interface Science*, 2006, *11*, 316–323.

(125) Ai, S.; Lu, G.; He, Q.; Li, J. *J. Am. Chem. Soc.* **2003**, *125*, 11140–11141.

(126) Allen, F. I.; Comolli, L. R.; Kusoglu, A.; Modestino, M. A.; Minor, A. M.; Weber, A. Z. *ACS Macro Lett.* **2015**, *4*, 1–5.

(127) Kuş, M.; Okur, S. *Sensors Actuators, B Chem.* **2009**, *143*, 177–181.

(128) Ikeshoji, T. *Bull. Chem. Soc. Jpn.* **1987**.

(129) Quickenden, T. I.; Mua, Y. *J. Electrochem. Soc.* **1995**, *142*, 3985–3994.

(130) Sokirko, A. *Electrochim. Act* **1994**, *39*, 597–609.

(131) Weininger, J. L. *J. Electrochem. Soc.* **1964**, *111*, 769.

(132) Burrows, B. *J. Electrochem. Soc.* **1976**, *123*, 154.

(133) Newman, J. *Ind. Eng. Chem. Res.* **1995**, *34*, 3208–3216.

(134) Vennekamp, M.; Janek, J. *Solid State Ionics* **1999**, *118*, 43–66.

(135) Duhr, S.; Braun, D. *Proc. Natl. Acad. Sci. U. S. A.* **2006**, *103*, 19678–19682.

(136) Di Ventra M; Pantelides, S.; Lang, N. *Phys. Rev. Lett.* **2000**, *84*, 979–982.

(137) Di Ventra, M.; Pantelides, S. T.; Lang, N. D. *Appl. Phys. Lett.* **2000**, *76*, 3448.

(138) Dell'Angela, M.; Kladnik, G.; Cossaro, A.; Verdini, A.; Kamenetska, M.; Tamblyn, I.; Quek, S. Y.; Neaton, J. B.; Cvetko, D.; Morgante, A.; Venkataraman, L. *Nano Lett.* **2010**, *10*, 2470–2474.

(139) Reed, M.; Zhou, C.; Muller, C.; Burgin, T.; Tour, J. *Science* **1997**, *278*, 252–254.

(140) Reddy, P.; Jang, S. Y.; Segalman, R. A.; Majumdar, A. *Science.* **2007**, *315*, 1568–1571.

(141) Quinn, J.; Foss, F. *J. Am. Chem. Soc.* **2007**, *129*, 6714–6715.

(142) Xiao, X. Y.; Xu, B. Q.; Tao, N. J. *Nano Lett.* **2004**, *4*, 267–271.

(143) Chen, F.; Hihath, J.; Huang, Z. F.; Li, X. L.; Tao, N. J. *Annu. Rev. Phys. Chem.* **2007**, *58*, 535–564.

(144) Tao, N. J. *J. Mater. Chem.* **2005**, *15*, 3260–3263.

(145) Xu, B. Q.; Tao, N. J. J. *Science.* **2003**, *301*, 1221–1223.

(146) Ahn, S.; Aradhya, S. V; Klausen, R. S.; Capozzi, B.; Roy, X.; Steigerwald, M. L.; Nuckolls, C.; Venkataraman, L. *Phys. Chem. Chem. Phys.* **2012**, *14*, 13841–13845.

(147) Chen, W.; Widawsky, J. *J. Am. Chem. Soc.* **2011**, 17160–17163.

(148) Kamenetska, M.; Quek, S. Y.; Whalley, A. C.; Steigerwald, M. L.; Choi, H. J.; Louie, S. G.; Nuckolls, C.; Hybertsen, M. S.; Neaton, J. B.; Venkataraman, L. *J. Am. Chem. Soc.* **2010**, *132*, 6817–6821.

(149) Kiguchi, M.; Miura, S.; Hara, K.; Sawamura, M.; Murakoshi, K. *Appl. Phys. Lett.* **2006**, *89*.

(150) Lindsay, S. *J. Chem. Educ.* **2005**, *82*, 727–733.

(151) Beebe, J.; Kim, B.; Gadzuk, J.; Daniel Frisbie, C.; Kushmerick, J. *Phys. Rev. Lett.* **2006**, *97*, 026801.

(152) Kiguchi, M.; Murakoshi, K. *J. Phys. Chem. C* **2008**, *112*, 8140–8143.

(153) Schneebeli, S. T.; Kamenetska, M.; Cheng, Z. L.; Skouta, R.; Friesner, R. A.; Venkataraman, L.; Breslow, R. *J. Am. Chem. Soc.* **2011**, *133*, 2136–2139.

(154) Yee, S. K.; Sun, J. B.; Darancet, P.; Tilley, T. D.; Majumdar, A.; Neaton, J. B.; Segalman, R. A. *ACS Nano* **2011**, *5*, 9256–9263.

(155) Malen, J. A.; Yee, S. K.; Majumdar, A.; Segalman, R. A. *Chem. Phys. Lett.* **2010**, *491*, 109–122.

(156) Venkataraman, L.; Park, Y. S.; Whalley, A. C.; Nuckolls, C.; Hybertsen, M. S.; Steigerwald, M. L. *Nano Lett.* **2007**, *7*, 502–506.

(157) Park, Y.; Whalley, A. *J. Am. Chem. Soc.* **2007**, *129*, 15768–15769.

(158) Capozzi, B.; Dell, E. J.; Berkelbach, T. C.; Reichman, D. R.; Venkataraman, L.; Campos, L. M. *J. Am. Chem. Soc.* **2014**, *136*, 10486–10492.

(159) Tsutsui, M.; Taniguchi, M. *Sensors (Basel).* **2012**, *12*, 7259–7298.

(160) Beebe, J. M.; Engelkes, V. B.; Miller, L. L.; Frisbie, C. D. *J. Am. Chem. Soc.* **2002**, *124*, 11268–11269.

(161) Malen, J. A.; Doak, P.; Baheti, K.; Tilley, T. D.; Segalman, R. A.; Majumdar, A. *Nano Lett.* **2009**, *9*, 1164–1169.

(162) Venkataraman, L.; Klare, J. E.; Tam, I. W.; Nuckolls, C.; Hybertsen, M. S.; Steigerwald, M. L. *Nano Lett.* **2006**, *6*, 458–462.

(163) French, W. R.; Iacovella, C. R.; Rungger, I.; Souza, A. M.; Sanvito, S.; Cummings, P. T. *J. Phys. Chem. Lett.* **2013**, *4*, 887–891.

(164) Toher, C.; Sanvito, S. *Phys. Rev. B* **2008**, *77*, 155402.

(165) Pontes, R. B.; Rocha, A. R.; Sanvito, S.; Fazzio, A.; Roque da Silva, A. J. *ACS Nano* **2011**, *5*, 795–804.

(166) Quek, S. Y.; Choi, H. J.; Louie, S. G.; Neaton, J. B. *Nano Lett.* **2009**, *9*, 3949–3953.

(167) Widawsky, J.; Chen, W.; Vázquez, H.; Kim, T.; Breslow, R.; Hybertsen, M. S.; Venkataraman, L. *Nano Lett.* **2013**, *13*, 2889–2894.

(168) Li, C.; Pobelov, I.; Wandlowski, T. *J. Am. Chem. Soc.* **2008**, *130*, 318–326.

(169) Adams, N. W. H.; Kramer, J. R. *Environ. Toxicol. Chem.* **1998**, *17*, 625–629.

(170) Li, J.; Shi, L.; Chen, Y.; Zhang, Y.; Guo, Z.; Su, B.; Liu, W. *J. Mater. Chem.* **2012**, *22*, 9774–9781.

(171) Baheti, K.; Malen, J. A.; Doak, P.; Reddy, P.; Jang, S.-Y.; Tilley, T. D.; Majumdar, A.; Segalman, R. A. *Nano Lett.* **2008**, *8*, 715–719.

(172) Bürkle, M.; Viljas, J. K.; Vonlanthen, D.; Mishchenko, a.; Schön, G.; Mayor, M.; Wandlowski, T.; Pauly, F. *Phys. Rev. B* **2012**, *85*, 075417.

(173) Kiguchi, M.; Miura, S.; Takahashi, T.; Hara, K.; Sawamura, M.; Murakoshi, K. *J. Phys. Chem. C* **2008**, *112*, 13349–13352.

(174) Kim, B.; Choi, S. H.; Zhu, X.-Y.; Frisbie, C. D. *J. Am. Chem. Soc.* **2011**, *133*, 19864–19877.

(175) Reed, M. a. *Science.*. **1997**, *278*, 252–254.

(176) Boya, R.; Jayaraj, D.; Kulkarni, G. U. *Chem. Sci.* **2013**, *4*, 2530.

(177) Béthencourt, M. I.; Srisombat, L.; Chinwangso, P.; Lee, T. R. *Langmuir* **2009**, *25*, 1265–1271.

(178) Boer, B. De; Meng, H.; Perepichka, D.; Zheng, J.; Frank, M. M.; Chabal, Y. J.; Bao, Z. *Langmuir* **2003**, 4272–4284.

(179) Morita, T.; Lindsay, S. *J. Am. Chem. Soc.* **2007**, *129*, 7262–7263.

(180) Fukagawa, H.; Yamane, H.; Kera, S.; Okudaira, K. K.; Ueno, N. *Phys. Rev. B - Condens. Matter Mater. Phys.* **2006**, *73*.

(181) Greczynski, G.; Kugler, T.; Salaneck, W. R. *Thin Solid Films* **1999**, *354*, 129–135.

(182) Li, R.; Cai, C.; Hu, L.; Wu, H.; Zhang, W.; Zhu, J. *Appl. Surf. Sci.* **2013**, *276*, 258–261.

(183) MacHida, S. I.; Nakayama, Y.; Duhm, S.; Xin, Q.; Funakoshi, A.; Ogawa, N.; Kera, S.; Ueno, N.; Ishii, H. *Phys. Rev. Lett.* **2010**, *104*.

(184) Narioka, S.; Ishii, H.; Yoshimura, D.; Sei, M.; Ouchi, Y.; Seki, K.; Hasegawa, S.; Miyazaki, T.; Harima, Y.; Yamashita, K. *Appl. Phys. Lett.* **1995**, *67*, 1899.

(185) Park, Y.; Choong, V.; Gao, Y.; Hsieh, B. R.; Tang, C. W. *Appl. Phys. Lett.* **1996**, *68*, 2699–2701.

(186) Salaneck, W. R. *J. Electron Spectros. Relat. Phenomena* **2009**, *174*, 3–9.

(187) Salaneck, W. .; Lögdlund, M.; Fahlman, M.; Greczynski, G.; Kugler, T. The electronic structure of polymer–metal interfaces studied by ultraviolet photoelectron spectroscopy. *Materials Science and Engineering: R: Reports*, 2001, *34*, 121–146.

(188) Sueyoshi, T.; Fukagawa, H.; Ono, M.; Kera, S.; Ueno, N. *Appl. Phys. Lett.* **2009**, *95*.

(189) Takahashi, T.; Tokailin, H.; Sagawa, T. *Phys. Rev. B* **1985**, *32*, 8317–8324.

(190) Hüfner, S.; Schmidt, S.; Reinert, F. *Nucl. Instruments Methods Phys. Res. Sect. A Accel. Spectrometers, Detect. Assoc. Equip.* **2005**, *547*, 8–23.

(191) Kong, L.; Bjelkevig, C.; Gaddam, S.; Zhou, M.; Lee, Y. H.; Han, G. H.; Jeong, H. K.; Wu, N.; Zhang, Z.; Xiao, J.; Dowben, P. A.; Kelber, J. A. *J. Phys. Chem. C* **2010**, *114*, 21618–21624.

(192) Professor Dr. Stefan Hüfner. In *Photoelectron Spectroscopy*; 1996; pp. 403–419.

(193) Schwan, H. P. *Biophysik* **1966**, *3*, 181–201.

(194) Mirtaheri, P.; Grimnes, S.; Martinsen, Ø. G. *IEEE Trans. Biomed. Eng.* **2005**, *52*, 2093–2099.

(195) Van der Linde, A. J.; Bijsterbosch, B. H. Electrode polarization and its implications in streaming potential and streaming current measurements. *Colloids and Surfaces*, 1989, *41*, 345–352.

(196) Emmert, S.; Wolf, M.; Gulich, R.; Krohns, S.; Kastner, S.; Lunkenheimer, P.; Loidl, A. Electrode polarization effects in broadband dielectric spectroscopy. *The European Physical Journal B*, 2011, *83*, 157–165.

(197) Sharenko, A.; Kuik, M.; Toney, M. F.; Nguyen, T.-Q. *Adv. Funct. Mater.* **2014**, n/a – n/a.

(198) Mitsumori, T.; Inoue, K. *J. Am. Chem. Soc.* **1995**, 2467–2478.

(199) Ikeda, T.; Higuchi, M.; Sato, A.; Kurth, D. *Org. Lett.* **2008**, 2004–2007.

(200) Zamborini, F. P.; Leopold, M. C.; Hicks, J. F.; Kulesza, P. J.; Malik, M. A.; Murray, R. W. *J. Am. Chem. Soc.* **2002**, *124*, 8958–8964.

(201) Toberer, E. S.; Baranowski, L. L.; Dames, C. *Annu. Rev. Mater. Res.* **2012**, *42*, 179–209.

(202) Losego, M. D.; Cahill, D. G. *Nat. Mater.* **2013**, *12*, 382–384.

(203) Ong, W.-L.; Rupich, S. M.; Talapin, D. V; McGaughey, A. J. H.; Malen, J. A. *Nat. Mater.* **2013**, *12*, 410–415.

(204) Yuan, M.; Zhitomirsky, D.; Adinolfi, V.; Voznyy, O.; Kemp, K. W.; Ning, Z.; Lan, X.; Xu, J.; Kim, J. Y.; Dong, H.; Sargent, E. H. *Adv. Mater.* **2013**, *25*, 5586–5592.

(205) Joseph, Y.; Besnard, I.; Rosenberger, M.; Guse, B.; Heinz-Georg, N.; Wessels, J. M.; Wild, U.; Knop-Gericke, A.; Su, D.; Schlogl, R.; Yasuda, A.; Vossmeyer, T. *J. Phys. Chem. B* **2003**, *107*, 7406–7413.

(206) Joanis, P.; Tie, M.; Dhirani, A.-A. *Langmuir* **2013**, *29*, 1264–1272.

(207) Müller, K.; Wei, G.; Raguse, B.; Myers, J. *Phys. Rev. B* **2003**, *68*, 155407.

(208) Peng, Z. L.; Sun, Y. Y.; Zhou, X. Y.; Wang, Y. H.; Han, D.; Niu, Z. J.; Zhou, X. S. *Int. J. Electrochem. Sci.* **2013**, *8*, 6544–6552.

(209) Luo, L.; Choi, S. H.; Frisbie, C. D. *Chem. Mater.* **2011**, *23*, 631–645.

(210) Lang, N. D.; Kagan, C. R. *Nano Lett.* **2006**, *6*, 2955–2958.

(211) Wang, G. R.; Wang, L.; Rendeng, Q.; Wang, J.; Luo, J.; Zhong, C.-J. *J. Mater. Chem.* **2007**, *17*, 457.

(212) Wold, D. J.; Haag, R.; Rampi, M. A.; Frisbie, C. D. *J. Phys. Chem. B* **2002**, *106*, 10–13.

(213) Anderson, P. *Phys. Rev. Lett.* **1975**, 953–955.

(214) Zhou, Y. X.; Jiang, F.; Chen, H.; Note, R.; Mizuseki, H.; Kawazoe, Y. *J. Chem. Phys.* **2008**, *128*, 044704.

(215) Müller, K.-H. *J. Chem. Phys.* **2008**, *129*, 044708.

(216) Stallinga, P. Electronic transport in organic materials: Comparison of band theory with percolation/(variable range) hopping theory. *Advanced Materials*, 2011, *23*, 3356–3362.

(217) Coquil, T.; Reitz, C.; Brezesinski, T.; Nemanick, E. J.; Tolbert, S. H.; Pilon, L. *J. Phys. Chem. C* **2010**, *114*, 12451–12458.

(218) Leitner, D.; Wolynes, P. Heat flow through an insulating nanocrystal. *Physical Review E*, 2000, *61*, 2902–2908.

(219) Toberer, E. S.; Baranowski, L. L.; Dames, C. Advances in Thermal Conductivity. *Annual Review of Materials Research*, 2012, *42*, 179–209.

(220) Li, D.; Wu, Y.; Kim, P.; Shi, L.; Yang, P.; Majumdar, A. *Appl. Phys. Lett.* **2003**, *83*, 2934–2936.

(221) Cahill, D. G.; Pohl, R. O. *Phys. Rev. B* **1987**, *35*, 4067–4073.

(222) Bullen, A. J.; O'Hara, K. E.; Cahill, D. G.; Monteiro, O.; Von Keudell, A. *J. Appl. Phys.* **2000**, *88*, 4.

(223) Zink, B. L.; Pietri, R.; Hellman, F. *Phys. Rev. Lett.* **2006**, *96*.

(224) Moon, S.; Hatano, M.; Lee, M.; Grigoropoulos, C. P. *Int. J. Heat Mass Transf.* **2002**, *45*, 2439–2447.

(225) Van den Brule, B. H. A. A. *Rheol. Acta* **1989**, *28*, 257–266.

(226) Finefrock, S. W.; Wang, Y.; Ferguson, J. B.; Ward, J. V.; Fang, H.; Pfluger, J. E.; Dudis, D. S.; Ruan, X.; Wu, Y. *Nano Lett.* **2013**, *13*, 5006–5012.

(227) Lee, W.; Kim, K.; Jeong, W.; Zotti, L. A.; Pauly, F.; Cuevas, J. C.; Reddy, P. *Nature* **2013**, *498*, 209–212.

(228) Lienhard, J. H. *J. Heat Transfer* **2010**, *82*, 198.

(229) Matey, J. R.; Blanc, J. *J. Appl. Phys.* **1985**, *57*, 1437–1444.

(230) Lee, D. T.; Pelz, J. P.; Bhushan, B. *Rev. Sci. Instrum.* **2002**, *73*, 3525.

(231) Jeandupeux, O.; Marsico, V.; Acovic, A.; Fazan, P.; Brune, H.; Kern, K. *Microelectron. Reliab.* **2002**, *42*, 225–231.

(232) Hansen, P. J.; Strausser, Y. E.; Erickson, A. N.; Tarsa, E. J.; Kozodoy, P.; Brazel, E. G.; Ibbetson, J. P.; Mishra, U.; Narayanamurti, V.; DenBaars, S. P.; Speck, J. S. *Appl. Phys. Lett.* **1998**, *72*, 2247–2249.

(233) Jaensch, S.; Schmidt, H.; Grundmann, M. In *Physica B: Condensed Matter*; 2006; Vol. 376-377, pp. 913–915.

(234) Platzek, D.; Karpinski, G.; Stiewe, C.; Ziolkowski, P.; Drasar, C.; Muller, E. Potential-Seebeck-microprobe (PSM): measuring the spatial resolution of the Seebeck coefficient and the electric potential. *Thermoelectrics, 2005. ICT 2005. 24th International Conference on*, 2005, 13–16.

(235) Chen, N.; Gascoin, F.; Snyder, G. J.; Müller, E.; Karpinski, G.; Stiewe, C. *Appl. Phys. Lett.* **2005**, *87*, -.

(236) Iwanaga, S.; Snyder, G. J. *J. Electron. Mater.* **2012**, *41*, 1667–1674.

(237) Miessler, G.; Donald, T. *Inorganic Chemistry*; 4th ed.; Prentice Hall.

(238) Shriver, D.F. Atkins, P. W. *Inorganic Chemistry*; 3rd ed.; Oxford University Press: Oxford, 2001.

(239) Zumdahl, S. S. *Chemical principles*; Houghton Mifflin Company: Boston, 2005.

(240) Hynes, M. J.; O'Dowd, M. *J. Chem. Soc. Dalt. Trans.* **1987**, 563–566.

(241) Huheey, J. E.; Keiter, E. A.; Keiter, R. L. *Inorganic Chemistry: Principles of Structure and Reactivity*; 4th ed.; HarperCollins College Publishers, 1993.

(242) Shen, C.; Hui, C.; Yang, T.; Xiao, C.; Tian, J.; Bao, L.; Chen, S.; Ding, H.; Gao, H. *Chem. Mater.* **2008**, *20*, 6939–6944.

(243) Caragheorgheopol, A.; Chechik, V. *Phys. Chem. Chem. Phys.* **2008**, *10*, 5029–5041.

(244) Cahill, D. G. *Rev. Sci. Instrum.* **1990**, *61*, 802–808.

(245) Riffat, S.; Ma, X. *Appl. Therm. Eng.* **2003**, *23*, 913–935.

(246) Abraham, T. J.; MacFarlane, D. R.; Pringle, J. M. *Chem. Commun.* **2011**, *47*, 6260–6262.

(247) Chikina, I.; Shikin, V.; Varlamov, A. A. *Phys. Rev. E* **2012**, *86*, 011505.

(248) MacFarlane, D. R.; Tachikawa, N.; Forsyth, M.; Pringle, J. M.; Howlett, P. C.; Elliott, G. D.; Davis, J. H.; Watanabe, M.; Simon, P.; Angell, C. A. *Energy Environ. Sci.* **2014**, *7*, 232.

(249) Abraham, T. J.; MacFarlane, D. R.; Pringle, J. M. *Energy Environ. Sci.* **2013**, *6*, 2639.

(250) Quickenden, T.; Vernon, C. *Sol. Energy* **1986**, *36*, 63–72.

(251) Hu, R.; Cola, B. A.; Haram, N.; Barisci, J. N.; Lee, S.; Stoughton, S.; Wallace, G.; Too, C.; Thomas, M.; Gestos, A.; Cruz, M. E. Dela; Ferraris, J. P.; Zakhidov, A. A.; Baughman, R. H. *Nano Lett.* **2010**, *10*, 838–846.

(252) Heitner-Wirguin, C. *J. Memb. Sci.* **1996**, *120*, 1–33.

(253) Sugioka, H. *Langmuir* **2014**, *30*, 8624–8630.

(254) Würger, A. *Phys. Rev. Lett.* **2008**, *101*, 108302.

(255) Reichl, M.; Herzog, M.; Götz, A.; Braun, D. *Phys. Rev. Lett.* **2014**, *112*, 198101.

(256) Monroe, C.; Newman, J. *J. Electrochem. Soc.* **2003**, *150*, A1377.

(257) Sone, Y.; Ekdunge, P.; Simonsson, D. *J. Electrochem. Soc.* **1996**, *143*, 1254–1259.

(258) Chou, J.; McFarland, E. W.; Metiu, H. *J. Phys. Chem. B* **2005**, *109*, 3252–3256.

(259) Cahill, D. G. *Rev. Sci. Instrum.* **2004**, *75*, 5119–5122.

(260) Burheim, O.; Vie, P. J. S.; Pharoah, J. G.; Kjelstrup, S. *J. Power Sources* **2010**, *195*, 249–256.

(261) Zhang, Q.; Sun, Y.; Xu, W.; Zhu, D. *Adv. Mater.* **2014**.

(262) Merle, G.; Wessling, M.; Nijmeijer, K. *J. Memb. Sci.* **2011**, *377*, 1–35.

(263) Zhang, Y.; Bahk, J.-H.; Lee, J.; Birkel, C. S.; Snedaker, M. L.; Liu, D.; Zeng, H.; Moskovits, M.; Shakouri, A.; Stucky, G. D. *Adv. Mater.* **2014**, *26*, 2755–2761, 2618.

(264) Okamoto, H.; Toyama, T.; Hattori, K. *J. Non. Cryst. Solids* **2004**, *338-340*, 341–344.

(265) Mehraeen, S.; Coropceanu, V.; Brédas, J.-L. *Phys. Rev. B* **2013**, *87*, 195209.

(266) Rieke, P. C.; Vanderborgh, N. E. *J. Memb. Sci.* **1987**, *32*, 313–328.

(267) Stavrinidou, E.; Leleux, P.; Rajaona, H.; Khodagholy, D.; Rivnay, J.; Lindau, M.; Sanaur, S.; Malliaras, G. G. *Adv. Mater.* **2013**, *25*, 4488–4493.

(268) Wang, H.; Ail, U.; Gabrielsson, R.; Berggren, M.; Crispin, X. *Adv. Energy Mater.* **2015**.

(269) Shetzline, J. A.; Creager, S. E. *J. Electrochem. Soc.* **2014**, *161*, H917–H923.

(270) Kosuga, A.; Kurosaki, K.; Muta, H.; Stiewe, C.; Karpinski, G.; Müller, E.; Yamanaka, S. *Mater. Trans.* **2006**, *47*, 1440–1444.

(271) Bertini, L.; Stiewe, C.; Toprak, M.; Williams, S.; Platzek, D.; Mrotzek, A.; Zhang, Y.; Gatti, C.; Müller, E.; Muhammed, M.; Rowe, M. *J. Appl. Phys.* **2003**, *93*.

(272) Nakamoto, G.; Nakabayashi, Y. *Intermetallics* **2013**, *32*, 233–238.

(273) D., P.; G., K.; C., D.; Muller, C.; Muller, E. *Mater. Sci. Forum* **2005**, *492-493*, 587–592.

(274) Kamarudin, M. A.; Sahamir, S. R.; Datta, R. S.; Long, B. D.; Mohd Sabri, M. F.; Mohd Said, S. A review on the fabrication of polymer-based thermoelectric materials and fabrication methods. *The Scientific World Journal*, 2013, *2013*.

(275) Lang, U.; Müller, E.; Naujoks, N.; Dual, J. *Adv. Funct. Mater.* **2009**, *19*, 1215–1220.

(276) Crispin, X.; Jakobsson, F. L. E.; Crispin, A.; Grim, P. C. M.; Andersson, P.; Volodin, A.; van Haesendonck, C.; Van der Auweraer, M.; Salaneck, W. R.; Berggren, M. *Chem. Mater.* **2006**, *18*, 4354–4360.

(277) Snaith, H. J.; Kenrick, H.; Chiesa, M.; Friend, R. H. *Polymer (Guildf).* **2005**, *46*, 2573–2578.

(278) Kang, S. K.; Buchwalter, S.; Tsang, C. *J. Electron. Mater.* **2000**, *29*, 1278–1283.

(279) Gall, T. P.; Ingraham, A. P. Low temperature ternary C4 flip chip bonding method, 1995.